Physics of Fluids

Mass-balance and locality versus accuracy with the new boundary and interface-conjugate approaches in advection-diffusion lattice Boltzmann method

Cite as: Phys. Fluids **33**, 057104 (2021); https://doi.org/10.1063/5.0047210
Submitted: 11 February 2021 . Accepted: 29 March 2021 . Published Online: 06 May 2021

Irina Ginzburg, and Gonçalo Silva

Physics of Fluids ARTICLE scitation.org/journal/phf

Mass-balance and locality versus accuracy with the new boundary and interface-conjugate approaches in advection-diffusion lattice Boltzmann method

Cite as: Phys. Fluids **33**, 057104 (2021); doi: 10.1063/5.0047210
Submitted: 11 February 2021 · Accepted: 29 March 2021 · Published Online: 6 May 2021

View Online Export Citation CrossMark

Irina Ginzburg[1,a] and Gonçalo Silva[2,b]

AFFILIATIONS

[1]Université Paris-Saclay, INRAE, UR HYCAR, 92160 Antony, France
[2]IDMEC, Department of Mechatronics, University of Évora, Largo dos Colegiais 2, 7000-645 Évora, Portugal

Note: This paper is part of the Special Issue on the Lattice Boltzmann Method.
[a]**Author to whom correspondence should be addressed:** irina.ginzburg@inrae.fr
[b]**Electronic mail:** goncalo.nuno.silva@gmail.com

ABSTRACT

We introduce two new approaches, called A-LSOB and N-MR, for boundary and interface-conjugate conditions on flat or curved surface shapes in the advection-diffusion lattice Boltzmann method (LBM). The Local Second-Order, single-node A-LSOB enhances the existing Dirichlet and Neumann normal boundary treatments with respect to locality, accuracy, and Péclet parametrization. The normal-multi-reflection (N-MR) improves the directional flux schemes via a local release of their nonphysical tangential constraints. The A-LSOB and N-MR restore all first- and second-order derivatives from the nodal non-equilibrium solution, and they are conditioned to be exact on a piece-wise parabolic profile in a uniform arbitrary-oriented tangential velocity field. Additionally, the most compact and accurate single-node parabolic schemes for diffusion and flow in grid-inclined pipes are introduced. In simulations, the global mass-conservation solvability condition of the steady-state, two-relaxation-time (S-TRT) formulation is adjusted with either (i) a uniform mass-source or (ii) a corrective surface-flux. We conclude that (i) the surface-flux counterbalance is more accurate than the bulk one, (ii) the A-LSOB Dirichlet schemes are more accurate than the directional ones in the high Péclet regime, (iii) the directional Neumann advective-diffusive flux scheme shows the best conservation properties and then the best performance both in the tangential no-slip and interface-perpendicular flow, and (iv) the directional non-equilibrium diffusive flux extrapolation is the least conserving and accurate. The error Péclet dependency, Neumann invariance over an additive constant, and truncation isotropy guide this analysis. Our methodology extends from the d2q9 isotropic S-TRT to 3D anisotropic matrix collisions, Robin boundary condition, and the transient LBM.

I. MOTIVATION

Recent physical,[3,41,70,74,78,81,109] biomechanical[67,75,98,100] and engineering[13,72,82] research, and especially solute and heat transfer modeling in porous networks,[18,19,59,71,102,107,108] intensively apply the lattice Boltzmann method (LBM)[58] in complex problems for solving linear,[11,31,45,50,60,83,99] non-linear,[7,8,27,43,110] isotropic or anisotropic[15,25,32,66,84,101,107] advection-diffusion equation (ADE) with homogeneous or heterogeneous coefficients and sources.[29,38,65,76] Although the coordinate d2q5/d3q7 discrete velocity stencil is sufficient to match the diagonal diffusion tensors, the specific combinations of the coordinate and diagonal equilibrium weights are appealing for their truncation isotropy and advanced stability.[31,34,60] In bulk, the standard LBM guarantees the local and global mass conservation, which is defined from the zero-moment (sum) of its real variables, called populations, allowing for a regular, cuboid control-volume interpretation of the LBM mass-balance.[28] The simplest heterogeneity treatment–do nothing algorithm, and the Maxwell, bounce-back (BB), and mirror (specular-forward) population reflections on the impermeable boundary preserve the global conservation property at the cost of only approximately mid-node, implicit location of the grid-aligned walls and interfaces.[16,29,52,54,97]

However, it was recognized[14,107] that although the mirror reflection is suitable, the BB and "local" specular reflection (which returns the mass to departure node), enforce to zero not only the normal but also the tangential mass-flux components through the wall-inclined discrete-velocities.[26,33] The implicit interface tracking shares a similar tangential deficiency, because its advective-diffusive flux and scalar-field continuity conditions intrinsically couple[29] the BB and the (anti-BB) ABB Dirichlet rule.[26,56] The distribution moments can be regarded as the best indicators of the nonphysical solution behavior. So that, when the solute travels along an impermeable straight tubular conduit, the BB spurious effects on the first and second Gaussian moments, leading to (i) a retardation of the mean advection velocity $\mathscr{U}$ and (ii) a decrease in the molecular diffusion coefficient $\mathscr{D}_0$, grow with a free-tunable diagonal weight-value and decay only linearly with the space resolution,.[33,36] Gebäck and Heintz[17] extended the mirror reflection for curved wall on the d3q7 and d3q19 lattices, and improved the BB in the presence of the tangential wall flux in the diffusion problems. However, on the one side, the global accuracy worsens when the populations reflected by the same ghost solid node conserve its incoming mass; on the other side, the BB behaves as accurately as the mass-conserving mirror schemes, and much better than the non-conserving ones, for the zero tangential boundary flux.

Our boundary value problems are delivered by the extended method of moments (EMM),[37,94] which is the mathematical algorithm for the recursive prediction of the distribution moments: dispersion, skewness, kurtosis,… The EMM extends the Brenner's generalized dispersion approach[4] and the volume averaging boundary-value formulation,[93] from the second-order microscopic spatial Taylor moment to any-order, spatial or temporal, moment. The EMM applies in any nature multi-scale streamwise-periodic stationary d-dimensional, Newtonian or non-Newtonian, velocity field resolved in the piecewise continuous heterogeneous porosity field, where it simultaneously builds two systems of moments: the spatial (mean-concentration, due to Taylor & Aris[1,92]) and the temporal (residence time distribution, due to Danckwerts[12]) The high-order moments characterize the non-Gaussian behavior, the EMM is hence appealing to classify them, particularly in porous and composite materials. Other utility is that the method builds recursively the steady-state ADE with the non-uniform, global-mass conserving sources; the ADE is closed by an impermeable Neumann boundary or periodic interface, and its symbolic solutions are available[37,94] for benchmarking purpose.[38]

The flow and the associated heat transport are often modeled with the so-called (multiple-relaxation-time thermal) MRT-TLBM, e.g., in a very recent work[78] using the BB and ABB straight-wall rules. However, the MRT-TLBM operates the d2q9 flow collision with only two distinctive relaxation rates: the symmetric one for the fluid viscosity and the anti-symmetric one for the second-order BB accuracy using the exact Poiseuille flow solution,[20,22] whereas the energy conservation equation is modeled with the d2q5 isotropic MRT-ADE. Indeed, these two collision models automatically reduce to the two-relaxation-time TRT collision,[25,29] which is simpler, lattice independent, and more computationally efficient; additionally, the TRT allows for the solution parametrization, stability, and boundary/interface control with the help of the specific combination Λ of its two relaxation rates; moreover, the optimal TRT-ADE stability choice[31] $\Lambda = \frac{1}{4}$ remains robust in high Reynolds fluid flow modeling.[79] The methodology developed in the present work is especially compact with the TRT collision but it extends for any linear collision operator. Numerically, we solve steady-state linear ADE with the recent (stationary) S-TRT formulation[40] where (i) an arbitrary physical and model parameter range is available, because the S-TRT is quite insensitive to the transient stability restrictions and Péclet range, and (ii) the modeled solution is fixed by the grid Péclet number $\mathscr{U}/\mathscr{D}_0$ and Λ for any diffusion collision rate.

We apply the d2q9 with the free-tunable advection-diffusion equilibrium weights but, since the weight-stencil remains invisible for *a stationary* scalar field in the straight channels,[38] in contrast with the aforementioned transient transport, we focus on the grid-rotated homogeneous and heterogeneous slabs, where all discrete directional effects "come to the surface." To give one impressive example, the effective diffusivity of two diagonal heterogeneous blocks in series differs from its classical harmonic-mean value with the full d2q9 stencil. This happens because its intrinsic *equilibrium* accommodation on the implicit interface, called the A-layer,[39] spoils the canonical piece-wise linear Chapman–Enskog prediction. The A-layer is much more harmful than its *non-equilibrium* B-layer counterpart, responsible for the BB moments corrections,[33,36] because on top of the spurious weight-dependency, the A-layer is capable to modify the physical Péclet scale of the modeled solution, which is mandatory with the EMM for a proper prediction of the Péclet Ansatz in dispersion coefficient and higher order moments. Therefore, we aim to verify the performance of the advanced boundary and interface rules to reduce strong accommodation weight- and grid-inclined effects.

The "linear-interpolation" LI and "multi-reflection" MR ADE approach[26] originates from its fluid flow counterparts[22] and prescribes the Dirichlet scalar condition with the linear combination of three (LI) or five (MR) populations moving along the same wall-cut link, featuring, respectively, the exact linear or parabolic diffusion solutions in arbitrary oriented channels. Li and coworkers[62] built several d2q5/d3q7 Dirichlet LI schemes and introduced flux LI scheme, hereafter referred to as FLI, which comes down to BB on a mid-grid wall. The Cartesian decomposition method[62] involves the population interpolations and estimates the lacking tangential boundary flux value from the actual solution, with the help of the two intersecting coordinate linear MR Dirichlet conditions. This method however sacrifices the assets of the LI/MR link-wise implementation and its transparency for the discrete velocity set, because the d2q9 and d3q19 reduce the coordinate-set convergence by one-order.[64] Then only the d2q5/d3q7 schemes[62] were coupled for the scalar field and *diffusive-flux* interface-conjugate continuity[63] and jumps;[42] these schemes were successfully evaluated against the semi-implicit interface methods.[13,55] The coordinate, linear Dirichlet, Neumann, and Robin directional boundary schemes[48,49] were combined for the interface diffusion conditions[46] and further extended[47] to account for the normal-vector variation along the shaped boundary.

Indeed, the transform of the Neumann and interface-flux conditions to their Dirichlet counterparts (like BB to ABB) has inspired many techniques on straight,[2] stair-wise[9,69] or curved[89] surfaces. In an early work, the Neumann condition is simply plugged[68] into the *three-point* back-sided normal Dirichlet extrapolation, whereas the interface-normal and bilinear extrapolations for curved shapes require even larger stencils.[9,61] A very recent d2q5 scheme[89] is more compact: it operates the ghost solid-bisection node with the two-node linear (but again not directional) population interpolations and expresses the lacking boundary-flux from the obtained non-equilibrium solution, involving the ABB only for ghost population solution. However, the advection regime validation is commonly limited to a relatively small Péclet number (about twenty), whereas the ABB completely degrades its second-order accuracy for a mid-grid surface location in an interface-perpendicular plug flow at Pe $\approx 10^2$,[38] because its directional closure relation interferences with the advective projections,[26] overlooked by the later asymptotic analysis.[106]

With these ideas in mind, the ABB, the equivalent LI schemes[62,106] and the MR Dirichlet schemes[26] have been recently extended[40] to "linear" [ABB/MPLI/PLI] and "parabolic" accurate [KMR/PP] Dirichlet families, improving their accuracy and parametrization by the grid Péclet number in the presence of the velocity field [PAB/PLI/KMR/PP] and space-variable mass-source, such that every family contains an infinite number of members (coefficients) of equivalent spatial accuracy; only the parametrized LMKC scheme[62] enters the MPLI family. The LI can be operated in-node, whereas the MR requires the next directional fluid neighbor; both LI and MR cope with any discrete-velocity set but require, as a minimum, the TRT collision for their parametrization. Along these lines, this work complements the list[40] with the particular single-node three-population *parabolic* PPLI scheme which is exact on a pure-diffusion parabolic profile in an arbitrary inclined channel. For the sake of completeness, we also provide its flow-counterpart *(inclined Poiseuille)* IPLI scheme, which models exactly an arbitrary-inclined Poiseuille Stokes force-driven flow, at least. These schemes extend the recent LI schemes[95,96] from the straight to the grid-rotated geometry and, most likely, they are the most simple and compact boundary/interface schemes offering the parabolic accuracy level on diffusion-type problems; the two-node MR ADE and flow schemes[40] retain this formal accuracy on any fluid flow field.

Concerning the Neumann schemes, it has been shown[40] that the FLI destinates for the advective-diffusive flux, rather than for the diffusive flux, but it accounts only for the diffusive-flux spatial variation and then it loses its (diffusion) parabolic accuracy in a uniform grid-inclined flow. The FLI is then extended[40] to a two-node parabolic-accurate advective-diffusive flux FMR scheme and diffusive-flux DFLI family; in reality, even when the diffusive-flux and the advective-diffusive flux closure conditions are equivalent in theory, e.g., for a no-slip velocity or interface-continuous scalar field, they are not identical on the numerical solutions. All novel Dirichlet and Neumann schemes[40] were coupled for the directional interface-conjugate and Robin condition, and validated through the EMM problems, but their Neumann conditions remained limited to zero rotated tangential advective-diffusive flux problems. Also, a recent study[39] has shown that the scalar-field and its local gradient estimate are not necessarily independent of an additive constant in the modeled Neumann and periodic-interface problems. Finally, also the discussion on mass leakage remains a "tabu" topic. Although this is a principal issue, as of today it has been poorly investigated.

Our objective is hence twofold. On the one side, we intend to develop compact normal-flux Neumann schemes. Conversely, we want to quantify their mass-balance with respect to its exact, body-fitted, definition. To this end, we introduce and examine two new approaches: N-MR and A-LSOB. The two methods resort to the same, *in-node non-equilibrium solution* for all first and second-order derivatives, borrowing the idea of the Local Second-Order Boundary (LSOB) reconstruction[21] in its "Lnode" formulation.[87] On this basis, the (normal) N-MR expands the anti-tangential N-BB correction[26,28] to any LI/MR flux rule. The N-MR re-builds it precisely with the internal coefficients of the MR closure relation and then subtracts this correction from the incoming population. In this way, whereas the reconstruction discards the directional implementation, the N-MR does not perform any additional interpolation and preserves the versatility for interface-conjugate: specifically, N-FLI remains local; the MR flux schemes also incorporate an independent correction for space-variable mass-source.

In turn, the A-LSOB is both single-node and parabolic-accurate: in transient algorithm, it prescribes the third-order accurate Chapman–Enskog solution for the incoming populations explicitly, such that its derivatives are constrained to the Taylor normal expansion of a given boundary rule, either Dirichlet or Neumann; the Robin condition can be straightforwardly obtained from their combination. In turn, the S-TRT operates with the equilibrium and non-equilibrium components, rather than with populations, and it embeds all constraints into its global linear system. It should be emphasized that the A-LSOB has been developed independently of the single-node approach,[104,105] recently extended for the Dirichlet, Neumann and Robin conditions from its flow counterpart[103] with the d2q5 BGK[104] and d2q9 anisotropic matrix collision.[105] These two, flow and transport, methods adopt the original "Lwall" formulation[21] and express the Chapman–Enskog solution through the surface variables but, "for the sake of simplicity", they drop all second-order derivatives. The methodology[104,105] is elaborated for the straight in-node wall and, in the curvilinear coordinates, for a circular surface. The method is reported to support the second-order accuracy through the benchmark simulations (i) in straight wall-node coincident surface, whereby the spatial variation vanishes from the closure relations, and (ii) in heat conduction inside a circle, where the diffusive flux only varies along the surface. Hence, the A-LSOB is expected to enhance those methods, principally, by now considering the spatial flux variation through the parabolic terms in the Chapman–Enskog solution. Several numerical examples will delineate the difference between the parabolic and linear-accurate A-LSOB.

Another point of focus is put on the comparison of the LI, MR, N-MR, and A-LSOB for their mass-balance properties. In fact, the solvability condition of the EMM boundary problems requires the mass-source distribution $\mathscr{M}(\vec{r})$ to conserve the global mass, say $\langle \mathscr{M}(\vec{r}) \rangle \equiv 0$. We prescribe it exactly and adjust the S-TRT with two heuristic solvability techniques: (i) a grid-uniform mass-source M_0 following,[40] then $\langle \mathscr{M}(\vec{r}) + M_0 \rangle \equiv 0$ in any geometry, or (ii) a non-conserving corrective flux $\pm\Phi_0$, prescribed on two parallel delimiting surfaces. The two variables, M_0 or Φ_0, join the list of the global S-TRT unknowns and their solution measures the mass-balance property of the given scheme. Roughly speaking, these two experiments compare the uniform bulk distribution of the mass-leakage with its surface counterbalance.

We address them with the Taylor dispersion Ansatz[34,92] where the adjacent EMM problem combines the parabolic tangential velocity and mass-source fields. We will show that in the presence of the rotated advection, the quartic polynomial solution becomes only available with the hydrodynamic advection-diffusion weights, and it incorporates an anisotropic truncation correction; the latter obeys the spurious non-linear Péclet scale and vanishes only with a particular choice of two remaining free model parameters. The constructed effective solution is first validated with the specific, fourth-order accurate Dirichlet and Neumann conditions, and then examined for its deviations due to generic schemes in open flow and at the diffusive interface. In parallel, a simultaneous truncation and mass-balance effect will be quantified exactly in straight heterogeneous blocks in series. This is a tough test, where the interface-normal Darcy plug flow induces asymmetry across the implicit interface,[38] and although all MR schemes handle the diffusion problem exactly, they asymptotically decay only with the first-order accuracy, the BB alike, in advection dominant grid-inclined flow,.[40] At last, we will aim to understand whether the N-MR is able to reduce their accommodation.

This paper is organized as follows: Sec. II recalls the ADE-LBM and MR, introduces N-MR, A-LSOB, and the 2D TRT reconstruction. Section III formulates the S-TRT, discusses its solvability, and recasts with it the N-MR, interface-conjugate, and A-LSOB. Section IV validates N-MR and A-LSOB on the heterogeneous rotated parabolic profiles and also addresses their modeling with the lower-order treatment. Section V constructs the effective rotated quartic-polynomial solution and employs it for boundary and interface analysis. Section VI addresses the heterogeneous blocks in series and proposes an inverse 1d mapping from the A-LSOB to MR. In the Appendix, Subsection A summarizes the LI and MR families; Subsection B exemplifies the reconstruction step; Subsection C builds the corrective flux for the exact quartic solutions; and Subsection D examines the mass-balance within the grid-shifted straight interface.

II. THE MR, N-MR, AND A-LSOB

We define the LBM framework in Sec. II A, introduce the MR and A-LSOB closure relation in Sec. II B, reconstruct all first- and second-order 2D derivatives in Sec. II C, and then build tangential-flux N-MR corrections in Sec. II D. Section II E embeds the reconstruction process into N-MR and A-LSOB numerical algorithms. Section II F summarizes the new methods and discusses their extensions. The notations employed for Dirichlet and Neumann schemes are gathered in Tables I and II, respectively; the reconstructions are specified in Table III.

A. The simplified ADE model

Let us assume that a continuous velocity field $\vec{u}(\vec{r})$, heterogeneous porosity $\phi = \{\phi_k\}$, diffusion coefficient $\mathscr{D} = \{\mathscr{D}_k\}$ and mass-source $\mathscr{M} = \{\mathscr{M}_k\}$ are prescribed on the equidistant $d-$ dimensional computational grid $\vec{r} \in V_p$, where the scalar field $P(\vec{r}) = \{P_k(\vec{r})\}$ obeys the linear isotropic ADE,

$$\partial_t \phi_k P_k + \nabla \cdot \vec{u} P_k - \mathscr{M}_k = \nabla \cdot \mathscr{D}_k \nabla P_k \,, \; \mathscr{D}_k = \phi_k \mathscr{D}_0. \tag{1}$$

The local variables of the dDqQ LBM model are $Q_m = Q - 1$ moving populations $\{f_q(\vec{r}, t)\,,\, q = 1, .., Q_m\}$ and $f_0(\vec{r}, t)$, an immobile one. At each time step t, the non-equilibrium population component $n_q = f_q - e_q$ is updated by a linear collision operator and the modified population propagates to the neighbor grid node $\vec{r} + \vec{c}_q$. Let us first put the mass-source $\{\mathscr{M}_k\}$ aside and prescribe the simplest linear equilibrium distribution $e_q(\vec{r}) = e_q^+(\vec{r}) + e_q^-(\vec{r})$ with the local mass variable $P_k(\vec{r}, t) = \sum_{q=0}^{Q_m} f_q(\vec{r}, t)$,

$$e_q^+(\vec{r}, t) := t_q^{(m)} c_e P_k(\vec{r}, t), \tag{2a}$$

$$e_0^+(\vec{r}, t) := P_k(\vec{r}, t) - \sum_{q=1}^{Q_m} e_q^+(\vec{r}, t), \tag{2b}$$

$$e_q^-(\vec{r}, t) := t_q^{(a)} P_k(\vec{r}, t) \vec{u} \cdot \vec{c}_q \,,\; q = 1, \ldots, Q_m. \tag{2c}$$

The diffusion weight $t_q^{(m)} = \{t_c^{(m)}, t_d^{(m)}\}$ and the advection weight $t_q^{(a)} = \{t_c^{(a)}, t_d^{(a)}\}$ obey independently the same isotropic constraint,

$$\sum_{q=1}^{Q-1} t_q^{(.)} c_{q\alpha} c_{q\beta} = \delta_{\alpha\beta} \,,\; \forall\{\alpha, \beta\} \,,\; t_q^{(.)} \in \left[0, \frac{1}{2}\right]. \tag{3}$$

Hence, there exists an infinite number $(t_c^{(.)}, t_d^{(.)})$ (coordinate, diagonal) weight-stencils obeying Eq. (3), including $\left(\frac{1}{2}, 0\right)$ in d2q5/d3q7. Equation (1) then reads with $\mathscr{D}_k(\vec{r}) = c_e \Lambda_k^-(\vec{r}), \Lambda_k^- = (\tau_k^- - \frac{1}{2})$, where $\tau_k^- > \frac{1}{2}$ is the common relaxation rate assigned for the d velocity eigenvectors $\{c_{q\alpha}\}$ in the isotropic matrix collisions, and τ_k^- is assigned for all anti-symmetric modes in TRT operator; the diffusion-scale equilibrium parameter $c_e \in]0, c_e^{max}(t_q^{(m)})]$ is free-tunable inside its stability interval.[31,60] In what follows, the phase index k is dropped unless indicated.

TABLE I. The Dirichlet schemes are classified with respect to their exactness for piece-wise parabolic pure diffusion and constant-velocity rotated parabolic profiles modeled in an arbitrary inclined channel. (a) and (b) MPLI/LMKC and ABB are exact in the grid-aligned symmetric parabolic profiles with (a) $\Lambda = \frac{\delta^2}{2}\ \forall\, \delta$ and (b) $\Lambda = \frac{1}{8}$, $\delta = \frac{1}{2}$; (c) PPLI and KMR1 are exact on an inclined diffusion profile and grid-aligned advection velocity field $\forall \Lambda$; (a)–(c) using $l_b = 0$ in Eq. (A4) and $l_{int} = 1$ in Eq. (37a) [see also Tables III and IV, Eqs. (121) and (122) in Ref. 40].

Scheme	Single-node	Exact parabolic rotated diffusion	Exact parabolic rotated advection-diffusion $\vec{u} = u_\tau \vec{1}_\tau$	References
MPLI/PLI	✓	$-(a)$	–	Equation (6a), Tables X–XIV
LMKC ∈ MPLI	✓	$-(a)$	–	
ABB ∈ MPLI	✓	$-(b)$	–	
PPLI ∈ LI	✓	✓	$-(c)$	Equation (6b), Tables XII– XIV
KMR1 ∈ MR	–	✓	$-(c)$	Equation (6b), Tables XI– XIV
PP ∈ MR	–	✓	✓	Equation (6b), Tables XI– XIV
T-PP ∈ A-LSOB	✓	✓	✓	Equation (12a)

TABLE II. The Neumann schemes are classified with respect to their exactness for pure diffusion ad constant tangential velocity $\vec{u} = u_\tau \vec{1}_\tau$, grid-rotated piece-wise parabolic profiles; (a): when $u_\tau \neq 0$, FLI is exact only on the grid-aligned interface; (b): when $u_\tau \neq 0$, FMR is also exact on the grid-rotated continuous interface solution or for specific jumps, as $\sigma^{(p)} = \sigma^{(u)}$, $\eta^{(p)} = 0$ in Eq. (36) (see Eq. (102) in Ref. 40. The mass-conservation in the grid-shifted straight slab is indicated with respect to its exact solvability condition in the interface-perpendicular flow $\vec{u} = u_n \vec{1}_n$, where N-MR reduces to MR.

Flux scheme	Single-node	Exact parabolic rotation diffusion	Exact parabolic in rotated $\vec{u} = u_\tau \vec{1}_\tau$	Exact mass-balance in surface perpendicular flow $\vec{u} = u_n \vec{1}_n$	References
FLI ∈ MR	✓	✓	$-(a)$	✓, Eq. (70)	Equation (7), Tables XV–XVIII
FMR ∈ MR	–	✓	$-(b)$	✓, Eq. (70)	Equation (7), Tables XV–XVIII
DFLI ∈ MR	–	✓	✓	–, Eq. (73)	Equation (8), Tables XVI–XVIII
N-FLI ∈ N-MR	✓	✓	✓	✓	FLI with Eqs. (21), (10), and (23a)
N-FMR ∈ N-MR	–	✓	✓	✓	FMR with Eqs. (21), (10), and (23a)
N-DFLI ∈ N-MR	–	✓	✓	–	DFLI with Eqs. (21), (10), and (23b)
T-DFLI ∈ A-LSOB	✓	✓	✓	–	Equation (12b)

B. Closure relations

We numerate the one-half of the discrete velocities $\cup_{q=1}^{Q_m} \vec{c}_q$ with the positive numbers $q \in Q_{\frac{1}{2}}$ [$\mathrm{sgn}_q = 1$] and their opposite vectors with the negative numbers $-q \in Q_{-\frac{1}{2}}$ [$\mathrm{sgn}_{-q} = -1$] . When the population $f_q(\vec{r}_\mathrm{b}, t+1)$ leaves the computational domain at the boundary node $\vec{r}_\mathrm{b}$, the opposite (incoming) population $f_{-q}(\vec{r}_\mathrm{b}, t+1)$ is prescribed by the boundary rule (see Fig. 1). The directional boundary rule computes $f_{-q}(\vec{r}_\mathrm{b}, t+1)$ from the known or already updated solution components (populations, their post-collision, equilibrium and non-equilibrium) moving along the same link $(\vec{c}_q, \vec{c}_{-q})$; this *link-wise* component is termed through $\mathrm{MR}_q(\vec{r}_\mathrm{b}, t)$; the boundary value is prescribed by the term $w_q(\vec{r}_q, \tilde{t})$ in wall point $\vec{r}_q = \vec{r}_\mathrm{b} + \delta_q \vec{c}_q \notin V_p$, $\delta_q \in [0, 1]$, at some suitable time instance $\tilde{t}$:

$$f_{-q}(\vec{r}_\mathrm{b}, t+1) = \mathrm{MR}_q(\vec{r}_\mathrm{b}, t) + w_q(\vec{r}_q, \tilde{t}), \; q \in Q_{\frac{1}{2}} \cup Q_{-\frac{1}{2}}. \quad (4)$$

The content of MPLI/PLI is exemplified for the multi-reflection (MR) in Eqs. (A1) and (A2); their particular reduction to "linear-interpolation" LI is given by Eq. (A3); the w_q is provided in Eq. (A4) for the Dirichlet rules and it makes the core subject of our discussion for the Neumann rules.

The associated (intrinsic, implicitly prescribed) closure relation $\mathrm{CL}_q(\vec{r}_b, t)$ is expressed through the directional derivatives $\partial_q \psi = \nabla\psi \cdot \vec{c}_q$ and $\partial_q^2 \psi = \nabla[\partial_q \psi] \cdot \vec{c}_q$ [hereafter, cut link number q is dropped in δ_q and the coefficients $\alpha_q^{(p)} - \gamma_q^{(u)}$, unless indicated]:

$$-w_q(\vec{r}_q, \tilde{t}) = \mathrm{CL}_q(\vec{r}_\mathrm{b}, t),$$

$$\mathrm{CL}_q(\vec{r}_\mathrm{b}, t) := \Big[\alpha^{(p)} e_q^+ + \alpha^{(u)} e_q^- + \beta^{(p)} \partial_q e_q^+ + \beta^{(u)} \partial_q e_q^- + \gamma^{(p)} \partial_q^2 e_q^+ + \gamma^{(u)} \partial_q^2 e_q^- + \tau^{(p)} \partial_t e_q^+ + \tau^{(u)} \partial_t e_q^-\Big](\vec{r}_\mathrm{b}, t). \quad (5)$$

In this work, we focus us on the spatial component and refer to Ref. 40 for the temporal coefficients $\tau^{(p)}$ and $\tau^{(u)}$. The parametrized schemes produce identical steady-state solutions when Péclet number $\mathrm{Pe} = \mathscr{U}\mathscr{L}/\mathscr{D}_0$ and the specific combinations of the symmetric/anti-symmetric relaxation rates are fixed, regardless the particular values assigned to $\mathscr{U}$ and $\mathscr{D}_0$ on given grid $\mathscr{L}$.[30,38] The LI and MR schemes[40] are all parametrized for any geometry. The following Dirichlet families[40] apply here: the one-node "linear" [MPLI/PLI] and the two-node "parabolic" [PP/KMR] fit CL_q to, respectively, the linear and parabolic, directional Taylor expansion from $\vec{r}_\mathrm{b}$ to $\vec{r}_q = \vec{r}_\mathrm{b} + \delta\vec{c}_q$:

$$\mathrm{MPLI/PLI} : \alpha^{(p)} (P + \delta\partial_q P)_{\vec{r}_\mathrm{b}}^{num} \approx \alpha^{(p)} P(\vec{r}_q), \quad (6a)$$

$$\mathrm{PP/KMR/PPLI} : \alpha^{(p)} \left(P + \delta\partial_q P + \frac{1}{2}\delta^2 \partial_q^2 P\right)_{\vec{r}_\mathrm{b}}^{num} \approx \alpha^{(p)} P(\vec{r}_q). \quad (6b)$$

TABLE III. The notations employed with respect to Eq. (21): we apply $I_\tau^{(\mathscr{M})} = 0$ because $\mathscr{M}(\vec{r})$ does not vary along $\vec{1}_\tau$ in our computations, and set $I_n^{(\mathscr{M})} = 1$ for the normal mass-source variation with all schemes except the basic ones: MR = {FLI, FMR, DFLI}. The MR_n only implies $I_n^{(\mathscr{M})} = 1$ in Eqs. (17)–(24b), without any reconstruction step. The A-LSOB from Eq. (12) adopts the same notations: T-PP_i and T-DFLI_i with $i = r$ [when "RM" from Eq. (20) is applied in all nodes] or $i \in \{1, 2, 3, 4\}$ [when Eq. (20) is optionally applied only in nodes with a single cut link].

Equation (21)	**MR**	MR_n	N-MR_r	N-MR_1	N-MR_2	N-MR_3	N-MR_4
$I_n^{(\mathscr{M})}$	0	1	1	1	1	1	1
I_τ	0	0	1	1	1	1	1
Equation (17) with Eq. (19a)						$q = 3$	$q = 4$
Equation (17) with Eq. (19b)				$q = 1$	$q = 2$		
Equation (17) with Eq. (20)			✓				

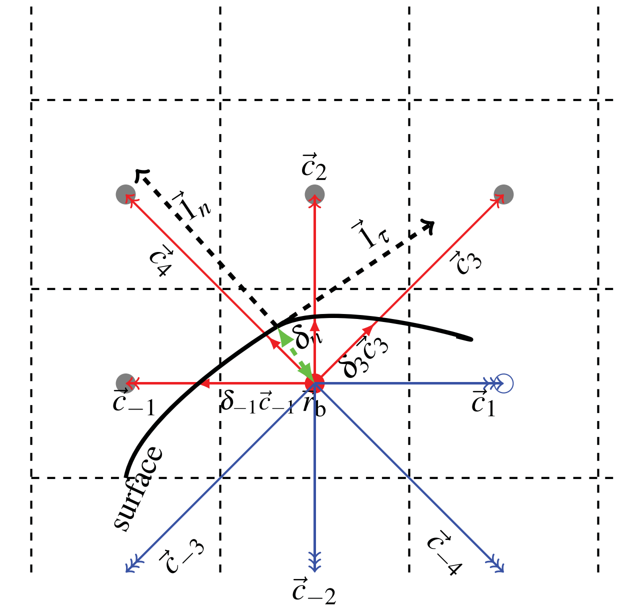

FIG. 1. Sketch for d2q9 boundary node $\vec{r}_{\rm b}$: wall-cut links are $\{\vec{c}_{-1}, \vec{c}_2, \vec{c}_3, \vec{c}_4\}$; unknown populations are $\{f_1, f_{-2}, f_{-3}, f_{-4}\}$; The MR and N-MR operate the delimiting surface with the directional distances $\delta||\vec{c}_q||$. The A-LSOB builds the Taylor closure relation along $\vec{1}_n$ for a distance δ_n. We consider a single surface bisection $\vec{r}_n(\vec{r}_{\rm b}) = \vec{r}_{\rm b} + \delta_n \vec{1}_n$.

The Dirichlet family contains an infinite number of members parametrized by the link-wise free parameter $\alpha^{(p)}$; the MPLI family improves LI schemes[25,62] for parametrization and includes one of three schemes,[62] called LMKC; the PLI family corrects MPLI for the cut link projection of the advective gradient $t_q^{(a)}\partial_q(P\vec{u}\cdot\vec{c}_q)$, e.g., in a grid-inclined or interface-perpendicular velocity field. The PP family is exact on the piece-wise parabolic profiles in the presence of the uniform grid-rotated velocity field; the two-node KMR1 and the novel single-node PPLI retain this accuracy in grid-rotated diffusion slabs and the grid-aligned advection velocity. The coefficients of the linear and parabolic Dirichlet MR are exemplified in Tables X and XII, respectively. The members of the same family produce identical stationary solutions provided that their effective steady-state closure relations, exactly expressed through $e_q^{\pm}$ and $n_q^{\pm}$, are equivalent; their coefficients can be found in Table XIII, whereas those of their approximation with Eq. (5) are gathered in Table XIV. The Dirichlet schemes are classified in Table I.

The MR_q coefficients of the advective-diffusive flux FLI and FMR schemes are presented in Table XV, those for an infinite diffusive-flux family DFLI in Table XVI; the internal coefficients of the stationary closure are all gathered in Table XVII, and those of the second-order accurate approximation with Eq. (5) are specified in Table XVIII. The one-node FLI and the two-node FMR fit CL_q to the directional Taylor expansion for the projection of the advective-diffusive flux $\vec{\Phi}(\vec{r})$:

$$\mathrm{FLI/FMR}: \alpha^{(u)}(\Phi_q + \delta\partial_q\Phi_q)|_{\vec{r}_{\rm b}}^{num} \approx \alpha^{(u)}\Phi_q(\vec{r}_q), \tag{7a}$$

$$\begin{aligned}\Phi_q^{num}(\vec{r}_{\rm b}) &:= t_q^{(a)}P\vec{u}\cdot\vec{c}_q - t_q^{(m)}\mathscr{D}\partial_q P|_{\vec{r}_{\rm b}}^{num},\\ \Phi_q(\vec{r}_q) &:= t_q\vec{\Phi}(\vec{r}_q)\cdot\vec{c}_q,\ \vec{\Phi} := \vec{u}P - \mathscr{D}\nabla P.\end{aligned} \tag{7b}$$

The *flux linear interpolation* (FLI) reduces to the BB for half-distance $\delta = \frac{1}{2}$; the FMR improves FLI for the parabolic advection term $\gamma^{(u)}t_q^{(a)}\partial_q^2(P\vec{u}\cdot\vec{c}_q)$ in Eq. (5); the scale factor $\alpha^{(u)}$ is fixed in these two schemes. Typically, the boundary accommodation simplifies with the same weight $t_q^{(m)} = t_q^{(a)} = t_q$ in Eq. (2). In turn, the *diffusive-flux* MR DFLI family vanishes all advection terms in Eq. (5) and it prescribes the linear continuation of the diffusive flux governed by an arbitrary linkwise scale factor β':

$$\mathrm{DFLI}: \beta'(D_q + \delta\partial_q D_q)|_{\vec{r}_{\rm b}}^{num} \approx \beta' D_q(\vec{r}_q), \tag{8a}$$

$$\begin{aligned}D_q^{(num)}(\vec{r}_{\rm b}) &\approx -t_q^{(m)}\mathscr{D}\partial_q P|_{\vec{r}_{\rm b}}^{num},\\ D_q(\vec{r}_q) &:= t_q^{(m)}\vec{D}(\vec{r}_q)\cdot\vec{c}_q,\ \vec{D} := -\mathscr{D}\nabla P.\end{aligned} \tag{8b}$$

The MR_q schemes are quite natural for LBM because they supply the unknown populations directly, the BB alike. However, Eqs. (7) and (8) need to prescribe not only the normal (physical) flux component $\Phi_n(\vec{r}_q)$ but also its (unknown *a priori*) tangential component $\Phi_\tau(\vec{r}_q)$, given that $\Phi_q(\vec{r}_q) = (\Phi_\tau, \Phi_n)\cdot\vec{c}_q$ with $\vec{\Phi} = \Phi_\tau\vec{1}_\tau + \Phi_n\vec{1}_n$, in the unit (tangential, normal) surface-aligned coordinate system $(\vec{1}_\tau, \vec{1}_n)|_{\vec{r}_q}$ traced at the bisection point $\vec{r}_q = \vec{r}_{\rm b} + \delta_q\vec{c}_q$ of the cut link and a given surface; Fig. 2 illustrates flux decomposition for a constant flux $\vec{\Phi}$ prescribed on the flat grid-inclined surface.

Hence, one of our objectives is to relax *the continuation of* $\Phi_\tau\vec{1}_\tau\cdot\vec{c}_q$ and $D_\tau\vec{1}_\tau\cdot\vec{c}_q$ from the closure relation CL_q in the normal N-MR flux schemes, where MR_q in Eq. (4) becomes replaced by MR_{qn}:

$$\mathrm{N\text{-}MR}: \mathrm{MR}_{qn} = \mathrm{MR}_q - \mathrm{CL}_{q\tau}. \tag{9}$$

When Eq. (5) is expressed in the 2D rotated frame $(\vec{1}_\tau, \vec{1}_n)|_{\vec{r}_q}$ using decomposition $\vec{u}(\vec{r}_{\rm b}) = \{u_\tau, u_n\}$ and $\vec{c}_q = \{c_{q\tau}, c_{qn}\}$, the $\mathrm{CL}_{q\tau}$ reads

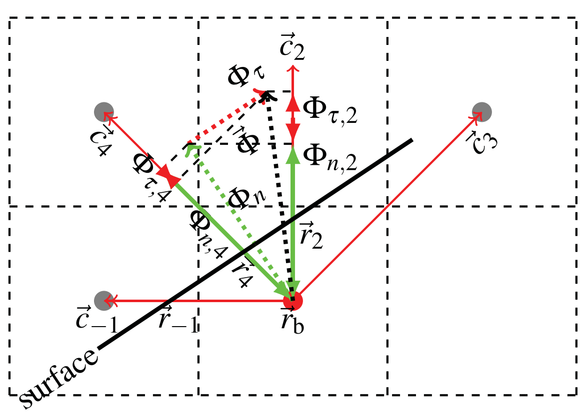

FIG. 2. Sketch for a uniform boundary flux $\vec{\Phi} = \Phi_n\vec{1}_n + \Phi_\tau\vec{1}_\tau$ and its directional projections $\Phi_q = \Phi_{nq} + \Phi_{\tau q}$, with $\Phi_{nq} = \Phi_n\vec{1}_n\cdot\vec{c}_q$ and $\Phi_{\tau q} = \Phi_\tau\vec{1}_\tau\cdot\vec{c}_q$, specified for $q=2$ and $q=4$ on the flat grid-rotated surface. The MR prescribes $\Phi_q(\vec{r}_q)$; the N-MR prescribes $\Phi_{nq}(\vec{r}_q)$; the A-LSOB prescribes $\Phi_n(\vec{r}_n)\vec{1}_n$.

$$\mathrm{CL}_{q\tau}(P, u_\tau P) = \alpha^{(u)} t_q^{(a)} u_\tau P c_{q\tau} + \beta^{(p)} t_q^{(m)} c_e \partial_\tau P c_{q\tau} + \beta^{(u)} t_q^{(a)} \Big[\partial_\tau (u_\tau P) c_{q\tau}^2 + \partial_n (u_\tau P) c_{q\tau} c_{qn}\Big] + \gamma^{(p)} t_q^{(m)} c_e \Big[\partial_{\tau\tau}^2 P c_{q\tau}^2 + \partial_{\tau n}^2 P c_{q\tau} c_{qn}\Big] + \gamma^{(u)} t_q^{(a)} \times \Big[\partial_{\tau\tau}^2 (u_\tau P) c_{q\tau}^3 + 2\partial_{\tau n}^2 (u_\tau P) c_{q\tau}^2 c_{qn} + \partial_{nn}^2 (u_\tau P) c_{q\tau} c_{qn}^2\Big]\Big|_{\vec{r}_b}^{(num)}. \quad (10)$$

Linear formulation assumes that $\vec{u}(\vec{r})$ is independent of $P(\vec{r})$. Equation (10) can be then readily expressed through the local vector $\mathbf{Y}[5]$:

$$2\mathrm{d}: \mathbf{Y}[5] = \{\partial_\tau P, \partial_n P, \partial_{\tau\tau}^2 P, \partial_{nn}^2 P, \partial_{\tau n}^2 P\}|_{\vec{r}_b}^{(num)}. \quad (11)$$

The idea is to reconstruct $\mathbf{Y}[5]$ locally, based on the in-node LSOB approach,[21,87] and to compute $\mathrm{CL}_{q\tau}(P, u_\tau P)$ explicitly; the one-node N-MR, as N-FLI, then remains local but it loses its directional implementation.

The alternative *in-node* A-LSOB approach assumes the surface-aligned $(\vec{1}_\tau, \vec{1}_n)|_{\vec{r}_n}$ unit coordinate system to be traced at the bisection point $\vec{r}_\mathrm{n}(\vec{r}_\mathrm{b}) = \vec{r}_\mathrm{b} + \delta_n \vec{1}_n$ (see Figs. 1 and 2), and it employs the reconstructed nodal derivatives to build the parabolic-accurate Taylor closure relation along the normal direction from $\vec{r}_\mathrm{b}$ to $\vec{r}_\mathrm{n}$ for Dirichlet [T-PP], diffusive flux [T-DFLI] and advective-diffusive flux [T-FLI]:

$$\text{T-PP}: P(\vec{r}_\mathrm{b}) + \sum_{m=1}^{2} \frac{\delta_n^m}{m!} \partial_n^m P|_{\vec{r}_b}^{(num)} = P(\vec{r}_\mathrm{n}), \quad (12a)$$

$$\text{T-DFLI}: \mathscr{D} \sum_{m=1}^{2} \frac{\delta_n^{(m-1)}}{(m-1)!} \partial_n^m P|_{\vec{r}_b}^{(num)} = P(\vec{r}_\mathrm{n}), \quad (12b)$$

$$\text{T-FLI}: (u_n(\vec{r}_\mathrm{b}) \times \text{T-PP}) + \text{T-DFLI} = \Phi_n(\vec{r}_n), \quad \text{where } \vec{r}_n = \vec{r}_\mathrm{b} + \delta_n \vec{1}_n. \quad (12c)$$

Assuming a constant normal velocity u_n, Eq. (12c) computes the advection component $u_n P$ with P replaced by the LHS of Eq. (12a); Eq. (12c) reduces to Eq. (12b) when the normal velocity u_n is zero (typically on the solid wall), or when u_n and P are continuous on the interface provided that scalar-field continuity is prescribed with Eq. (12a). An extension to space-variable $u_n(\vec{r})$ is straightforward giving its normal Taylor expansion.

At this point, we should recognize that the A-LSOB extension to interface is less evident than with the MR, because the interface points $\{\vec{r}_n\}$ do not overlap, except for a grid-aligned interface. For that reason, the Taylor schemes will be only considered for grid-rotated walls and grid-aligned interface.

The flux schemes are summarized in Table II; just to fix ideas, we propose to "interpret" FLI and FMR as the linearly and parabolically interpolated BB, whereas T-DFLI and DFLI can be thought as the local and back-sided extrapolations of the diffusive flux and its non-equilibrium term, respectively. We will show that these internal characteristics determine their mass-balance properties.

C. Local reconstruction

The reconstruction procedure restores the first- and second-order derivatives from the non-equilibrium solution based on the LSOB ideas.[21,87] We demonstrate this procedure for TRT operator, but it extends under the symmetry argument[32,40] for any standard isotropic or anisotropic collision matrix, giving the associated third-order accurate Chapman–Enskog non-equilibrium solution.

1. Reconstruction with the TRT collision

The TRT update applies in the following form:

$$f_j(\vec{r} + \mathrm{sgn}_j \vec{c}_q, t+1) = f_j(\vec{r}, t) + \hat{n}_q^+(\vec{r}, t) + \mathrm{sgn}_j \hat{n}_q^-(\vec{r}, t), \quad \forall j \in Q_{\frac{1}{2}} \cup Q_{-\frac{1}{2}}, \ q = j\mathrm{sgn}_j, \ q \in Q_{\frac{1}{2}}, \quad \{\vec{r}, \vec{r} + \mathrm{sgn}_j \vec{c}_q\} \in V_p, \ \text{with} \quad (13a)$$

$$\hat{n}_q^\pm := -\frac{1}{\tau^\pm}(f_q^\pm - e_q^\pm), \ f_q^\pm := \frac{1}{2}(f_q \pm f_{-q}); \quad f_0(\vec{r}, t+1) = f_0(\vec{r}, t) + \hat{n}_0^+(\vec{r}, t), \quad \hat{n}_0^+ := \mathscr{M}(\vec{r}, t) - 2\sum_{q=1}^{Q-1} \hat{n}_q^+(\vec{r}, t). \quad (13b)$$

We assume hereafter that Eq. (2) incorporates the mass-source $\mathscr{M}(\vec{r}, t)$ and re-defines the scalar-field solution $P(\vec{r})$ with $\frac{1}{2}\mathscr{M}$:

$$e_q^+(\vec{r}) := t_q^{(m)} c_e P^{eq}, \ P^{eq} = P(\vec{r}) + \Lambda^+ \mathscr{M}(\vec{r}), \quad (14a)$$

$$e_q^-(\vec{r}) := t_q^{(a)} P \vec{u} \cdot \vec{c}_q, \ P = \sum_{q=0}^{Q_m} f_q + \frac{1}{2}\mathscr{M}, \quad (14b)$$

$$\Lambda^\pm(\vec{r}) := \left(\tau^\pm(\vec{r}) - \frac{1}{2}\right), \ \Lambda(\vec{r}) = \Lambda^+(\vec{r})\Lambda^-(\vec{r}). \quad (14c)$$

A free-tunable collision parameter $\Lambda(\vec{r})$ should remain fixed to obtain the same steady-state solution for any diffusion coefficient $\mathscr{D}_0 = c_e \Lambda^-$ given the grid Péclet number $\mathscr{U}/\mathscr{D}_0$ and, in general case, c_e value. At steady-state, the non-equilibrium solution obeys the recurrence equations[40,51] exactly expressed through the directional central-differences: $\bar{\Delta}_q \psi(\vec{r}) = \frac{1}{2}(\psi(\vec{r} + \vec{c}_q) - \psi(\vec{r} - \vec{c}_q))$ and $\bar{\Delta}_q^2 \psi(\vec{r}) = \psi(\vec{r} + \vec{c}_q) - 2\psi(\vec{r}) + \psi(\vec{r} - \vec{c}_q)$, as

$$\text{RE-a}: \hat{n}_q^\pm = \bar{\Delta}_q e_q^\mp - \Lambda^\mp \bar{\Delta}_q^2 e_q^\pm + \left(\Lambda - \frac{1}{4}\right) \bar{\Delta}_q^2 \hat{n}_q^\pm, \quad (15a)$$

$$\text{RE-b}: \bar{\Delta}_q^2 e_q^\pm - \Lambda^\pm \bar{\Delta}_q^2 \hat{n}_q^\pm - \bar{\Delta}_q \hat{n}_q^\mp = 0, \quad (15b)$$

$$\text{RE-c}: \Lambda^\mp \hat{n}_q^\mp = \Lambda^\mp \bar{\Delta}_q e_q^\pm - \frac{1}{4} \bar{\Delta}_q^2 e_q^\pm - \left(\Lambda - \frac{1}{4}\right) \bar{\Delta}_q \hat{n}_q^\mp. \quad (15c)$$

Equation (15c) is obtained by expressing $\bar{\Delta}_q^2 \hat{n}_q^\pm$ from RE-b and inserting it into RE-a. We restrict RE-a to its second-order accurate approximation [A-RE]:

$$\text{A} - \text{RE}: \hat{n}_q^{\pm(2)} \approx \partial_q e_q^\mp - \Lambda^\mp \partial_q^2 e_q^\pm, \ \forall \vec{r}. \quad (16)$$

Giving the post-collision solution $\hat{n}_q^\pm$ at boundary node $\vec{r}_\mathrm{b}$ or at interface node $\vec{r}_i$, $\mathbf{Y}[5]$ from Eq. (11) solves the local linear system:

$$\mathbf{B} \cdot \mathbf{Y}[5] = \mathbf{R}, \ \mathbf{B} = \{B_{q,j}^\pm\}, \ B_{q,j}^\pm = \partial_{Y_j} \hat{n}_q^{\pm(2)}, \quad (17a)$$

$$\mathbf{R} = \{R_q^\pm\}, \ R_q^\pm = \hat{n}_q^\pm - \hat{n}_q^{\pm(2)}|_{\mathbf{Y}=0}, \quad (17b)$$

$$\mathbf{Y}[5] = \mathbf{B}^{-1}\mathbf{R}. \quad (17c)$$

The term $\hat{n}_q^{\pm(2)}|_{\mathbf{Y}=0}$ may differ from zero when $\vec{u}(\vec{r})$ and/or $\mathscr{M}(\vec{r})$ vary in space, e.g., $\hat{n}_q^{\pm(2)}|_{\mathbf{Y}=0}$ includes $P(\vec{r}_{\rm b},t)\partial_q\vec{u}\cdot\vec{c}_q$ and $P(\vec{r}_{\rm b},t)\partial_q^2\vec{u}\cdot\vec{c}_q$ in a parabolic velocity profile.

Remark. In the transient case, the RHS in Eq. (16) sums with $\partial_t e_q^{\pm}(\vec{r},t)$ which can be estimated locally from $\hat{n}_0(\vec{r},t)\propto\partial_t P(\vec{r},t)$.

2. Reconstruction in constant velocity field

Let us illustrate the reconstruction procedure for a constant velocity field $\vec{u}=(u_\tau,u_n)$. When the mass-source is set piece-wise constant, Eq. (16) becomes

$$\begin{aligned}\hat{n}^{+(2)}(P,\vec{u}P) &= t_q^{(a)}(c_{qn}u_n+c_{q\tau}u_\tau)(c_{qn}\partial_n P+c_{q\tau}\partial_\tau P)\\ &\quad -t_q^{(m)}c_e\Lambda^-\times(c_{qn}^2\partial_{nn}^2P+2c_{qn}c_{q\tau}\partial_{\tau n}^2P+c_{q\tau}^2\partial_{\tau\tau}^2P),\end{aligned}\tag{18a}$$

$$\begin{aligned}\hat{n}^{-(2)}(P,\vec{u}P) &= t_q^{(m)}c_e(c_{qn}\partial_n P+c_{q\tau}\partial_\tau P)-t_q^{(a)}\Lambda^+(c_{qn}u_n+c_{q\tau}u_\tau)\\ &\quad\times(c_{qn}^2\partial_{nn}^2P+2c_{qn}c_{q\tau}\partial_{\tau n}^2P+c_{q\tau}^2\partial_{\tau\tau}^2P),\end{aligned}\tag{18b}$$

$$\begin{aligned}&\text{with }\vec{1}_\tau=(\cos[\theta],\,\sin[\theta])\,,\ \vec{1}_n=(-\sin[\theta],\,\cos[\theta])\,.\\ &c_{q\tau}=\vec{c}_q\cdot\vec{1}_\tau\,,\ c_{qn}=\vec{c}_q\cdot\vec{1}_n.\end{aligned}\tag{18c}$$

Giving the four non-complanar d2q9 velocities, as: $\vec{c}_1=(1,0)$, $\vec{c}_2=(0,1)$, $\vec{c}_3=(1,1)$, $\vec{c}_4=(1,-1)$, the d2q9 operates with four independent couples $\{\hat{n}_q^+,\hat{n}_q^-\}$, $q\in Q_{\frac{1}{2}}$; they reduce to two coordinate pairs with d2q5. The d2q9 allows us to reconstruct the five components of $\mathbf{Y}[5]$; recall, they are required for $\mathrm{CL}_{q\tau}$ in Eq. (10) and also by the A-LSOB, to prescribe all incoming populations with Eq. (16). Hence, we have to select 5 components $\hat{n}_q^{\pm}$ from their 4×2 available values. We consider first two groups, I and II, each formed by two particular square subsets, as Ia and Ib. Group I prescribes $\{\hat{n}_q^+,\hat{n}_q^-\}$ for the two coordinates links, and $\hat{n}_q^+$ for one of the two diagonal links. Inversely, group II prescribes $\{\hat{n}_q^+,\hat{n}_q^-\}$ for the two diagonal links and $\hat{n}_q^+$ for one of the two coordinate links:

$$\begin{aligned}&\mathrm{I}:\hat{\mathbf{n}}[5]=\{\hat{n}_1^+,\hat{n}_1^-,\hat{n}_2^+,\hat{n}_2^-\}\cup\hat{n}_q^+\,,\,q=3(a)\text{ or }q=4(b):\\ &|\det[\mathbf{B}]|=2t_d^{(m)}c_e\Lambda^-\times|\Pi_{j=1}^{j=2}(t_c^{(m)2}c_e^2\Lambda^--t_c^{(a)2}\Lambda^+(\vec{u}\cdot\vec{c}_j)^2)|,\end{aligned}\tag{19a}$$

$$\begin{aligned}&\mathrm{II}:\hat{\mathbf{n}}[5]=\{\hat{n}_3^+,\hat{n}_3^-,\hat{n}_4^+,\hat{n}_4^-\}\cup\hat{n}_q^+\,,\,q=1(a)\text{ or }q=2(b):\\ &|\det[\mathbf{B}]|=8t_c^{(m)}c_e\Lambda^-\times|\Pi_{j=3}^{j=4}(t_d^{(m)2}c_e^2\Lambda^--t_d^{(a)2}\Lambda^+(\vec{u}\cdot\vec{c}_j)^2)|.\end{aligned}\tag{19b}$$

The determinant is specified in system (18), it has the same magnitude $|\det[\mathbf{B}]|$ inside each group and it is different from zero unless when the d2q9 reduces to d2q5 in group I $[t_d^{(m)}=0]$ or to d2q5^{rot} in group II $[t_c^{(m)}=0]$. It is also to note that the subset II shall be preferred in the straight situation for the sake of the symmetry. Equation (B2a) and (B2b) display the alternative reconstructions, when the fifth component $\hat{n}_q^+$ is replaced by $\hat{n}_q^-$; however, then, $\det[\mathbf{B}]=0$ if $\vec{u}$ is complanar with the diagonal or coordinate direction $\vec{c}_q$, respectively.

We note that regardless the wall inclination or surface curvature, Eq. (18) can be expressed in the Cartesian coordinate system through $\mathbf{Y}_0[5]=\{\partial_xP,\partial_yP,\partial_{xx}^2P,\partial_{yy}^2P,\partial_{xy}^2P\}$. When $\mathbf{Y}_0[5]$ is derived from Eq. (17), $\mathbf{Y}_0[5]$ gets the same solution as that using the inclined system in Eq. (17) with the help of the posterior mapping given in Eq. (B1). The fixed coordinate system may lead to a simplified implementation when $(\vec{1}_\tau,\vec{1}_n)$ vary along the wall, as for example when the N-MR applies on the curved surface (see also[87]) When the velocity or mass-source varies in space, Eq. (18) becomes modified according to Eq. (16); Eqs. (B3)–(B5) then exemplify the parabolic fields using the subset II.

Finally, the whole rectangular matrix ("RM" hereafter) can be pseudo-inverted in Eq. (17):

$$\begin{aligned}&\mathrm{RM}'':\mathbf{B}[8\times5]\cdot\mathbf{Y}[5]=\mathbf{R}[8]\,,\ \mathbf{R}=\hat{\mathbf{n}}-\hat{\mathbf{n}}^{\pm}(2)|_{\mathbf{Y}=0}\,,\\ &\hat{\mathbf{n}}[8]=\cup_{q=1}^{q=4}\{\hat{n}_q^{\pm}\}.\end{aligned}\tag{20}$$

Equation (20) prescribes all 8 post-collision values regardless the local geometry. The "RM" approach is then simpler and it naturally retains the underlying symmetry. One can also restrict "RM" to $\hat{\mathbf{n}}[6]$, e.g., giving four coordinate values and two diagonal values. The rectangular system can be solved with the help of the singular-value decomposition method following;[21,23] in this work, the most suitable (least-square) approximate is automatically provided by the linear solver of the symbolic tool. The obtained solution is exact when Eq. (16) satisfies the system exactly. We will find that on the one side, the rectangular reconstruction is algorithmically simpler than the square one; on the other side, it is only approximate and then it does not maintain the bulk parametrization exactly, in general cases.

D. The N-MR flux schemes

Giving that $\mathbf{Y}[5]$ is reconstructed with Eq. (17), the N-MR applies the correction $\mathscr{E}_q^{(-)}(\vec{r}_{\rm b},t)$ to the MR rule as

$$\begin{aligned}&f_{-q}(\vec{r}_{\rm b},t+1)=(\mathrm{MR}_q-\mathscr{E}_q^{(-)})(\vec{r}_{\rm b},t)+w_q(\vec{r}_q,\tilde{t})\,,\\ &\mathscr{E}_q^{(-)}=I_\tau\mathrm{CL}_{q\tau}(P,u_\tau P)+I_\tau^{(\mathscr{M})}\mathrm{CL}_{q\tau}(\Lambda^+\mathscr{M},0)\\ &\quad+I_n^{(\mathscr{M})}\mathrm{CL}_{qn}(\Lambda^+\mathscr{M},0)\,,\\ &\{I_\tau,I_\tau^{(\mathscr{M})},I_n^{(\mathscr{M})}\}\in\{0,1\}.\end{aligned}\tag{21}$$

We distinguish three optional and independent directional corrections: $\mathrm{CL}_{q\tau}(P,u_\tau P)$ for the tangential projection of the advective-diffusive flux; $\mathrm{CL}_{q\tau}(\Lambda^+\mathscr{M},0)$ and $\mathrm{CL}_{qn}(\Lambda^+\mathscr{M},0)$ for the tangential and normal variation of the mass-source. The boundary term $w_q(\vec{r}_q,\tilde{t})$ prescribes the projection of $\Phi_n\vec{1}_n$ or $D_n\vec{1}_n$, respectively,

$$\mathrm{FLI/FMR}:\ w_q(\vec{r}_q,\tilde{t})=-\alpha^{(u)}t_q\Phi_n\vec{1}_n(\vec{r}_q,\tilde{t})\cdot\vec{c}_q\,;\tag{22a}$$

$$\mathrm{DFLI}:\ w_q(\vec{r}_q,\tilde{t})=-\beta' t_q^{(m)}D_n\vec{1}_n(\vec{r}_q,\tilde{t})\cdot\vec{c}_q.\tag{22b}$$

When $I_\tau=1$, Eq. (5) reproduces the directional Taylor expansion for the link projection of the normal flux Φ_{nq} or D_{nq}, and Eqs. (7) and (8) then read as, accordingly,

$$\begin{aligned}&\text{N-FLI/N-FMR}:\alpha^{(u)}(\Phi_{nq}+\delta\partial_q\Phi_{nq})|_{\vec{r}_{\rm b}}^{(num)}\approx\alpha^{(u)}\Phi_{nq}(\vec{r}_q)\,,\\ &\Phi_{nq}^{(num)}:=t_q^{(a)}u_nc_{qn}-t_q^{(m)}\mathscr{D}\partial_nPc_{qn}|^{(num)}\,,\\ &\Phi_{nq}:=t_q\Phi_n\vec{1}_n\cdot\vec{c}_q=t_q\Phi_nc_{qn}\,;\end{aligned}\tag{23a}$$

and

$$\begin{aligned}&\text{N-DFLI}:\beta'(D_{nq}+\delta\partial_qD_{nq})|_{\vec{r}_{\rm b}}^{(num)}\approx\beta' D_{nq}(\vec{r}_q)\,,\\ &D_{nq}^{(num)}:=-t_q^{(m)}\mathscr{D}\partial_nPc_{qn}\,,\\ &D_{nq}:=t_q^{(m)}D_n\vec{1}_n\cdot\vec{c}_q=t_q^{(m)}D_nc_{qn}.\end{aligned}\tag{23b}$$

When $\mathscr{M}(\vec{r})$ varies, its tangential and normal variations modify the flux closure condition, and they can be removed from it in Eq. (21), e.g., giving their (known) derivatives:

$$\mathrm{CL}_{q\tau}(\Lambda^+\mathscr{M},0) = t_q^{(m)}\Lambda^+ c_e\Big[\beta^{(p)}\partial_\tau \mathscr{M} c_{q\tau} + \gamma^{(p)}(\partial^2_{\tau\tau}\mathscr{M} c^2_{q\tau} + \partial^2_{n\tau}\mathscr{M} c_{q\tau}c_{qn})\Big], \quad (24a)$$

$$\mathrm{CL}_{qn}(\Lambda^+\mathscr{M},0) = t_q^{(m)}\Lambda^+ c_e\Big[\beta^{(p)}\partial_n \mathscr{M} c_{qn} + \gamma^{(p)}(\partial^2_{nn}\mathscr{M} c^2_{qn} + \partial^2_{\tau n}\mathscr{M} c_{q\tau}c_{qn})\Big]. \quad (24b)$$

The role of the mass-source corrections diminishes when $c_e \to 0$, but in principle, they should also complement the MR in Eq. (A1) following Eq. (21). Their main configurations that will be employed in this work are labeled in Table III.

E. Transient algorithms with the MR, N-MR, and A-LSOB

The boundary algorithms MR, N-MR, and A-LSOB may cope with any linear ADE collision but they are elaborated with the TRT operator, because it naturally provides the symmetric and anti-symmetric post-collision components $\hat{n}_q^{\pm}$, which are used by the MR corrective term $\hat{F}_q$ in Eqs. (A1) and (A2) and by the reconstruction in Eqs. (17) and (20). Assume that the populations $f_q(\vec{r}, t=0)$ are initialized in fluid nodes $\vec{r} \in V_p$. The iterative TRT algorithm then consists of the following steps:

1. Compute the equilibrium components $e_q^{\pm}(\vec{r}, t)$ including the mass source term $\Lambda^+\mathscr{M}(\vec{r}, t)$ into e_q^+, e.g., using Eq. (14).
2. Compute the post-collision populations $\hat{f}_q(\vec{r}, t) = f_q(\vec{r}, t) + \hat{n}_q^+(\vec{r}, t) + \hat{n}_q^-(\vec{r}, t)$ with the TRT operator (13) in all fluid nodes; store $\hat{n}_q^{\pm}(\vec{r}_b)$ in the boundary nodes $\vec{r}_b$.
3. Perform the streaming and update all neighbor "fluid" populations: $f_q(\vec{r} + \vec{c}_q, t+1) = \hat{f}_q(\vec{r}, t)$; store $\hat{f}_q(\vec{r}, t)$ temporarily in the boundary nodes $\vec{r}_b$, e.g., with the BB rule: $f_{-q}(\vec{r}_b, t+1) = \hat{f}_q(\vec{r}_b, t)$.
4. Perform the boundary update in all boundary nodes $\vec{r}_b$.
   Note: using the time-explicit formulation in Eq. (A2), the unknown populations $f_{-q}(\vec{r}_b, t+1)$ can be computed before the streaming step using the pre-collision solution $f_q(\vec{r}, t)$.
5. Go to step 1 unless the stop criteria is reached.

I. Boundary update using the MR and N-MR. The MR computes unknown populations $f_{-q}(\vec{r}_b, t+1)$ with Eq. (A1) [or Eq. (A2)]:

1. Pre-select the MR rule for wall-cut link q, e.g., the Neumann FLI/FMR/DFLI from Table XV or the Dirichlet, linear MPLI/PLI from Table X or the parabolic PP/KMR1 from Table XI. Prescribe its free-scale parameter ($\alpha_q^{(p)}$, $\alpha_q^{(u)}$ or β'_q); compute coefficients $\{\hat{\alpha}, \beta, \hat{\beta}, \gamma, \hat{\gamma}\}_q$ and the correction $\hat{F}_q$, giving the distance δ_q from $\vec{r}_b$ to the wall cut link bisection point $\vec{r}_q$.
2. Prescribe the boundary term $w_q(\vec{r}_q, \tilde{t})$, e.g., with Eq. (22) in the Neumann rule, or with Eq. (A4) in the Dirichlet rule.
3. Compute $f_{-q}(\vec{r}_b, t+1)$ according to Eq. (A1).
4. If $\mathscr{M}(\vec{r})$ varies in space, it is recommended to compute its normal $\mathrm{CL}_{qn}(\Lambda^+\mathscr{M}, 0)$ and tangential $\mathrm{CL}_{q\tau}(\Lambda^+\mathscr{M}, 0)$ corrections with Eq. (24), and to subtract them from $f_{-q}(\vec{r}_b, t+1)$ following Eq. (21).
5. If the tangential-flux N-MR correction is not needed, go to the next cut link $q(\vec{r}_b)$. Otherwise, the N-MR correction $\mathrm{CL}_{q\tau}(P, u_\tau P)$ is to be computed after the reconstruction step and subtracted from $f_{-q}(\vec{r}_b, t+1)$ with Eq. (21) for all Neumann cut links $q(\vec{r}_b)$.
6. Go to the next boundary node when all values $f_{-q}(\vec{r}_b, t+1)$ are updated.

Note: In this work only a constant flat-surface boundary flux is simulated, where the flux boundary values Φ_n and D_n in Eqs. (22)–(23) can be set equal to $\Phi_n(\vec{r}_n)$ and $D_n(\vec{r}_n)$, respectively (see Fig. 2). This enables us to perform one reconstruction procedure per boundary node in the wall-aligned coordinate system. Otherwise, when $\Phi_n(\vec{r}_q)$ or the coordinate system $\{\vec{1}_\tau, \vec{1}_n\}(\vec{r}_q)$ varies along the surface, the N-MR may perform the reconstruction in the Cartesian coordinates, applying then the individual mapping from Eq. (B1) to compute the term of $\mathscr{E}_q^{(-)}$ in Eq. (21) for the given cut link.

The reconstruction step can be performed as the following:

1. Select a subset $\hat{n}_q^{\pm}$ for the square reconstruction of $\mathbf{Y}(\vec{r}_b)$ (e.g., with Eq. (19)), unless when the rectangular reconstruction is applied with Eq. (20) giving all Q_m values $\hat{n}_q^{\pm}$.
2. Select the coordinate system, e.g., the Cartesian or the wall-aligned $(\vec{1}_\tau, \vec{1}_n)|_{\vec{r}_q}$, and to express Eq. (16) with it. Compute the matrix entries $\mathbf{B}(\vec{r}_b, t)$ and the right-hand-side (RHS) vector $\{\hat{n}_q^{\pm(2)}(\vec{r}_b, t)|_{\mathbf{Y}=0}\}$ in Eq. (17); the examples are provided by Eqs. (18) and (B3).
   Note: The matrix $\mathbf{B}$ and $\{\hat{n}_q^{\pm(2)}\}|_{\mathbf{Y}=0}$ can be precomputed prior to the iterative update provided that the relaxation rates, velocity and mass-source fields do not vary in time.
3. Compute vector $\mathbf{R}(\vec{r}_b, t)$ from $\{\hat{n}_q^{\pm}(\vec{r}_b, t)\}$ and solve Eq. (17) or Eq. (20) for $\mathbf{Y}(\vec{r}_b, t)$.

II. Boundary update using the A-LSOB. The A-LSOB prescribes the incoming population $f_{-q}(\vec{r}_b, t+1)$ with the second-order accurate Chapman-Enskog approximation:

$$f_{-q}(\vec{r}_b, t+1) = \Big[e_q^+ - e_q^- - \tau^+\hat{n}_q^{+(2)} + \tau^-\hat{n}_q^{-(2)}\Big]|_{\vec{r}_b}^{\tilde{t}}, \quad (25)$$

where $e_q^{\pm}$ depends upon an unknown value $P(\vec{r}_b, t+1)$; $\hat{n}_q^{\pm(2)}(\vec{r}_b, t)$ are computed with Eq. (16) after the **Reconstruction step**. The *Reconstruction step* shall, additionally, incorporate normal Taylor conditions from Eq. (12). For example, the Dirichlet closure equation from Eq. (12) can be either directly added to Eq. (17) or utilized to express $P(\vec{r}_b, t+1)$ through other unknowns. In the case of the Neumann rule (12 b), the definition of the unknown local variable $P(\vec{r}_b, t+1) = \sum_{q=0}^{Q_m} f_q(\vec{r}_b, t+1)$ can complement Eq. (17), by substituting their the updated populations $f_q(\vec{r}_b, t+1)$ and by expressing the incoming ones with Eq. (25); a similar procedure is exemplified by Eq. (3.6) in Ref. 87. When the Taylor closure or the local mass definition equation is added to Eq. (17), the unknown variable $P(\vec{r}_b, t+1)$ is inserted into $\mathbf{Y}(\vec{r}_b)$. Once $\mathbf{Y}(\vec{r}_b)$ is reconstructed, Eq. (25) is computed in the preselected coordinate system.

Note: Since Eq. (12b) inter-relates the two normal derivatives, the number of unknowns in $\mathbf{Y}(\vec{r}_b)$ can be reduced by one; in this way, the A-LSOB 2D flux schemes shall become available with the d2q5 scheme.

These A-LSOB transient algorithms are left however for future adaptation and validation. In this work, we focus on the development and application of the A-LSOB within the steady-state formulation.

F. Summary and extensions

Our starting point is the generic second-order accurate approximate of the closure relation in Eq. (5) associated with the one or two-point MR rule in Eqs. (A1) and (A2). Generalizing the common procedure, Eq. (5) includes not only the first-order equilibrium derivatives but also the second-order ones, and it also accounts for the non-equilibrium neighbor variation in two-point rules. The coefficients in Eq. (5) are provided in Sec. A for the Dirichlet and Neumann ADE rules, but they are also tabulated[40] for the Dirichlet velocity, pressure and normal stress LI and MR rules; the LI and MR also extend for the slip-flow regime.[85,86] Practically, any directional boundary or interface rule fits Eq. (5) with some coefficients; for example, the free-interface pressure/stress scheme[5] corresponds to the Dirichlet family MPLI($\alpha^{(p)} = -1$) [see Eq.(61) in Ref. 40].

We then identify the deficient projections in Eq. (5) for the given boundary rule; Eq. (10) exemplifies the deficient advective-diffusion tangential projection with respect to the normal Neumann flux condition in a constant velocity ADE. Once the deficient term is formulated, the idea is to re-build it from the in-node non-equilibrium solution $\hat{n}_q^{\pm}$, and to subtract it from the MR incoming population. Again, this type of correction can be built-in into any directional rule. The proposed algorithms are all summarized in Sec. II E and they do not need to resort to any off-grid interpolations. The subsequent analysis extends straightforwardly for any linear collision operator by replacing Eq. (16) by its associated Chapman-Enskog approximate.

The current reconstruction assumes that $e_q^{\pm}$ is linear with respect to the macroscopic variables, as the concentration, diffusive-flux variable (in the linear or non-linear ADE), or pressure and velocity in the fluid Stokes/Brinkmann flow modeling. The 2D ADE system then requires the restoring of the five derivatives; they are exemplified in the wall-aligned coordinate system by Eq. (11) but the coordinate system can be assigned arbitrarily, and it may vary from one node to another. We propose then either to preselect the five values $\hat{n}_q^{\pm}$ and to invert the square system in Eq. (17), or to give all Q_m values $\hat{n}_q^{\pm}$ and to (approximately) solve the rectangular system with Eq. (20). We note that the second strategy is geometry and problem independent, but it may not maintain exactly the TRT parametrization by the physical dimensionless numbers at fixed Λ. The reconstruction was introduced with the LSOB flow matrix method[21] and it has been recently optimized[87] with the 2D/3D TRT collision for Stokes flow. In turn, the A-LSOB closure equations (12) are formulated here as an alternative, normal Taylor single-node parabolic closure of the ADE system. Once the macroscopic variables and derivatives are reconstructed, the incoming populations are consequently prescribed by Eq. (16).

We note that the N-BB prototype of N-FLI was successfully applied[26] to release the tangential advective-diffusive flux, and hence to compute correctly the two first moments, in solute transition along the flat surface, and on the heterogeneous anisotropic interface.[28] The numerical simulations in this work will be performed with the steady-state formulation, which enables us to verify all new bounding techniques through a quite arbitrarily, parameter range (physical contrasts, Péclet number), without concerns from stability.[31,32,34,38,60,83] However, the transient MR ADE interface-conjugate has been also developped;[40,42] its update to N-MR is identical with the boundary counterpart, and it is exemplified with the steady-state interface-conjugate treatment in Sec. III D. The MR interface-conjugate is also formulated[40] for the velocity and normal-stress continuous flow conditions; their release from the tangential stress projection shell becomes possible following the N-MR path. Conversely, the LSOB approach demonstrates how to insert the physical, normal and tangential, free-surface flow stress conditions directly into the Chapman-Enskog multiple-relaxation-time (MRT) population reconstruction in the filling process, either at high Reynolds number[23] or for Bingham fluid.[24]

A preliminary MR analysis[22] demonstrated that the parabolic velocity scheme MR1 (which is the original flow counterpart of the Dirichlet scalar scheme KMR1 from Table XI) is much more accurate than the linear ones[6,91] not only for porous media later confirmed,[10,53] but also for the pressure fluctuations in a newborn fluid node, improving them for the mass conservation and the Galilean invariance in the static/moving frames. These properties have been recently carefully evaluated,[10,44,80] leading however partly to a different conclusion[80] on the competition between the linear CLI scheme[30] (which is in turn the flow counterpart of LMKC) and MR1. In our belief, the parabolic MR shall handle more accurately pressure fluctuations because MR vanishes the pressure terms of $\beta^{(p)}$ (as MR1) and also $\gamma^{(p)}$ (with new PM schemes[40]) in Eq. (5), which are both non-zero in the linear (LI) Dirichlet velocity schemes including their new member IPLI from Table XII.

Finally, it is well known that the local mass adjustment spoils body-fitted boundary rules.[90] Differently from a mechanical mass conservation account, the steady-state formulation will express it through the body-fitted global solvability condition, providing interesting hints for mass-balance properties of the linear and parabolic ADE flux schemes. We expect to extend this approach in a near future to flow schemes.

III. STEADY-STATE TRT FORMULATION

We recall the steady-state TRT formulation and specify its bulk-uniform M_0- solvability condition in Sec. III. The alternative corrective boundary-flux approach is introduced in Sec. III B. Section III C recasts stead-state MR and N-MR; Sec. III D applies them with the interface-conjugate; Sec. III E provides the steady-state MR, N-MR and A-LSOB algorithms; and Sec. III F resumes these techniques.

A. Bulk system

The TRT bulk steady system is composed from two equations per every internal link connecting $\vec{r} \in V_p$ and $\vec{r} + \vec{c}_q \in V_p$, $q \in Q_{\frac{1}{2}}$:

$$S_q(\vec{r}) = S_{-q}(\vec{r} + \vec{c}_q), \tag{26a}$$

$$G_q(\vec{r}) = -G_{-q}(\vec{r} + \vec{c}_q), \tag{26b}$$

with

$$\begin{aligned} S_q(\vec{r}) &= \left[e_q^+ + \frac{1}{2}\hat{n}_q^- - \Lambda^+ \hat{n}_q^+\right](\vec{r}), \\ S_{-q}(\vec{r} + \vec{c}_q) &= \left[e_q^+ - \frac{1}{2}\hat{n}_q^- - \Lambda^+ \hat{n}_q^+\right](\vec{r} + \vec{c}_q), \\ G_q(\vec{r}) &= \left[e_q^- + \frac{1}{2}\hat{n}_q^+ - \Lambda^- \hat{n}_q^-\right](\vec{r}), \\ -G_{-q}(\vec{r} + \vec{c}_q) &= \left[e_q^- - \frac{1}{2}\hat{n}_q^+ - \Lambda^- \hat{n}_q^-\right](\vec{r} + \vec{c}_q). \end{aligned} \tag{27a}$$

This system is complemented with the local mass-conservation equation given by

$$2\sum_{q=1}^{Q_m/2}\hat{n}_q^+(\vec{r}) = \mathscr{M}(\vec{r}) + M_0\,,\ \vec{r}\in V_p. \tag{28}$$

The global set of the unknowns Var in the linear system formed by Eqs. (26)–(28) reads

$$Var = M_0\cup_{\vec{r}\in V_p}(P(\vec{r})\cup\hat{\mathbf{n}}(\vec{r})), \tag{29a}$$

$$\hat{\mathbf{n}}(\vec{r}) = \cup_{q\in Q_{\frac{1}{2}}}\hat{n}_q^{\pm}(\vec{r}). \tag{29b}$$

When the grid is composed of N_p nodes, the set Var consists of $N_pQ_m+N_p+1$ variables. A single unknown variable M_0 is introduced to assure the solvability condition whenever the system is defined to an additive constant, so that one variable $P(\vec{r})$ can be fixed to arbitrary value. The solution is normalized *a posteriori*, as it typically happens when the system is closed by the Neumann or periodic conditions. In principle, the two notions: (i) the exact solvability condition of the steady-state system, and (ii), the preservation of the population mass (sum), are distinct for grid-shifted or shaped boundary. Indeed, the sums of the pre-collision and the post-collision populations are the same provided that $\sum_{\vec{r}}\mathscr{M}(\vec{r})=0$:

$$\sum_{\vec{r}}\sum_{q=0}^{Q_m}\hat{f}_q(\vec{r}) = \sum_{\vec{r}}\sum_{q=0}^{Q_m}f_q(\vec{r})\ \text{if only}\ \sum_{\vec{r}}\mathscr{M}(\vec{r})=0. \tag{30}$$

This condition assures the solvability condition with the BB or implicit periodic interface. At the same time, the exact solvability condition reads as $\langle\mathscr{M}(\vec{r})\rangle=\int_{\vec{r}}\mathscr{M}(\vec{r})dr=0$. In fact, when prescribing a mass-conserving source $\langle\mathscr{M}(\vec{r})\rangle=0$, the BB− system will find the following solution for M_0:

$$\mathrm{BB}:\ M_0N_p = \sum_{\vec{r}}\mathscr{M}(\vec{r}) - \langle\mathscr{M}(\vec{r})\rangle. \tag{31}$$

In other words, only when the boundary scheme is exact, or when $\mathscr{M}(\vec{r})$ obeys its discrete solvability condition, the obtained solution is $M_0=0$. It should be said that the M_0-mechanism is self-activated by the transient LBM via a time/space uniform immobile population post-collision, when the boundary rule cannot assure its equilibrium steady-state.[22,40] In this work, we prescribe $\mathscr{M}(\vec{r})$ exactly and compare the magnitude of M_0 for all flux schemes.

B. The corrective boundary flux

We introduce and comparatively evaluate an alternative approach, when the modified normal diffusive flux $D_n\pm\Phi_0$ is prescribed for two parallel surfaces $y'=\{0,h\}$, as

$$\begin{aligned}-\mathscr{D}\partial_{y'}P|_{y'=0} &= D_n+\Phi_0\,,\\ -\mathscr{D}\partial_{y'}P|_{y'=h} &= D_n-\Phi_0\,,\ \Phi_0=\mathscr{D}\chi.\end{aligned} \tag{32}$$

Equation (32) modifies the mass balance because the corrective flux is opposite on the two bounding surfaces; it mimics a uniform distribution of mass leakage over the wall. It is clear that Eq. (32) will behave most accurately for symmetrically placed walls. We will also extend Eq. (32) for the periodic interface, either continuous or subject to a constant flux jump, and compare magnitude Φ_0 for all flux schemes. The unknown value Φ_0 then replaces M_0 in the global list Var in Eq. (29):

$$Var = \Phi_0\cup_{\vec{r}\in V_p}(P(\vec{r})\cup\hat{\mathbf{n}}(\vec{r})),\quad M_0=0\,. \tag{33}$$

The rationale behind of the corrective flux is to verify whether Eq. (32) is more accurate than the M_0 source, because the modeled bulk equation remains not modified.

C. The steady-state MR and N-MR

The bulk system (26) is not defined for the cut links $q_b\in Q_b(\vec{r}_{\mathrm{b}})$ where Eq. (21) reduces to linear equation with respect to $X_q[8]$:

$$\begin{aligned}
M_q\cdot X_q - \mathscr{E}_{q_b}^{(-)}(\hat{\mathbf{n}}) &= -w_{q_b}(\vec{r}_{q_b})\,,\\
M_q[8] &= \{m_1,m_2,m_3,m_4\}\\
&\quad\cup\{m_5,m_6,m_7,m_8\}_q\,,\\
X_q[8] &= \{e_q^+,\mathrm{sgn}_{q_b}e_q^-,\hat{n}_q^+,\mathrm{sgn}_{q_b}\hat{n}_q^-\}|_{\vec{r}_{\mathrm{b}}}\\
&\quad\cup\{e_q^+,\mathrm{sgn}_{q_b}e_q^-,\hat{n}_q^+,\mathrm{sgn}_{q_b}\hat{n}_q^-\}|_{\vec{r}_{nb}}\,,\\
\vec{r}_{q_b} &= \vec{r}_{\mathrm{b}}+\delta_{q_b}\vec{c}_{q_b}\,,\ \vec{r}_{nb}=\vec{r}_{\mathrm{b}}-\vec{c}_{q_b}\,,\\
q &= \mathrm{sgn}_{q_b}q_b\,,\ q\in Q_{\frac{1}{2}}.
\end{aligned} \tag{34}$$

The coefficients $\{m_i\}$ are computed from MR in Eq. (A1):

$$\begin{aligned}
m_1 &= \hat{\alpha}+\beta+\hat{\beta}-1, & m_2 &= (\hat{\alpha}+\beta-\hat{\beta}+1),\\
m_3 &= -\tau^+m_1+\hat{\alpha}+\hat{\beta} & m_4 &= -\tau^-m_2+\hat{\alpha}-\hat{\beta}\\
&\quad+\hat{K}^+, & &\quad+\hat{K}^-,\\
m_5 &= \gamma+\hat{\gamma}, & m_6 &= \gamma-\hat{\gamma},\\
m_7 &= -\tau^+m_5+\hat{\gamma}, & m_8 &= -\tau^-m_6-\hat{\gamma}.
\end{aligned} \tag{35}$$

The local (linear) MR operates with zero coefficients m_5-m_8, so that M_q reduces to $M_q[4]=\{m_1,m_2,m_3,m_4\}_q$ and the unknown vector $X_q[4]|_{\vec{r}_{\mathrm{b}}}$ is local. The correction $\mathscr{E}_{q_b}^{(-)}$ applies with Eq. (21), where $\mathrm{CL}_{q\tau}(P,u_\tau P)$ is expressed with Eq. (17c) through *the in-node variables* $\hat{\mathbf{n}}=\cup_{q\in Q_{\frac{1}{2}}}\hat{n}_q^{\pm}(\vec{r}_{\mathrm{b}})$ (cf. Eqs. (B3)–(B4a)). Equations (34) and (35) complete the bulk system for $\cup_{\vec{r}_{\mathrm{b}}}Q_b(\vec{r}_{\mathrm{b}})$ wall-cut links. The steady-state algorithm then solves the global linear system with respect to all unknowns Var from Eq. (29) or Eq. (33).

D. The MR and N-MR interface-conjugate

Following[40,42,63] assume now that $P_k(\vec{r}_{int})$ and $D_n^{(k)}(\vec{r}_{int})$ are subject to continuity or jump conditions on the interface $\vec{r}_{int}$:

$$P^{(1)}|_{\vec{r}_{int}} = \sigma^{(p)}P^{(2)}+\eta^{(p)}|_{\vec{r}_{int}}, \tag{36a}$$

$$D_n^{(1)}|_{\vec{r}_{int}} = \sigma^{(u)}D_n^{(2)}+\eta^{(m)}|_{\vec{r}_{int}}. \tag{36b}$$

Based on Eq. (34), the interface-conjugate directional closure between the two neighbors $\vec{r}_i$ and $\vec{r}_{ni}=\vec{r}_i+\vec{c}_{q_i}$ is accordingly expressed by the Dirichlet $M_q^{(p)}(\alpha_q^{(p)})$ rule for Eq. (36a) and by the flux $M_q^{(f)}(W_q)$ rule for Eq. (36b):

$$\left.\frac{M_q^{(p)}\cdot X_q-\mathscr{E}_q^{(+)}}{\alpha_q^{(p)}}\right|_{\vec{r}_i}^{(1)} = \sigma^{(p)}\left[\frac{M_q^{(p)}\cdot X_q-\mathscr{E}_q^{(+)}}{\alpha_q^{(p)}}\right]\Bigg|_{\vec{r}_{ni}}^{(2)}+\eta^{(p)}(\vec{r}_{int})\,, \tag{37a}$$

$$\left.\frac{M_q^{(f)}\cdot X_q-\mathscr{E}_{q_i}^{(-)}(\hat{\mathbf{n}})}{w_q^{(u)}}\right|_{\vec{r}_i}^{(1)}=-\,\sigma^{(u)}\left.\left[\frac{M_q^{(f)}\cdot X_q-\mathscr{E}_{-q_i}^{(-)}(\hat{\mathbf{n}})}{W_q^{(u)}}\right]\right|_{\vec{r}_{ni}}^{(2)}+t_q\eta^{(m)}(\vec{r}_{int})\vec{1}_n\cdot\vec{c}_{q_i}. \tag{37b}$$

Equation (37) is expressed with Eqs. (34) and (35) in terms of the half set $\{e_q^+,\mathrm{sgn}_q e_q^-,\hat{n}_q^+,\mathrm{sgn}_q\hat{n}_q^-\}$ using the following convention in phases (1) and (2):

$$(1)\ :\ \vec{r}=\vec{r}_i,\quad \delta_q=\delta_{q_i},\quad \vec{r}_{int}=\vec{r}_i+\delta_{q_i}\vec{c}_{q_i},\quad \vec{r}_{nb}=\vec{r}_i-\vec{c}_{q_i},\quad q=q_i\mathrm{sgn}_{q_i},\quad \mathrm{sgn}_q=\mathrm{sgn}_{q_i}, \tag{38a}$$

$$(2)\ :\ \vec{r}=\vec{r}_{ni},\quad \delta_q=\delta_{-q_i},\quad \vec{r}_{int}=\vec{r}_{ni}+\delta_{-q_i}\vec{c}_{-q_i},\quad \vec{r}_{nb}=\vec{r}_{ni}-\vec{c}_{-q_i},\quad q=(-q_i)\mathrm{sgn}_{-q_i},\quad \mathrm{sgn}_q=\mathrm{sgn}_{-q_i}. \tag{38b}$$

Equation (37a) reads with an optional term $\mathscr{E}_q^{(+)}=I_{int}\alpha_q^{(p)}t_q^{(m)}c_e\Lambda^+\mathscr{M}_k(\vec{r}_{int})$ introduced to remove the interface value of the equilibrium mass-source term, or its second-order approximate, from the continuity/jump closure equation (see Ref. 40) We set $I_{int}=1$ and prescribe $\mathscr{M}_k(\vec{r}_{int})$ exactly on each interface side. In turn, Eq. (37b) reads with Eq. (21) applying the scale-factor of the MR flux scheme [cf. (7a), (23a) and (8a), (23b), respectively]:

$$\mathrm{FLI/FMR}\ :\ W_q^{(u)}=\alpha_q^{(u)}, \tag{39a}$$

$$\mathrm{DFLI}\ :\ W_q^{(u)}=\beta_q'. \tag{39b}$$

Equation (37) is assembled together with the bulk and boundary equations, the whole system is then solved with respect to all unknowns *Var* from Eq. (29) or Eq. (33).

Note: Below, the interface-conjugate is abbreviated as PP-FLI, PP-FMR or PP-DFLI when the PP applies for $M_q^{(p)}$ in Eq. (37a), whereas FLI, FMR or DFLI applies for $M_q^{(F)}$ in Eq. (37b). The FLI and FMR should be replaced by N-FLI and N-FMR when the presence of the advective flux projection in Eq. (37b) is not compatible with the prescribed condition (36b), examples in this respect are provided below.

E. Steady-state algorithms with the MR, N-MR, and A-LSOB

The steady-state TRT algorithm closed with the MR boundary and interface-conjugate conditions is formulated in more detail in Appendix B;[40] we update it with MR, N-MR or A-LSOB. To sum up, the global solution $\{P(\vec{r})\}$ and $\{\hat{n}_q^{\pm}(\vec{r})\}$ is found by solving the linear algebraic system composed from the following equations:

1. the couple of the TRT bulk equations (26), assembled for every bulk link;
2. the local mass-conservation equation (28), assembled for every fluid node;
3. the MR closure equation (34), assembled for every wall-cut link or, alternatively, the A-LSOB closure equations assembled in-node as provided below.
4. the couple of the MR interface-conjugate equations (36a) and (36b), assembled for every interface-cut link; they replace the couple of bulk equations.
5. a prescribed free value $P(\vec{r})$ in any one point when the global solution is defined to an additive constant, e.g., in the Neumann or periodic-interface systems. In such cases, M_0 from Eq. (28) enters the list of the global variables; otherwise $M_0=0$ is substituted there. Alternatively, the boundary flux can be prescribed with the corrective flux variable Φ_0 from Eq. (32); an extension for periodic interface is exemplified by Eq. (64).

Note: a posteriori, the normalized procedure shall remove the solution dependency on the prescribed value. We will examine the proposed flux schemes with respect to this property.

1. Steady-state N-MR boundary algorithm

The N-MR tangential correction $\mathrm{CL}_{q\tau}(P,u_\tau P)$ from Eq. (10) is embedded via $\mathscr{E}_{q_b}^{(-)}(\hat{\mathbf{n}})$ in Eq. (34), following Eq. (21). In that, $\mathrm{CL}_{q\tau}(P,u_\tau P)$ *is expressed* through $\mathbf{Y}[5]=\mathbf{B}^{-1}\mathbf{R}$, $R_q^{\pm}=\hat{n}_q^{\pm}-\hat{n}_q^{\pm(2)}|_{\mathbf{Y}=0}$, and $\{\hat{n}_q^{\pm}\}$ belongs to the list of unknowns *Var*. In that, one computes $\mathbf{B}^{-1}$ and $\hat{n}_q^{\pm(2)}|_{\mathbf{Y}=0}$ following the *Reconstruction step* from the transient algorithm in Sec. II E.

2. Steady-state N-MR interface-conjugate algorithm

The interface-conjugate applies with Eq. (37) where, similarly, the tangential corrections are introduced by the terms of $\mathscr{E}_{q_i}^{(-)}$ and $\mathscr{E}_{-q_i}^{(-)}$ in Eq. (37b). They are expressed, respectively, through $\mathbf{Y}[5]_{\vec{r}_i}=\mathbf{B}^{-1}\mathbf{R}|_{\vec{r}_i}^{(1)}$ and $\mathbf{Y}[5]_{\vec{r}_{ni}}=\mathbf{B}^{-1}\mathbf{R}|_{\vec{r}_{ni}}^{(2)}$ in two interface nodes.

3. Steady-state A-LSOB boundary algorithm

Similarly with the N-MR, the normal derivatives in the Taylor conditions from Eq. (12) are expressed through $\mathbf{Y}(\hat{\mathbf{n}}(\vec{r}_\mathrm{b}))$ and the prescribed Taylor condition is embedded into the global system. Then, giving N_b cut links $\{q_b\}$, one adds to the global system N_b-1 closure "expansions" in the form

$$\hat{n}_q^+=\hat{n}_q^{+(2)}\,,\ \hat{n}_q^-=\hat{n}_q^{-(2)}\,,\ q=\mathrm{sgn}_{q_b}q_b\,, \tag{40}$$

where $\hat{n}_q^{\pm}(\vec{r}_\mathrm{b})$ belongs to *Var*, and $\hat{n}^{\pm(2)}(\vec{r}_\mathrm{b})$ is prescribed as given by Eq. (16) in terms of $\mathbf{Y}(\hat{\mathbf{n}}(\vec{r}_\mathrm{b}))$.

Note: The choice of N_b-1 Eq. (40) is not defined uniquely: one can prescribe N_b-1 relations for the symmetric or anti-symmetric components alone, as $\hat{n}_q^+=\hat{n}_q^{+(2)}$ or $\hat{n}_q^-=\hat{n}_q^{-(2)}$, or combine these two. In principle, any combination of the reconstruction subset with N_b-1 closure relations is suitable provided that, respectively, Eq. (17) and the global linear system are well defined. Our optional semi-heuristic algorithm is detailed by Example 4 in Sec. B.

4. Steady-state A-LSOB interface-conjugate algorithm

This algorithm is only applied in Sec. VI A 3 for a straight interface in interface-perpendicular plug flow. The couple of the interface conditions (36a) and (36b) is then expressed through their normal Taylor approximate with Eqs. (12a) and (12b), and it replaces the couple of the bulk equations for interface-cut link.

F. Summary on the steady-state formulation

The steady-state TRT formulation operates with the non-equilibrium post-collision variables $\hat{n}_q^{\pm}(\vec{r})$ and the conserved quantity

$P(\vec{r})$. They solve the linear algebraic bulk system composed of Eqs. (26)–(28). In a continuous problem, the solvability condition of the Neumann problem is guaranteed by the global mass conservation condition; however, since the continuous condition may not be assured in the discrete system, we propose to adjust it either with a single variable M_0 from Eq. (28), in any geometry, or with the corrective boundary flux $\pm\Phi_0$ from Eq. (32), in specific channel-like slabs. These variables are automatically obtained by solving the global Neumann or interface-closed system, where solution $P(\vec{r})$ is defined to an additive constant. Our next experiments will compare the respective accuracy of the two solvability techniques, whereas $|M_0|$ and $|\Phi_0|$ will measure the mass imbalance of the proposed flux schemes.

The key point is that the MR, N-MR, and A-LSOB are very similar to their transient formulation, but these algorithms are directly expressed in terms of the steady-state local *variables*, $\{\hat{n}_q^{\pm}\}$ and P. The bulk linear system is then closed by the compact MR closure equations (34), and it may incorporate the compact MR interface-conjugate (37). Equations (34) and (37) are optionally amended with the corrections for mass-source variation and tangential-flux release; the N-MR is specified with the FLI, FMR, and DFLI. Alternatively, the bulk system can be closed by the A-LSOB closure equations; they prescribe the normal Taylor equation (12) and $\hat{n}_q^{\pm} = \hat{n}_q^{\pm(2)}$ for the incoming links with Eq. (40); these equations are all termed in in-node variables through the reconstruction. The algorithms are all formulated in Sec. III E; they are built within the symbolic software and solved with its numerical solver.

IV. ROTATED PARABOLIC SOLUTIONS WITH THE TANGENTIAL ADVECTION

We introduce the stratified Darcy system and outline its previous analysis in Sec. IV A. Section IV B demonstrates that (i) the N-MR makes the two advective-flux schemes FLI and FMR exact for any interface diffusive-flux jumps in the presence of the grid-rotated Darcy velocity, and that (ii) the A-LSOB Dirichlet scheme T-PP and the diffusive-flux T-DFLI support this problem exactly. We then intentionally degrade the parabolic Dirichlet and Neumann accuracy to the linear one following the existing (similar in spirit) approaches[42,62,104,105] and demonstrate their respective solutions in Sec. IV C. Section IV D discusses obtained results and outlines the similarity/distinctness with their rotated Poiseuille flow counterpart. The Dirichlet and Neumann schemes are, respectively, classified in Tables I and II according to the presented analysis.

A. Stratified Darcy layers

We consider a stratified two-layered rotated system of width $h = h_1 + h_2$: $\phi = \phi_1$ when $y' \in [-h_1, 0]$ and $\phi = \phi_2$ when $y' \in [0, h_2]$. The system is aligned with the axis $x' = \vec{1}_\tau \cdot (x, y)$, and the diffusion process develops along the normal axis $y' = \vec{1}_n \cdot (x, y)$ [cf. Eq. (18c)]; the two layers are either periodic or bounded by two parallel walls. The interface-parallel (Darcy) velocity $\vec{u} = u_\tau \vec{1}_{x'}$ is constant; the mass-source $\mathscr{M}_k(\vec{u})$ is set piece-wise constant and hence, the profile $P(y')$ is piece-wise parabolic:

$$\partial_{x'} u_\tau P_k(y') - \mathscr{M}_k(y') = \mathscr{D}_k \partial^2_{y'} P_k(y'),\ \mathscr{D}_k := \phi_k \mathscr{D}_0 = c_e \Lambda_k^-,\quad \mathscr{M}_k(y') := \mathscr{U}\phi_k - u_\tau, \tag{41a}$$

$$P_k(y') = a_k + b_k y' + c_k y'^2, \quad c_k = \frac{-\mathscr{M}_k}{2\Lambda_k^- c_e}. \tag{41b}$$

The constants $\{a_k, b_k\}$ are set by Eq. (36) provided that the solvability condition is satisfied. The periodic continuous condition with $\sigma^{(u)} = 1$, $\eta^{(m)} = 0$ in Eq. (36b) is satisfied when $\mathscr{U} = \mathscr{U}^{(ex)}$ in Eq. (41a), thanks to the global mass conservation:

$$\langle \mathscr{M} \rangle = 0 \text{ with } \mathscr{U}^{(ex)} := \frac{\langle u_\tau \rangle}{\langle \phi \rangle} = \frac{u_\tau h}{\phi_1 h_1 + \phi_2 h_2}. \tag{42}$$

Equations (41) and (42) with the $y'-$ periodic, continuous solution $P(y')$ and continuous diffusive flux $-\mathscr{D}_k \partial_{y'} P(y')$ match the EMM boundary problem[37,94] for the (rotation-invariant) Taylor dispersion coefficient $D_T = -\frac{\langle Pu \rangle}{\langle \phi \rangle}$, which is due to the structure heterogeneity alone in the stratified Darcy layers. The TRT-EMM numerical solution for D_T has been examined with the implicit interface tracking in the straight system,[38] where the exact piecewise parabolic profile is available thanks to $\Lambda = \frac{1}{8(1-c_e)}$, because this choice[25,36] locates midway the ABB implicit surface [it corresponds to $I_b = 1$ in Eq. (A4) and $I_{int} = 0$ in Eq. (37a); otherwise, $\Lambda = \frac{1}{8}$ with $I_b = 0$ in Eq. (A4) and $I_{int} = 1$ in Eq. (37a), as in Table I]. The stratified Darcy modeling has been also extended[38] for the cubic and quartic polynomial solution due to the recursive polynomial mass-source expansion; these solutions provide, respectively, the skewness and kurtosis. Further extension[39] to the diagonally-rotated d2q9 system with the *implicit interface tracking* revealed that the non-equilibrium B-layer accommodation and the truncation parabolic component $t_q \partial_q^2 P u_\tau c_{q\tau}^3$ produce a non-zero *local gradient estimate in the translation invariant solution*, as $c_e \partial_\tau P \approx \sum_{q=1}^{Q-1} \hat{n}_q^- c_{q\tau}$. Moreover, the equilibrium A-layer accommodation perturbs the predicted Pe^2—scale of the modeled dispersion coefficient and retards its convergence from the second to first order, unless with the d2q5 in the diagonal stratified system. We examine now the interface-conjugate treatment in the rotated channels by extending the MR simulations[40] to N-MR and A-LSOB.

B. Piece-wise parabolic solutions with MR, N-MR, and A-LSOB

We formally extend the EMM problem for suitable combinations of the interface jumps and boundary conditions. Equation (42) presents the solvability condition for the y'—periodic but also constant-flux bounded system; in these two problems, $P(y')$ is defined up to an additive constant. Equation (36) with the continuous and jump conditions has been addressed[40] with the help of the interface-conjugate from Eq. (37), but without the tangential-flux correction $\mathscr{E}_{q_i}^{(-)}$ in Eq. (37b). In theory, the solution in Eq. (41b) is expected to be the same with and without tangential velocity field when $\mathscr{M}_k$ is fixed with Eq. (41a). However, the numerical computations in pure-diffusion [$e_q^- \equiv 0$], and in the presence of the advective velocity [$e_q^- = t_q^{(a)} u_\tau \vec{1}_\tau \cdot \vec{c}_q$], may produce different results because of the closure relations. That is because their non-equilibrium solutions differ, e.g., on the exact *advection-diffusion* solution $\hat{n}_q^{\pm}$ reads

$$\hat{n}_q^+ = t_q^{(a)} c_{qn} c_{q\tau} u_\tau \partial_n P - t_q^{(m)} c_{qn}^2 c_e \Lambda_k^- \partial^2_{nn} P, \tag{43a}$$

$$\hat{n}_q^- = t_q^{(m)} c_{qn} c_e \partial_n P - t_q^{(a)} c_{qn}^2 c_{q\tau} \Lambda_k^+ u_\tau \partial^2_{nn} P, \tag{43b}$$

with

$$\partial_n P = b_k + 2c_k y', \quad \partial^2_{nn} P = 2c_k\,, \qquad \partial_\tau P = \partial^2_{\tau\tau} P = \partial^2_{\tau n} P = 0. \tag{43c}$$

Since $\mathscr{M}_k$ is piece-wise constant, the mass-source corrections vanish in Eqs. (24a) and (24b). The tangential-flux correction $\mathrm{CL}_{q\tau}$ in Eq. (10) implicitly reduces to its *advective flux* counterpart on the exact profile:

$$\mathrm{CL}_{q\tau}(y') = \alpha^{(u)} t_q^{(a)} u_\tau P(y') c_{q\tau} + \beta^{(u)} t_q^{(a)} u_\tau \partial_n P(y') c_{q\tau} c_{qn} + \gamma^{(u)} t_q^{(a)} u_\tau \partial^2_{nn} P(y') c_{q\tau} c^2_{qn}. \tag{44}$$

Hence, although in theory the advective-diffusive flux and diffusive flux continuity conditions are equivalent, this is not the case with the MR flux schemes, because the tangential advection term is projected onto the interface-cut links with Eq. (44). In other words, Eq. (44) is expected to spoil the linear diffusive flux, unless when $\alpha^{(u)} = \beta^{(u)} = \gamma^{(u)} = 0$, as for example, in DFLI from Tables XVI–XVIII. Indeed, it has been confirmed[40] that PP-DFLI is exact in Eq. (36) for any scalar and flux grid-rotated conditions [recall, the Dirichlet family PP assures the continuity or jump in Eq. (36a) on the parabolic profiles]. In pure-diffusion and grid-aligned slabs, the PPLI-FMR, PP-FMR and PPLI-FLI, PP-FLI are also exact. However, among these schemes, only PP-FMR is exact in grid-inclined advection restricted to the "proportional" jump, as $\sigma^{(p)} = \sigma^{(u)}$, $\eta^{(p)} = 0$, when Eq. (44) vanishes from the interface-conjugate condition due to Eq. (37a), including the continuous case $\sigma^{(p)} = \sigma^{(u)} = 1$. At the same time, the FLI closure in Eq. (5) is built with $\beta^{(u)} = \alpha^{(u)}\delta$, like FMR, but with $\gamma^{(u)} = \alpha^{(u)}\Lambda$, instead of $\gamma^{(u)} = \frac{1}{2}\alpha^{(u)}\delta^2$ (see Table XVII). Consequently, FLI cannot assure an exact continuation of the (last) parabolic advection term in Eq. (44); however, PP-FLI remains second-order accurate in the rotated slabs (see Figs. 5–7 in Ref. 40). By construction, N-FLI aims to vanish Eq. (44) from the closure relation, and then it is expected to become exact on the piece-wise parabolic rotated solutions for (i) a constant flux Neumann boundary and (ii) for any interface-conjugate with Eq. (36).

In detail, the grid-inclined streamwise-periodic channel is discretized hereafter following,[40] such that the boundary/interface bisects a prescribed point (x_0, y_0) on the bottom. The L_2-error metric E_2 is employed hereafter to estimate the relative root squared error to exact solution; E_2 is computed over all grid points. We apply the generic procedure and reconstruct $\mathbf{Y}[5]$ in Eq. (10) with Eqs. (17) and (18). Equation (19) or Eq. (B2) [with non-zero determinant] then exactly reproduce all derivatives in Eq. (43c). This exact solution is also matched with the rectangular subsets, as $\mathbf{B}[6\times 5]$ or $\mathbf{B}[8\times 5]$ from Eq. (20). When $\mathbf{Y}[5]$ is expressed through the local unknowns, N-FLI and N-FMR apply with Eq. (21) for the boundary flux and Eq. (37b) for the interface flux.

Figure 3 addresses the computations in the bounded inclined channel $\theta = \arctan[\frac{1}{2}] \approx \frac{\pi}{6.776}$ closed by the constant diffusive flux and the continuous interface (left diagram), or Dirichlet boundary and interface jumps from Eq. (36) (right diagram). The PP scheme reproduces the interface scalar continuity condition from Eq. (36a). The boundary and interface flux-conditions are first modeled with the three MR schemes, FLI, FMR and DFLI. In agreement with our predictions, FLI and FMR produce very large errors, but DFLI is exact. In fact, the FMR is exact here for *the continuous interface advective-diffusive flux* but it cannot prescribe correctly the rotated diffusive boundary flux alone. Next, on the left diagram of Fig. 3, we replace the FMR by N-FMR for the boundary flux, and the obtained solution then becomes exact, in agreement with our expectations. Accordingly, $P(y')$ becomes exact when N-FLI replaces FLI both on the boundary and the interface (left diagram). Finally, the combinations of the exact schemes, as the single-node A-LSOB T-DFLI on the boundary, with the DFLI, N-FLI or N-FMR on the interface, all reproduce the exact profile. In turn, the single-node T-PP operates exactly the Dirichlet boundary (right diagram), where FLI and FMR are not able to reproduce the diffusive-flux interface jump because of their advection components. In contrast, DFLI, N-FLI and N-FMR are exact.

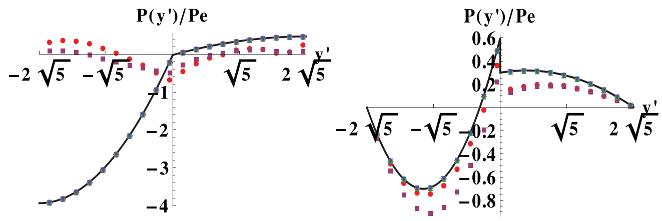

FIG. 3. The effect of the tangential velocity projection is demonstrated for piece-wise parabolic rotated solutions subject to Eq. (36) in a small rotated system at high $\mathrm{Pe} = 10^3$. Left: Interface continuity condition is exact with the parabolic MR PP family; zero boundary flux and interface-flux are, respectively, modeled with FLI − FLI● $E_2 = 1.06$, FMR-FMR■ $E_2 = 0.98$; $E_2 \equiv 0$ in all other schemes: DFLI-DFLI◆, N-FMR$_r$-FMR▲, N-FLI$_r$-N-FLI$_r$▼, T-DFLI-N-FLI$_r$○. Data: $\partial_{y'} P(-h_1) = \partial_{y'} P(h_1) = 0$, $\sigma^{(p)} = \sigma^{(u)} = 1$, $\eta^{(p)} = \eta^{(m)} = 0$. Right: Dirichlet boundary is exact with the parabolic A-LSOBT-PP, the interface flux is modeled with FLI● $E_2 = 2.13\times 10^{-1}$, FMR■ $E_2 = 4.33 \times 10^{-1}$; $E_2 \equiv 0$ in all other schemes: DFLI◆, N-FLI$_r$▲, N-FMR$_r$▼. Data: $P(-h_1) = 1$, $P(h_1) = 2$, $\sigma^{(p)} = 2$, $\eta^{(p)} = 0.2$, $\sigma^{(u)} = 4$, $\eta^{(m)} = 0.4$. Two diagrams: $\theta = \arctan[\frac{1}{2}]$, $h = H\cos[\theta]$, $H = 10$, $(x_0, y_0) = (\frac{1}{4}, 0)$, $\mathrm{Pe} = 10^3$, $\mathscr{U} = 1$, $c_e = \frac{1}{30}$.

C. Inexact solutions with the linear schemes

We model a very sharp variation (of three orders of magnitude) at high Péclet number $\mathrm{Pe} = 10^3$ in a small inclined channel $h = 10\cos[\theta]$, as displayed in Fig. 3, but replace the parabolic Dirichlet and linear flux schemes by the linear Dirichlet boundary and interface continuity conditions, and constant-flux schemes. We consider first the linear LMKC scheme;[42,62] the LMKC is the member of the infinite MPLI family from Table X and they share the same steady-state solution. These schemes are parametrized but their accuracy degrades in the presence of the advection velocity, because the advection $\hat{n}_q^+$ term $\beta^{(u)} t_q \partial_q P u c^2_{q\tau}$ is non-zero in Eq. (5) in the inclined channels. Consequently, the E_2 grows almost linearly with Pe but still converges with second-order rate (see Figs. 5–8 in Ref. 40 for the MPLI-FLI interface conjugate in continuous straight/diagonal/rotated systems).

Figure 4 (left diagram) follows Fig. 3 but LMKC replaces PP for the continuity condition in the interface-conjugate. Recall that only the FLI-FLI and the FMR-FMR (boundary-interface) treatment is inexact in Fig. 3 (left diagram). Now, also the four others, exact flux combinations, display highly inaccurate solutions, N-FLI$_r$-N-FLI$_r$ shows the smallest but still unacceptable error. Remarkably that FLI-

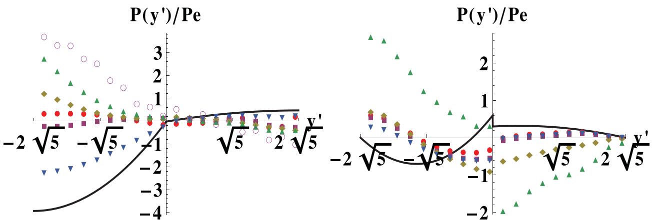

FIG. 4. Following Fig. 3 but with the only linear Dirichlet scheme[62] LMKC from Table X. Left: LMKC replaces the parabolic MR − PP for interface-continuity condition; zero boundary and interface-fluxes are modeled with FLI − FLI●, FMR − FMR■, DFLI − DFLI ◆, N-FMR$_r$ − FMR▲, N-FLI$_r$ − N-FLI$_r$▼, T-DFLI − FMR ◯; $E_2 = \{1.09, 9.8 \times 10^{-1}, 1.2, 1.47, 4.4 \times 10^{-1}, 1.85\}$, accordingly; for visualization purpose, T-DFLI − N-FLI$_r$ [$E_2 = 5.58$] is replaced by T-DFLI − FMR [$E_2 = 1.13$]. Right: LMKC replaces A-LSOB T-PP on the Dirichlet boundary; on the interface, scalar-jump is assured by MR PP and flux-jump is modeled with FLI●, FMR■, DFLI◆, N-FLI$_r$▲, N-FMR$_r$▼; $E_2 = \{1.27, 1.3, 1.85, 4.42, 1.13\}$. The three last results become exact [the two diagrams] with the parabolic PP and T-PP in Fig. 3.

FLI and FMR-FMR are almost unaffected by this intentional interface discontinuity; we will show later that their mass-balance properties (and then accuracy) are independent of the scalar-continuity scheme in basic configurations. Figure 5 (right diagram) demonstrates that LMKC also completely destroys the expected Dirichlet boundary location, here $\mathrm{Pe}^{-1}P(y') \approx 0$, when it replaces the parabolic A-LSOB T-PP scheme (12a).

Figure 5 displays the results of the linearly-truncated normal Taylor conditions, when T-DFLI from Eq. (12b) (left diagram) and T-PP from Eq. (12a) (right diagram) become depleted from their parabolic terms. The T-DFLI then degrades from the linear to the constant-flux condition, and it spoils all exact parabolic solutions. In turn, the degraded T-PP cannot support the exact solutions but its boundary location is much more accurate than with the LMKC in Fig. 4 (right diagram). This confirms that the principal MPLI/LMKC deficiency at high $\mathrm{Pe} = 10^3$ is due to the linear advection correction $\beta^{(u)} t_q \partial_q P u c^2_{q\tau}$, which is absent in the degraded normal Taylor T-PP in Fig. 5 (right diagram).

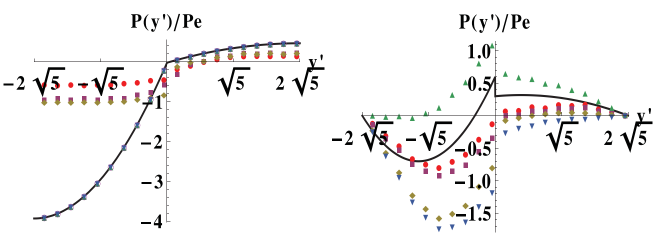

FIG. 5. Following Fig. 3 but with the only linear normal Taylor approximations of the boundary flux (left) and Dirichlet condition (right). Left: T-DFLI models zero boundary flux without parabolic term in Eq. (12b); interface continuity conditions are modeled by combining MR PP and N-FLI$_r$●$E_2 = 6.9 \times 10^{-1}$ FMR■ $E_2 = 7.15 \times 10^{-1}$, DFLI◆$E_2 = 8.21 \times 10^{-1}$. These solutions are all exact with T-DFLI from Eq. (12b): $E_2 = 0$ using T-DFLI − N-FLI$_r$▲, T-DFLI − FMR ▼, T-DFLI − DFLI◯. Right: the T-PP operates the Dirichlet boundary without last term in Eq. (12a); the scalar-jump is assured by MR PP and the flux-jump by FLI●, FMR■, DFLI◆, N-FLI$_r$▲, N-FMR$_r$▼, $E_2 = \{2.13 \times 10^{-1}, 8.141 \times 10^{-1}, 1.609, 1.222, 2.015\}$, accordingly. The three last results become exact with the parabolic T-PP in Fig. 3 (right diagram).

D. Summary on the piece-wise parabolic solutions

The piece-wise parabolic solution allows us to validate exactly the N-FLI and N-FMR in the presence of constant Darcy velocity field of an arbitrary amplitude. Since the obtained profiles $P(y')$ are exact, only $\partial_n P(\vec{r}_b)$ and $\partial^2_{nn} P(\vec{r}_b)$ are non-zero on the obtained solution $\mathbf{Y}(\hat{n}^{\pm}_q)$, giving an efficient reconstruction test-case. In turn, d2q5 is also able to produce the exact rotated channel solution with $\mathbf{B}[4 \times 4]$ provided that $\partial^2_{\tau\tau} P = 0$ or $\partial^2_{\tau n} P = 0$ is substituted into Eq. (18). Moreover, giving zero tangential and mixed solution derivatives, the d2q5 is able to derive $\mathbf{Y}[2] = \{\partial_n P, \partial^2_{nn} P\}$ from $\{\hat{n}^+_q, \hat{n}^-_q\}$ assigned on the same link $c_{qn} \neq 0$. Altogether, we confirm that DFLI, N-FLI and N-FMR are exact for the boundary and interface piece-wise linear rotated diffusion-flux in the presence of a uniform grid-inclined tangential advection velocity and jumps, provided that the interface scalar condition is modeled exactly with the MR PP. We also validate the exactness of the one-node Taylor boundary schemes from Eq. (12), T-PP and T-DFLI. In principle, Eq. (12) might be applied exactly on the interface in the rotated channel solutions due to their translation invariance.

Except the parabolic MR and A-LSOB T-PP, the existing Dirichlet ADE schemes are commonly restricted to only leading-order accuracy in the grid-inclined velocity field. Although PPLI is exact in the rotated pure-diffusion slab and the grid-aligned velocity field, it shares the MPLI/LMKC deficiency in the grid-rotated advection velocity field, because their closure relation in Eq. (5) reads with $\beta^{(u)} \neq 0$ and $\gamma^{(u)} \neq 0$ in Table XIV. Methodologically, the degraded T-I-PP$_r$ extends the Dirichlet flat-wall scheme[104,105] from the in-node placement $\delta \equiv 0$ to an inclined flat wall; obviously, when $\delta \equiv 0$, the linear and parabolic terms vanish in the normal Taylor expansion (12), but $\delta \equiv 0$ cannot address the grid-inclined walls. The degraded T-I-PP$_r$ fits then only the first-order accurate normal Taylor relation but it locates much more accurately the boundary values thanks to the absence of the velocity projections in its wall-normal Dirichlet Taylor prescription.

Let us mention that the force-driven Poiseuille flow modeling follows the same path: whereas a rotated parabolic no-slip and slip solutions are available for any two-point multi-reflection[22,30,40,85] and single-node LSOB,[21,87] they cannot be matched by the moment-based on-grid boundary methods[57,77] with $\delta \equiv 0$. The recent LI scheme[95] purposes the exact inclined Poiseuille flow modeling but, in reality, its solution is exact only in a straight channel, extending the BB solution[20,22] and MGLI schemes[30,40] to any distance δ and to any (stable) Λ. Yet, this Poiseuille channel problem is a pure-diffusion counterpart of the ADE problem (41). To this end, we complement PPLI with its flow counterpart IPLI in Table XII; the IPLI is exact for the force-driven Poiseuille flow in a grid-inclined channel and it is parabolic-accurate for any uniform-density Stokes flow, at least. We emphasize that the IPLI prescribes the forcing term $t_q \Lambda^- \vec{F} \cdot \vec{c}_q$ in both bulk and boundary equilibrium e^-_q following;[40] otherwise, when expressing[20,22,95] the force term from the momentum equation, IPLI becomes anisotropic, i.e., cut-link direction dependent. The PPLI/IPLI derivation straightforwardly applies Eq. (5), a result that will be reported elsewhere.

Finally, concerning the Neumann condition, the Cartesian decomposition method[42,62] assumes that the linear interpolations along two grid axes produce the "same" Dirichlet value; we have shown that they fail on the parabolic profiles and, especially, in the inclined velocity field. Hence, although the original FLI scheme[62] is able to support the rotated parabolic diffusion profile, the Cartesian decomposition method is not expected to extend this property to a constant rotated velocity. Purposely, we also degraded the A-LSOB flux scheme T-DFLI following[104,105] and rendered it only suitable for a constant normal-flux; obviously, this scheme cannot then support a linear diffusive flux on the parabolic profiles and it produces the relaxation-dependent, wrong solutions.

To sum up, the parabolic, N-FLI and T-DFLI and two-point N-FMR are expected to enhance the similarly constructed, but lower-order Neumann schemes. The single-node Dirichlet PPLI extends MPLI/PLI to rotated diffusion slabs and grid-aligned tangential velocity. These schemes do not restrict the free parameter range.

V. Rotated quartic solution with the tangential advection

We extend the stratified rotated system to the presence of the parabolic velocity-field and mass-source. In this context, Sec. V A describes the model equation and its analytical solution; Sec. V B constructs the effective rotated TRT bulk solution and determines the free-parameter range when it is either exact or obeys the exact solvability condition. Section V C extends the reconstruction procedure for a space-variable velocity and mass-source; Sec. V D validates the bulk analysis with the exact closure relations; Sec. V E constructs the effective "straight" solutions with a corrective boundary flux. Sections V F and V G discuss grid-aligned and rotated numerical solutions. Section V H examines independence over an additive constant. Section V I addresses the two-layered, bounded and periodic, systems. Section V J draws the conclusions.

A. The rotated Taylor-dispersion problem

We consider again Eq. (41a) but in open flow, where porosity ϕ is set equal to 1, and the interface-parallel constant Darcy velocity u_τ is replaced by the parabolic profile:

$$u_\tau(y') = -\frac{1}{2}\Psi y'(y'-h)\,,\; y' \in [0,h]\,,$$
$$\mathscr{M}(\mathscr{U}, y') = \mathscr{U} - u_\tau(y'), \quad \langle \mathscr{M}(\mathscr{U}^{(ex)}, y')\rangle = 0\,, \tag{45}$$
$$\mathscr{U}^{(ex)} = h^{-1}\int_0^h u_\tau(y') = \frac{\Psi h^2}{12}.$$

Exact solution $P^{(ex)}(y')$ is given by the rotation-invariant quartic polynomial:

$$P^{(ex)}(y') = \sum_{m=0}^{4} p_m^{(ex)} y'^m\,,$$
$$p_2^{(ex)} = -\frac{\Psi h^2}{24\mathscr{D}}, \quad p_3^{(ex)} = \frac{\Psi h}{12\mathscr{D}}, \quad p_4^{(ex)} = -\frac{\Psi}{24\mathscr{D}}. \tag{46}$$

Let us first prescribe the impermeable boundary, where $p_1^{(ex)} = 0$ and the dimensionless symmetric profile is defined to an additive constant P_0:

$$(\mathrm{Pe}\,h)^{-1}P^{(ex)}(Y) = -\frac{1}{2}Y^2(Y-1)^2 + P_0\,,\; Y = \frac{y'}{h}\,,$$
$$\mathrm{Pe} = \frac{\mathscr{U}h}{\mathscr{D}} = \frac{\Psi h^3}{12\mathscr{D}}, \quad P_0 = (\mathrm{Pe}\,h)^{-1}p_0. \tag{47}$$

This solution is illustrated in Fig. 7 (left diagram) using the normalization condition $\langle P^{(ex)}(y')\rangle = 0$ $[P_0 = \frac{1}{60}]$.

Physically, *a posteriori* estimate $D_T = -\frac{\langle Pu(y')\rangle}{h}$ predicts the famous Taylor dispersion coefficient.[1,92] The EMM extends this solution to the skewness and kurtosis, both in the spatial and temporal system of moments, interconnected by simple algebraic formulas (see Table III in Ref. 37 for an open channel and a circular capillary); these solutions are also extended[37,94] to heterogeneous stratified open/porous systems. On the numerical panel, this benchmark is exciting because it allows (i) to quantify[35] quasi-exactly the truncation (numerical) dispersion, skewness and kurtosis, by extending the EMM to the fourth-order approximate of the modeled macroscopic equation; (ii) to estimate the D_T deviations induced by the tangential velocity constraint;[36] and (iii) to examine the convergence delay due to the weighted accommodation on the diagonal interface. However, although the particular optimal Λ solutions have been derived to minimize these numerical artifacts, the effective advection-diffusion bulk solution of the scheme has not yet been constructed in arbitrary rotated channels.

In theory, when $\mathscr{M}(y')$ is prescribed with Eq. (45), $P^{(ex)}(y')$ is the same in pure diffusion and in the presence of the tangential advection velocity $\vec{u}(y') = u_\tau(y')\vec{1}_\tau$. However, the discrete solvability condition and the effective solution will differ giving $e_q^- \equiv 0$ or $e_q^-(y') = t_q^{(a)}u_\tau(y')P(y')c_{q\tau}$ in Eq. (14b). Besides, we have shown that the boundary schemes are subject to a different accuracy in these two cases. We examine whether the truncation and accommodation may perturb the linear Pe-scale of the scalar field $P(y')$, and whether the tangential corrections may smooth this joint discrete effect.

B. Effective discrete solution

We first examine (i) whether the quartic polynomial solution satisfies the discrete rotated advection-diffusion system and (ii), delineate free parameters when the effective solution is exact.

We give the parabolic profile for velocity and mass-source: $u_\tau(y') = \sum_{m=0}^{2} u_m y'^m$ and $\mathscr{M}(y') = \sum_{m=0}^{2} \mu_m y'^m$, and look for the quartic and quintic, respectively, effective solutions $P^{(eff)}(y')$ and $\hat{n}_q^{+(eff)}(y')$ [$\hat{n}_q^{+(eff)}$ is searched for as the fifth-order polynomial because $\hat{n}_q^+ = \nabla_q e_q^- + \cdots$ in Eq. (15a) and $e_q^-(y') = t_q^{(a)}u_\tau(y')P(y')c_{q\tau}$ is sextic]:

$$P^{(eff)}(y') = \sum_{m=0}^{4} p_m^{(eff)} y'^m, \tag{48a}$$

$$\hat{n}_q^{+(eff)} = \sum_{m=0}^{5} n_{q,m}^{(eff)} y'^m. \tag{48b}$$

Hence, we look for the effective solution $\hat{n}_q^{+(eff)}$ to Eq. (15a), keeping in mind that all solution components only vary along $\vec{1}_{y'} = \vec{1}_n$, then

$$\Delta_q\psi(\vec{r}) = \frac{1}{2}(\psi(\vec{r}+c_{q,y'}) - \psi(\vec{r}-c_{q,y'}))\,,$$
$$\Delta_q^2\psi(\vec{r}) = \psi(\vec{r}+c_{q,y'}) - 2\psi(\vec{r}) + \psi(\vec{r}+c_{q,y'})\,, \tag{49}$$
$$\forall\,\psi\,,\text{ with } c_{q,y'} = \vec{c}_q \cdot \vec{1}_{y'}.$$

Following the solution procedure,[39] we then plug Eq. (48) into Eq. (15a), and express the coefficients $\{n_{q,m}^{(eff)}\}$ through $\{p_m^{(eff)}\}$ for four d2q9 velocity links. The four components $\hat{n}_q^{+(eff)}(p_m^{(eff)})$ are then summed in Eq. (28), giving there $M_0 = 0$. The solvability condition comes down to the third-order polynomial equation, say $\sum_{m=0}^{3} e_m y'^m = 0$, where the three unknowns $\{p_2, p_3, p_4\}^{(eff)}$ can be determined only provided that $e_3 = 0$, as

$$
\begin{aligned}
e_3 &= u_2 p_4^{(eff)}(12\Lambda - 1)(3t_c^{(a)} - 1)\sin[4\theta]\,,\\
e_3 &= 0 \text{ if } u_2 = 0\,, \text{ or}\\
\sin[4\theta] &= 0\,, \text{ or } \Lambda = \frac{1}{12}\,, \text{ or } t_c^{(a)} = \frac{1}{3}.
\end{aligned}
\tag{50a}
$$

The case $u_2' = 0$ [$\Psi = 0$ in Eq. (45)] corresponds to pure diffusion with a given parabolic mass source, where the quartic polynomial solution exists for any rotation. The case $\sin[4\theta] = 0$ covers the grid-aligned, straight/diagonal, orientation where the effective quartic solution exists for any Λ and advection-weight $\{t_q^{(a)}\}$. The case $\Lambda = \frac{1}{12}$ vanishes the third-order truncation spatial error (see[34] and reference therein). The case $\{t_c^{(a)} = \frac{1}{3}, t_d^{(a)} = \frac{1}{12}\}$ corresponds to the isotropic (hydrodynamic) d2q9 weight obeying the additional constraint $\sum_{q=1}^{Qm} t_q^{(a)} c_{qx}^2 c_{qy}^2 = \frac{1}{3}$. We prescribe $t_c^{(a)} = t_c^{(m)} = \frac{1}{3}$ and keep Λ free. The *effective* solution (48a) is then given as

$$
\begin{aligned}
p_2^{(eff)} &= p_2^{(ex)} + \delta p_2, \quad p_2^{(ex)} = -\frac{\mu_0'}{2},\\
\delta p_2 &= \mu_2'\psi(\Lambda, c_e) + \frac{\xi(\Lambda)\sin[4\theta]}{864}(6(\mu_2' u_1' + 2\mu_1' u_2')\\
&\quad - \mu_2' u_2'^2 \xi(\Lambda)\sin[4\theta]),
\end{aligned}
\tag{51a}
$$

$$
\begin{aligned}
p_3^{(eff)} &= p_3^{(ex)} + \delta p_3, \; p_3^{(ex)} = -\frac{\mu_1'}{6},\\
\delta p_3 &= \frac{\mu_2' u_2' \xi(\Lambda)\sin[4\theta]}{72},
\end{aligned}
\tag{51b}
$$

$$
\begin{aligned}
p_4^{(eff)} &= p_4^{(ex)} = -\frac{\mu_2'}{12}, \text{ with}\\
u_m' &= \frac{u_m}{\mathscr{D}}, \quad \mu_m' = \frac{\mu_m}{\mathscr{D}}, \quad \mathscr{D} = c_e\Lambda^-,\\
\psi(\Lambda, c_e) &= \frac{1}{6} + \Lambda(c_e - 1), \quad \xi(\Lambda) = 1 + 30\Lambda(-1 + 4\Lambda).
\end{aligned}
\tag{51c}
$$

Hence, $P^{(eff)}(y')$ is anisotropic and it becomes exact, and hence isotropic, only provided that Λ and c_e are inter-related, as

$$
\begin{aligned}
&P^{(eff)}(y') = P^{(ex)}(y'), \quad \text{if only } \psi(\Lambda_0^{(ex)}, c_e) = 0\ :\\
&(a)\ \theta = 0,\ \forall t_q^{(m)}, \text{ or } \theta = \frac{\pi}{4}, \quad t_c^{(m)} = \frac{1}{3}, \text{ or } e_q^- = 0,\\
&\Lambda_0^{(ex)}(c_e) = \frac{1}{6(1 - c_e)}, \quad \forall\, c_e \in]0, 1[\,;
\end{aligned}
\tag{52}
$$

$$
\begin{aligned}
&(b)\ \forall\,\theta: \text{ if } t_c^{(.)} = \frac{1}{3}, \quad \xi(\Lambda^{(ex)}) = 0, \quad \psi(\Lambda^{(ex)}, c_e{}^{(ex)}) = 0,\\
&\text{then } \Lambda_0^{(ex)}(c_e{}^{(ex)}) = \Lambda^{(ex)}, \text{ with}\\
&\Lambda^{(ex)} = \frac{\sqrt{105} + 15}{120} \approx 0.210\,391,\\
&c_e{}^{(ex)} = \frac{\sqrt{105} - 5}{\sqrt{105} + 15} \approx 0.207\,825\,.
\end{aligned}
\tag{53}
$$

The pure diffusion rotated solution is exact with $\Lambda = \Lambda_0^{(ex)}(c_e)$, Eq. (52). In the presence of advection, the diagonal channel $\theta = \frac{\pi n}{4}$ also gets the exact solution with $\Lambda_0^{(ex)}(c_e)$ giving the hydrodynamic mass-weight. However, in the rotated system, $\Lambda_0^{(ex)}(c_e)$ is restricted to $\Lambda^{(ex)}$ with the particular solution $c_e{}^{(ex)}$ from Eq. (53). We substitute now velocity and mass-source profiles from Eq. (45); Eq. (51) then reads with $\{p_k^{(ex)}\}$ from Eq. (46), and $\mathscr{M}^{(ex)}(y')$ gets the effective correction $\mathscr{E}(y') = -\mathscr{D}\partial_{y'}^2 P^{(eff)} - \mathscr{M}^{(ex)}$:

$$
\begin{aligned}
\mathscr{M}^{(eff)}(y') &= \mathscr{M}(\mathscr{U}^{(ex)}, y') + \mathscr{E}(y'),\ \mathscr{E}' = \frac{\mathscr{E}}{\mathscr{D}},\\
\langle \mathscr{E}' \rangle &= \frac{12\mathrm{Pe}\psi(\Lambda, c_e)}{h^2} + \frac{\mathrm{Pe}^3 \sin^2[4\theta]\xi^2(\Lambda)}{2h^8}.
\end{aligned}
\tag{54}
$$

Given that $\langle \mathscr{M}(\mathscr{U}^{(ex)}, y') \rangle = 0$, the effective profile $P^{(eff)}(y')$ may satisfy the impermeable condition on the two walls only provided that

$$
\begin{aligned}
&\langle \mathscr{E}' \rangle = 0 \text{ with } \Lambda = \Lambda^{(eff)}(\theta, c_e, \mathrm{Pe}, h)\,;\\
&\Lambda^{(eff)}|_{c_e = c_e{}^{(ex)}} = \Lambda_0^{(ex)}(c_e{}^{(ex)}) = \Lambda^{(ex)}, \quad \forall \theta,\ \mathrm{Pe},\ h\,;\\
&\Lambda^{(eff)}|_{h\to\infty} \to \Lambda_0^{(ex)}(c_e).
\end{aligned}
\tag{55}
$$

Here, $\Lambda^{(eff)}$ solves the quartic polynomial equation $\langle \mathscr{E}' \rangle = 0$, and it reduces to Eq. (52) in the grid-aligned case. Figure 6 displays the suitable real root to Eq. (55) in the advection-dominant limit $c_e \to 0$ when $\mathrm{Pe} = \{10, 10^2, 10^3\}$, vs $\phi \in [0, \frac{\pi}{4}]$ (left diagram) and vs H (right diagram, with $h = H\cos[\theta]$, $\theta = \arctan[\frac{1}{2}]$). This root is delineated by a narrow (suitable) interval $\Lambda^{(eff)} \in [\frac{1}{6}, \Lambda^{(ex)}]$, where $\Lambda^{(eff)}|_{c_e\to 0}$ rapidly reduces to $\Lambda \approx \frac{1}{6}$ when Pe is small or when h increases. The difference with respect to the exact solution in Eq. (47) reads on the normalized profiles:

$$
\begin{aligned}
\frac{P^{(eff)} - P^{(ex)}}{\mathrm{Pe}\, h} &= (1 - 3Y)^2\left(\frac{\psi(\Lambda, c_e)}{3h^2} + \frac{\mathrm{Pe}^2\xi(\Lambda)^2\sin^2[4\theta]}{12h^8}\right)\\
&\quad - \frac{(1 - 6Y^2 + 4Y^3)\mathrm{Pe}\xi(\Lambda)\sin[4\theta]}{8h^4}.
\end{aligned}
\tag{56}
$$

Equation (56) only vanishes with $\{\Lambda^{(ex)}, c_e{}^{(ex)}\}$ from Eq. (53), and Eq. (56) is exactly *asymmetric* with respect to exchange $Y \to 1 - Y$ only with $\Lambda^{(eff)}(c_e)$. Figure 7 displays the anisotropic asymmetric solution $h^3\mathrm{Pe}^{-2}(P^{(eff)} - P^{(ex)})(Y)$ using $\Lambda^{(eff)}$; we find that this distribution becomes practically $h-$ and Pe-independent when $\Lambda^{(eff)}$ approaches its asymptotic values, e.g., when $H \geq 10$, $\mathrm{Pe} = 10^2$ or $H \geq 20$, $\mathrm{Pe} = 10^3$ in Fig. 6.

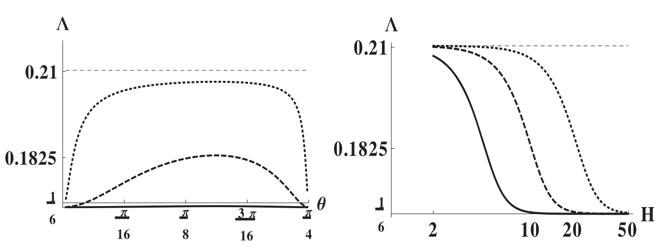

FIG. 6. Effective quartic-polynomial solution $\Lambda^{(eff)}(\theta, c_e, \mathrm{Pe}, h)$ from Eq. (55) with $h = H\cos[\theta]$. Left: $\Lambda^{(eff)}|_{c_e\to 0}$ vs $\theta \in]0, \frac{\pi}{4}[$ when $H = 10$. Right: $\Lambda^{(eff)}|_{c_e\to 0}$ vs H when $\theta = \arctan[\frac{1}{2}]$. Legend: $\mathrm{Pe} = 10^2$ (solid), $\mathrm{Pe} = 10^3$ (dashed), $\mathrm{Pe} = 10^4$ (dotted). The constant asymptotes are $\Lambda^{(ex)} \approx 0.21$ from Eq. (53) and $\Lambda_0^{(ex)}|_{c_e\to 0} = \frac{1}{6}$ from Eq. (52).

To sum up, our analysis suggests that when using $\Lambda^{(eff)}(c_e)$, the bulk system may satisfy the exact solvability condition, but one should expect the (anisotropic, asymmetric) discrete effects, which scale non-linearly with Pe and decay for finer resolutions when Pe grows. Clearly, this advection-diffusion rotated discrete behavior is very different from the isotropic symmetric pure-diffusion or grid-aligned profiles obeying the linear Pe-scale with Eq. (46). The effective solution becomes exact only with $\Lambda^{(ex)}$ and ${c_e}^{(ex)}$ from Eq. (53).

C. Reconstruction step

The standard reconstruction step is computed with Eq. (17) where the prescribed post-collision solution in Eq. (18) becomes modified according to Eq. (16), because $\vec{u} = u_\tau(y')\vec{1}_\tau$ and $\mathscr{M}(y')$ vary along the normal direction:

$$\begin{aligned}\hat{n}_q^{+(2)}(\vec{r}) =& t_q^{(a)}\left[c_{qn}\partial_n + c_{q\tau}\partial_\tau\right](Puc_{q\tau}) - t_q^{(m)}c_e\Lambda^- \\ &\times (c_{qn}^2\partial_{nn}^2(P+\Lambda^+\mathscr{M}) + 2c_{qn}c_{q\tau}\partial_{\tau n}^2 P + c_{q\tau}^2\partial_{\tau\tau}^2 P),\end{aligned} \tag{57a}$$

$$\begin{aligned}\hat{n}_q^{-(2)}(\vec{r}) =& t_q^{(m)}c_e(c_{qn}\partial_n(P+\Lambda^+\mathscr{M}) + c_{q\tau}\partial_\tau P) \\ &- t_q^{(a)}\Lambda^+\left[c_{qn}^2\partial_{nn}^2 + 2c_{qn}c_{q\tau}\partial_{\tau n}^2 + c_{q\tau}^2\partial_{\tau\tau}^2\right](Pu_\tau c_{q\tau}).\end{aligned} \tag{57b}$$

The matrix $\mathbf{B}(\vec{r}_b)$ from Eq. (17) then becomes space-dependent and $\mathbf{R}(\vec{r}_b)$ comprises the known terms due to the velocity and mass-source variation, hence $\mathbf{R}(\vec{r}_b)$ then linearly depends upon $P(\vec{r}_b)$ due to the advection term, as exemplified by Eqs. (B3) and (B4). The closure conditions are expressed locally through $\mathbf{Y}[5] = \mathbf{B}^{-1}\mathbf{R}(\vec{r}_b)$, with Eq. (21) in N-MR and Eqs. (12) and (40) in A-LSOB. The whole linear system is solved with respect to the global unknown list Var from Eq. (29) or (33).

D. Exact validation of the effective solution

The effective solution from Eqs. (51)–(56) is first validated numerically with the help of the *fourth-order accurate* Dirichlet [T-PP$^{(eff)}$] and Neumann [T-DFLI$^{(eff)}$] Taylor conditions:

$$\text{T-DFLI}^{(eff)}: -\mathscr{D}\sum_{m=1}^{4}\frac{\delta_n^{(m-1)}}{(m-1)!}\partial_{y'}^m P^{(eff)}|_{\vec{r}_b} = D_n|_{y'=\{0,h\}}, \tag{58a}$$

$$\text{T-PP}^{(eff)}: P^{(eff)} + \sum_{m=1}^{4}\frac{\delta_n^m}{m!}\partial_{y'}^m P^{(eff)}|_{\vec{r}_b} = P|_{y'=\{0,h\}}. \tag{58b}$$

The Dirichlet solution is defined for any Λ; the constant-flux Neumann solution is defined with $\Lambda^{(eff)}$ from Eq. (55); their boundary conditions complete the bulk system. Additionally, following the A-LSOB in Sec. III E, the effective equations: $\hat{n}_q^+(\vec{r}_b) = \hat{n}_q^{+(eff)}(\vec{r}_b)$ and/or $\hat{n}_q^-(\vec{r}_b) = \hat{n}_q^{-(eff)}(\vec{r}_b)$ are prescribed for $N_b - 1$ cut links; $\{\hat{n}_q^+\}^{eff}$ obeys Eq. (48b) with Eq. (51) and, giving $\{e_q^{\pm eff}\}$ and $\{\hat{n}_q^+\}^{eff}$, $\{\hat{n}_q^-\}^{eff}$ is derived with Eq. (15c), using there Eq. (49).

The effective solution is validated when it coincides with the numerical solution $P^{(num)}(y')$ in all grid points; to get rid of the additive constant, the normalization $\langle P\rangle = 0$ of the predicted effective and numerical Neumann profiles is performed via summation. We first prescribe the effective solution for all derivatives in Eq. (58) and confirm that, when using $\{\Lambda^{(ex)}, {c_e}^{(ex)}\}$, the numerical Neumann solution is exact and given by Eq. (46). Using $\Lambda^{(eff)}(c_e)$, the difference between the numerical and exact solutions then coincides with Eq. (56).

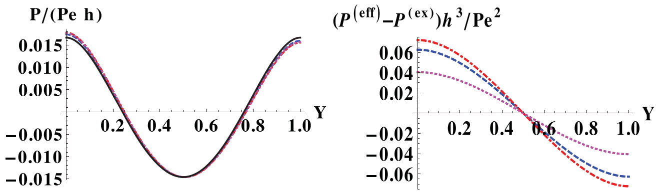

FIG. 7. Quartic-polynomials. Left: the exact normalized Neumann profile from Eq. (47) [solid, black] and the effective anisotropic asymmetric profile from Eq. (56) using $\Lambda^{(eff)}(c_e)$ from Eq. (55). Right: their rescaled difference when $\theta = \arctan[\frac{1}{4}]$ (dashed), $\theta = \arctan[\frac{1}{2}]$ (dotted-dashed), $\theta = \arctan[\frac{3}{4}]$ (dotted). Data: $c_e = \frac{1}{30}$, $h = H\cos[\theta]$, $H = 20$, $\mathrm{Pe} = 10^3$.

We now make use of this benchmark to validate the reconstruction procedure. The first- and second-order derivatives in Eq. (58) are then extracted with Eq. (17) giving there $R_q^{\pm}(\vec{r}_b) = (\hat{n}_q^{\pm} - \hat{n}_q^{\pm(2)}|_{Y=0}) + (\hat{n}_q^{\pm(eff)} - \hat{n}_q^{\pm(2,eff)})$, where the last term accounts for the fourth-order difference between the effective solution and its second-order approximate. Figure 8 displays the difference between the numerical solution obtained in two configurations: $\{\Lambda^{(eff)}(\mathrm{Pe}), c_e = \frac{1}{30}\}$ and $\{\Lambda^{(ex)}, {c_e}^{(ex)}\}$ for Neumann (left diagram) and Dirichlet (right diagram) Taylor conditions from Eq. (58). Here, the rectangular and square reconstructions give the same (effective) solution where $E_2^{(eff)} = 0$ [$E_2^{(eff)}$ is the L_2- error estimate with respect to the constructed effective bulk solution]. In turn, the error-estimate E_2 with respect to exact solution is non-zero unless when using $\{\Lambda^{(ex)}, {c_e}^{(ex)}\}$ from Eq. (53). Figure 8 (left diagram) confirms Eq. (56): the difference with the exact profile is *asymmetric* in the grid-symmetric channel using $\Lambda^{(eff)}$; the Dirichlet system (right diagram) shares the same property of $\Lambda^{(eff)}$, otherwise effective solution loses asymmetry.

It is worthwhile to note that the Neumann numerical solution with $\Lambda^{(eff)}$ finds $M_0 = 0$ in Eq. (28) [because $\langle\mathscr{M}^{(eff)}\rangle = 0$ thanks to $\Lambda^{(eff)}$]. However, when $\Lambda \neq \Lambda^{(eff)}$ and hence $\langle\mathscr{M}^{(eff)}\rangle \neq 0$, the

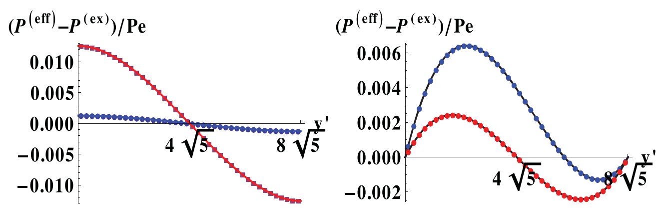

FIG. 8. The difference between two numerical solutions, using $\{\Lambda^{(eff)}(\mathrm{Pe}), c_e = \frac{1}{30}\}$ and $\{\Lambda^{(ex)}, {c_e}^{(ex)}\}$, is compared to its analytical prediction (solid line) from Eq. (56) when $\theta = \arctan[\frac{1}{2}]$, $h = H\cos[\theta]$, $H = 20$. Left: Neumann fourth-order scheme T-DFLI$^{(eff)}$: $\mathrm{Pe} = 10^2$ [$E_2^{(eff)} = 1.04\times10^{-13}$, $E_2 = 4.53\times10^{-3}$] and $\mathrm{Pe} = 10^3$ [$E_2^{(eff)} = 2.98\times10^{-12}$, $E_2 = 4.49\times10^{-2}$]. Right: Dirichlet fourth-order scheme T-PP$^{(eff)}$, $\mathrm{Pe} = 10^3$: $\Lambda^{(eff)}$ [$E_2^{(eff)} = 2.29\times10^{-13}$, $E_2 = 2.4\times10^{-3}$], and $\Lambda = \frac{1}{8}$ [$E_2^{(eff)} = 1.68\times10^{-10}$, $E_2 = 5.24\times10^{-3}$].

condition $\langle \mathscr{M}^{(ex)} = \mathscr{M}^{(eff)} + M_0 \rangle = 0$ becomes satisfied in the grid-aligned system or pure-diffusion problem thanks to the established numerical solution $M_0 = -\mathscr{E}$. Using the exact closure with Eq. (58a), the obtained numerical solution is then exact, as

$$\theta = \frac{\pi n}{4} \text{ or } e_q^- \equiv 0 \ : \ P(y') = P^{(ex)}(y'), \\ \text{with } M_0 = -\mathscr{E} = -\frac{12\mathrm{Pe}}{h^3}\psi(\Lambda, c_e), \quad \forall \Lambda, \forall c_e. \tag{59}$$

E. Exact solutions with inexact boundary schemes

We examine the straight system using $\Lambda_0^{(ex)}$ from Eq. (52); the bulk solution is then exact, $E_2 = E_2^{(eff)}$, and any eventual deviation is due to the boundary closure. Its solvability condition is adjusted with one of the two mechanisms: (i) via $M_0 \neq 0$ in Eq. (28), and (ii), via the corrective flux $\pm\Phi_0 = \pm\mathscr{D}\chi$ in Eq. (32). We first examine the difference between these two techniques for a midway impermeable boundary $\delta = \frac{1}{2}$, where FLI reduces to BB and the numerical solution reads with

$$M_0 - \mathrm{BB} \ : \ E_2 \neq 0, \ M_0 = \mathscr{M}(\mathscr{U}^{(sum)}, y) - \mathscr{M}(\mathscr{U}^{(ex)}, y) \\ = \mathscr{U}^{(sum)} - \mathscr{U}^{(ex)} = \frac{\mathscr{U}^{(ex)}}{2h^2}; \tag{60a}$$

$$\Phi_0 - \mathrm{BB} \ : \ E_2 = 0, \ \chi = \frac{\mathrm{Pe}}{4h^2} \text{ or } \frac{\Phi_0}{\mathscr{U}^{(ex)}h} = \frac{1}{4h^2}. \tag{60b}$$

Equation (60a) means that the BB system adjusts the exact (integration) solvability condition to summation in Eq. (45), in agreement with our prediction in Eq. (31), but the numerical solution is then inexact. The magnitude of M_0 scales with the mean-velocity amplitude, similarly to the case[40] of grid-rotated constant velocity; when $\mathscr{U}$ is kept constant, $|M_0|$ reduces as h^{-2} at fixed Pe. In contrast, BB $-$ Φ_0 produces the exact solution because the corrective flux in Eq. (60b) compensates the BB error with respect to the fourth-order accurate Neumann condition; this result is derived by Eqs. (C1)–(C7). Equation (60b) shows that χ reduces with second-order rate at fixed Pe. The total corrective flux, $2\Phi_0 = \frac{\mathscr{U}}{2h}$ is then equal to $\langle M_0 \rangle = M_0 h$. However, only the corrective flux reproduces the exact profile, because it does not modify the mass-source $\mathscr{M}(\mathscr{U}^{(ex)}, y)$. Equation (C8) extends $\chi(\delta)$ to an arbitrary distance δ with FLI, and Eq. (C14) generalizes this construction for FLI, FMR and DFLI, as

$$\mathrm{FLI} \ : \ \chi(\delta) = \frac{\mathrm{Pe}}{h^2}\left(3\delta^2 - \frac{1}{2} + \frac{\delta(1-4\delta^2)}{h}\right), \tag{61a}$$

$$\mathrm{FMR} \ : \ \chi(\delta) = \chi|_{\mathrm{FLI}} + \frac{3\mathrm{Pe}(h-1-2\delta)(2\Lambda_0^{(ex)} - \delta^2)}{h^3}, \tag{61b}$$

$$\mathrm{DFLI} \ : \ \chi(\delta) = \chi|_{\mathrm{FMR}} + \frac{3\mathrm{Pe}\delta(h-1-2\delta)(1+\delta)}{h^3}, \\ |\chi|_{\mathrm{DFLI}} > |\chi|_{\mathrm{FMR}} \text{ when } h \geq 4, \ \delta > 0, \\ \chi_{\mathrm{DFLI}} = \chi_{\mathrm{FMR}} \text{ when } \delta = 0. \tag{61c}$$

These results show that DFLI needs a larger amplitude Φ_0 than FMR, except when $\delta = 0$. The inter-relation between DFLI and FLI is more complicated, but typically $|\chi|_{\mathrm{DFLI}} > |\chi|_{\mathrm{FLI}}$, e.g., $\forall\delta >\approx 0.09$ when $h \geq 4$, and $\forall\delta >\approx 0.03$ when $h \geq 10$. Figure 9 (left diagram) compares the three schemes in the limit $c_e \to 0$, featuring the high Pe regime. The results are displayed for $\frac{\Phi_0}{\mathscr{U}^{(ex)}h} = \frac{\chi}{\mathrm{Pe}}$ when $\delta = \{\frac{5}{8}, \frac{1}{2}, \frac{1}{8}\}$.

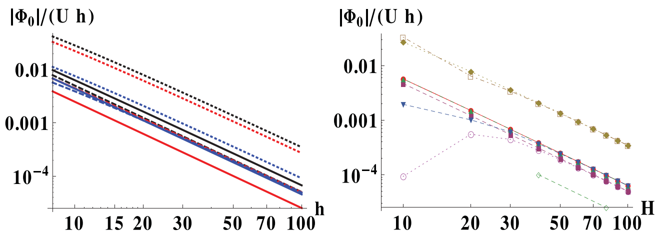

FIG. 9. Quartic solution is exact in the straight symmetric channel with all flux schemes using $\Lambda_0^{(ex)}(c_e)$ thanks to the corrective flux $\pm\Phi_0$ from Eq. (32). Left: analytical prediction $|\Phi_0|/(\mathscr{U}h) = |\chi(\delta)|/\mathrm{Pe}$ vs h from Eq. 61 with FLI (solid), FMR (dashed) and DFLI (dotted) when $\delta = \{\frac{5}{8}, \frac{1}{2}, \frac{1}{8}\}$ and $c_e \to 0$; note: FLI is c_e- independent and FLI($\delta = \frac{1}{2}$) = BB. Right: numerical result $|\Phi_0|/(\mathscr{U}h)$ vs h when $\delta = \frac{5}{8}$, $c_e = \frac{1}{30}$ with FLI$_n$ ●, FMR$_n$■, DFLI$_n$◆, T-DFLI$_r$▲, N-FLI$_r$▼, N-FMR$_r$ ◯, N-DFLI$_r$□, H^{-2}◇.

They show that DFLI requires a much larger amplitude Φ_0 to adjust the exact straight quartic solution, and confirm that DFLI approaches FMR when δ tends to zero. In turn, FMR shows an almost δ—independent amplitude $|\Phi_0|$. The FLI also approaches FMR when $\delta \to 0$, but FLI is more accurate than the two other formally higher-order accurate schemes, when it comes down to BB for $\delta = \frac{1}{2}$. The FLI$_n$, FMR$_n$, and DFLI$_n$ are supplemented with the normal mass-source correction [$I_n^{(\mathscr{M})} = 1$ in Eq. (21)] because $\mathscr{M}(y')$ varies along the normal direction (see Table III). The steady-state MR closure from Eq. (34) then reads with $\mathscr{E}_q^{(-)}(y_b) = \mathrm{CL}_{qn}(\Lambda^+\mathscr{M}, 0)$ from Eq. (24b). This correction modifies $\chi(\delta)$ equally with the three schemes and it is given by Eq. (C11):

$$\chi(\delta) \to \chi(\delta) + \delta\chi, \ \delta\chi < 0 \text{ with} \\ \delta\chi = \left.\frac{\mathscr{E}_{q_b}^{(-)}(y_b)}{\mathscr{D}t_q c_{q_b y}^2}\right|_{\Lambda=\Lambda_0^{(ex)}} = -\frac{c_e \mathrm{Pe}}{(1-c_e)h^2}. \tag{62}$$

Since Φ_0 is positive in Eq. (60b), and it is mostly positive in Eq. (61) when $h \geq 4$, the mass-source correction reduces the amplitude $|\chi|$. The derived solution $|\chi|$ is in exact agreement with the FLI$_n$, FMR$_n$ and DFLI$_n$ numerical solutions displayed in Fig. 9 (right diagram). Additionally, Eq. (C12) demonstrates that the Taylor scheme T-DFLI produces the same solution $\Phi_0(\delta)$ as FLI$_n$; this property is independent of the reconstruction procedure provided that T-DFLI prescribes the unknown vertical population with Eq. (57), according to example 4 in Subsection B of the Appendix.

The MR solutions with the three basic flux schemes are weight-independent in the straight channel, so that they are the same with d2q5 and d2q9. In other words, the accommodation of the advective flux by the diagonal links is invisible on the profiles due to the symmetry. The N-MR complements FLI$_n$, FMR$_n$ and DFLI$_n$ with the tangential correction $\mathrm{CL}_{q\tau}(P, u_\tau P)$ from Eq. (57) [$I_\tau = 1$ in Eq. (21)]. We observe that their profiles $P^{(num)}(y')$ remain exact, but the reconstructed tangential and mixed derivatives in $\mathbf{Y}[5]$ are due to the non-equilibrium accommodation, and they depend on the reconstruction subset. Figure 9 (right diagram) compares $|\Phi_0|$ between MR$_n$ and N-MR using rectangular reconstruction with Eq. (20). We observe that on the coarse grids N-FLI$_r$ and N-FMR$_r$ reduce $|\Phi_0|$ of their counterparts, FLI$_n$ and FMR$_n$, while the N-DFLI$_r$ and DFLI$_n$ behave very similarly. All schemes approach their MR_n counterparts when $H \approx 30$, and then monotonously reduce $|\Phi_0|$ with second-order rate.

To sum up, the corrective flux from Eq. (32) is able to adjust the exact quartic Neumann solution of the inexact flux schemes provided that the two straight walls are placed symmetrically. Although DFLI is exact on the parabolic rotated solutions, it is expected to behave worst on the quartic solutions because of its larger deviations from the exact solvability condition; consequently, N-DFLI$_r$ does not improve DFLI. The MR_n typically decreases $|\Phi_0|$ and hence, it improves for the conservation properties. The diffusive-flux A-LSOB T-DFLI from Eq. (12b) produces an identical solution $\Phi_0(\delta)$ with FLI$_n$ using the standard reconstruction algorithm; hence, T-DFLI shows smaller amplitude $|\Phi_0(\delta)|$ than DFLI, which is its MR counterpart. The N-MR releases the diagonal-link accommodation of the tangential advective flux; it retains the exact solution and further reduces $|\Phi_0|$, at least with the N-FLI$_r$ and N-FMR$_r$ on the coarse grids. Finally, the MR_n and their N-MR counterparts decay $|\Phi_0(\delta)|$ altogether with second-order rate.

F. Grid-shifted and diagonal channels

When the distances to the top and bottom walls differ, say $\delta_T \neq \delta_B$, Eq. (32) should be modified by prescribing $\{\chi(\delta_B), -\chi(\delta_T)\}$, and the numerical solution then remains exact. However, we restrict this work to an equal amplitude corrective flux with Eq. (32), where the numerical solution is then not exact. Figure 10 compares the results obtained with M_0 and Φ_0 when the whole slab is shifted with respect to the grid. We observe that T-DFLI and FLI$_n$ continue to produce the same solutions. On the whole $E_2(\Phi_0)$ is one order of magnitude smaller than $E_2(M_0)$, especially with $\text{FMR}_n - \Phi_0$ where E_2 is the smallest and it converges faster, with third-order rate; otherwise, E_2, M_0 and Φ_0 converge with second-order rate with all schemes. The FMR_n is much more accurate than FLI$_n$ because it vanishes the second-order advection accommodation term but FLI$_n$ demonstrates the best solvability properties, with the smallest amplitudes of $|M_0|$ and $|\Phi_0|$. In addition, Fig. 10 displays the N-MR results using the rectangular reconstruction from Eq. (20). The N-FLI$_r$ then improves FLI$_n$ for E_2, M_0 and Φ_0 but only on coarse grids $H \leq 20$, and the two schemes decay together on the finer grids. Similarly, N-FMR$_r$ improves FMR_n for M_0 and Φ_0, but $E_2(\text{N-FMR}_r)$ is not regular. This confirms our suggestion that FMR does not need any second-order tangential advection corrections in the straight channels, in agreement with the exactness of its parabolic solution. Like FMR, the DFLI copes better with Φ_0, where N-DFLI$_r$ reduces the error on coarse grids but again, the DFLI$-$ based schemes show much larger errors and one-order larger amplitude for $|M_0|$ and $|\Phi_0|$ against FLI and FMR. In turn, N-MR produces similar results using the square-matrix reconstruction, where it maintains the parametrization, meaning that E_2 is fixed by the grid Pe number $\mathscr{U}/\mathscr{D}_0$, c_e and $\Lambda(c_e)$. In contrast, the rectangular reconstruction loses the bulk parametrization property, unless on the exact solutions.

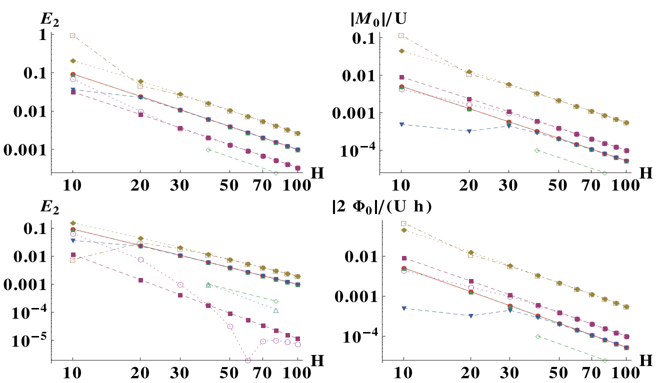

FIG. 10. Quartic-polynomial problem when the straight channel $h = H$ is uniformly shifted with by $\frac{1}{4}\vec{1}_y$ from the mid-grid boundary position. The ADE numerical solution with two strategies: M_0 from Eq. (28) (top row), and Φ_0 from Eq. (32) (bottom row) using FLI$_n$●, FMR$_n$■, DFLI$_n$◆, T-DFLI$_r$ ▲, N-FLI$_r$▼, N-FMR$_r$◯, N-DFLI$_r$□, H^{-2}◇, H^{-3} △; FLI$_n$ overlaps with the T-DFLI and T-DFLI$_r$. Data: $\text{Pe} = 10^2$, $\mathscr{U} = 1$, $c_e = \frac{1}{30}$, $\Lambda_0^{(ex)}(c_e)$, $\delta_B = 3/8$, $\delta_T = 5/8$.

Another important property refers the weight-independence and the linear Pe-scale of the numerical solutions. The unmodified MR schemes and T-DFLI produce weight-independent solutions in the straight grid-shifted channels, where they also retain the linear Pe-dependency of the analytical profile. These two features are not supported by the N-MR on the quartic profiles, either with the square- or rectangular reconstructions. We suggest that this spurious effect is induced via a complex accommodation dependency upon the weights and Pe inserted by the diagonal links into reconstructed tangential corrections. It follows that the results displayed in Fig. 10 are weight- and Pe-independent only with FLI$_n$ = T-DFLI, FMR_n and DFLI$_n$. These results confirm our expectation that the d2q9 MR flux schemes do not need any tangential corrections in the *steady-state straight homogeneous* solutions, to be contrasted with their necessity in the presence of the non-zero tangential boundary flux,[17,62] the heterogeneous interface weights[28] or for the *transient* BB simulations in the uniform velocity field.[26] Indeed, one should keep in mind that the harmful tangential boundary effect is much smaller on the parabolic profile $u_\tau(y')$ considered here than when u_τ is constant, because $u_\tau(y')$ vanishes on the wall. This difference was clearly quantified[33,36] on the effective retardation of the mean velocity, which is the first-order distribution moment.

We extend now these simulations to the symmetric diagonal slab, where the d2q9 weight-stencil excites the $\text{A}-$layer equilibrium accommodation on the implicit-interface quartic profiles.[39] The homogeneous solution remains exact using the fourth-order accurate boundary closure from Eq. (58), thanks to $\Lambda_0^{(ex)}$ and isotropic weights. Figure 11 addresses M_0- and Φ_0- results obtained with the second-order schemes: the straight channel alike, Φ_0 produces better accuracy and exhibits the third-order convergence rate [this is against the exact solution in the straight channel]; N-MR and MR then produce similar results; FMR_n remains the most accurate but FLI$_n$ shows smaller $|\Phi_0|$ (and also $|M_0|$) on the coarse grids, very closely followed by the N-FLI$_r$ and the Taylor scheme T-DFLI. The $|M_0|$ behaves very similarly with $|2\Phi_0/h|$ but FMR_n slows its convergence due to M_0 mass-source correction, and M_0- results all decay with second-order rate, where FLI$_n$, N-FLI$_r$ and T-DFLI are the most accurate.

When the whole slab is shifted with respect to the grid, and the discrete solution breaks the symmetry, the Φ_0 results (not shown here) are very similar to the straight shifted channel in Fig. 10. In that case, only FMR_n and N-FMR$_r$ decay with third-order rate but N-FMR$_r$ is

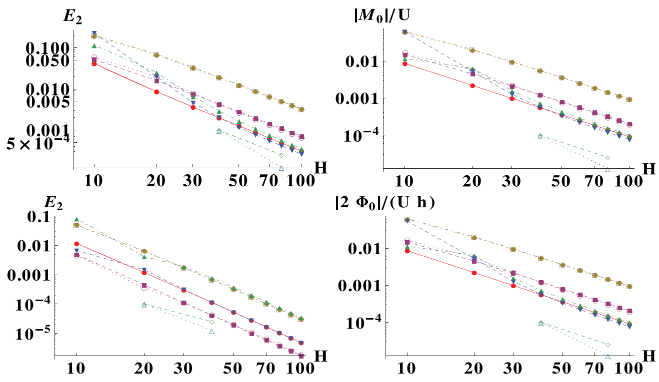

FIG. 11. Quartic-polynomial problem in grid-symmetric diagonal channel shifted by $\delta_B = -\frac{1}{4}$ and $\delta_T = \frac{1}{4}$ along $\vec{1}_y$, with Eq. (28) (top row) and Eq. (32) (bottom row) using FLI$_n$ ●, FMR$_n$■, DFLI$_n$◆, T-DFLI▲, N-FLI$_r$▼, N-FMR$_r$ ○ N-DFLI$_r$□, H^{-2}◇, H^{-3}△. Data: Pe $= 10^2$, $\mathcal{U} = 1$, $c_e = \frac{1}{30}$, $\Lambda_0^{(ex)}(c_e)$, $\delta_B = \delta_T = \frac{5}{8}$ along y.

irregular on the coarse grid; the DFLI continues to show the worst results. The T-DFLI$_r$ behaves similarly to FLI$_n$ when $H \geq 20$ but it is very inaccurate when $H = 10$ because of the rectangular reconstruction. We will systematically observe that T-DFLI$_r$ is much less accurate on the coarse grids compared to the square reconstruction, but the latter one is geometry-dependent.

G. Rotated channels

We model now a rotated channel $\theta = \arctan[\frac{1}{2}]$ with the isotropic (hydrodynamic) advection-diffusion weights. Unless indicated, we prescribe $\{\Lambda^{(ex)}, c_e{}^{(ex)}\}$ from Eq. (53), so that $P^{(eff)}(y')$ is exact in bulk and $E_2 = E_2^{(eff)}$. However, inexact boundary schemes do not reproduce the exact solution and hence, they are subject to truncation effects, such as the anisotropy and the loss of symmetry; also, E_2 becomes Pe- and weight-depending with all schemes. According to Fig. 6, one might expect that the anisotropic bulk effect is still relatively weak when Pe $\leq\approx 10^2$, but it rapidly increases on the coarse grid when Pe $= 10^3$. Figures 12 and 14 display the numerical profiles with the Dirichlet and Neumann conditions, respectively, on the coarse grid $H = 20$ when Pe $= 10^2$ and Pe $= 10^3$. The fourth-order accurate Taylor schemes T-PP$^{(eff)}$ and T-DFLI$^{(eff)}$ from Eq. (58) match $P^{(ex)}(y')$ exactly; otherwise, E_2 is given in Tables IV and V.

We examine first the Dirichlet boundary schemes prescribing $P|_{y'=\{0,h\}} =$ Pe; the exact profile $P(y')/\text{Pe}$ is then Pe-independent. Figure 12 displays the ADE results of (i) linear, one-node MPLI/LMKC and PLI families from Table X; (ii) parabolic in pure diffusion, new single-node PPLI scheme from Table XII; and (iii) parabolic in constant velocity field, two-node PP family from Table XI; the variation of the mass-source is accounted for by using $I_b = 1$ in Eq. (A4). Additionally, the single-node Taylor schemes T-PP$_r$ and T-PP from Eq. (12a) are examined using, respectively, rectangular and (mainly) square reconstructions. Again, we intentionally degrade Eq. (12a) to the first order with the T-I-PP$_r$ scheme but address it with the parabolic-accurate rectangular reconstruction.

Figure 12 (left diagram) shows that all schemes match the quartic profile on the relatively coarse grid when Pe $= 10^2$. However, unlike in pure-diffusion, the profiles are not symmetric and they do not scale exactly with Pe. These effects grow rapidly with Pe and only those schemes where the leading-order advection projections are absent, like the PP, T-PP$_r$, and T-PP, but also a less accurate T-I-PP$_r$, retain the profile shape when Pe $= 10^3$. The PLI is expected to overcome MPLI when Pe grows, because PLI removes the first-order advection gradient from its closure relation.[40] Table IV confirms that although MPLI is more accurate than the two other linear schemes, PLI and T-I-PP$_r$ in pure diffusion and Pe $= 10^2$, the T-I-PP$_r$ gains over them at Pe $= 10^3$. In turn, according to Table IV, the PPLI overpasses not only MPLI/PLI but also PP and A-LSOB T-PP/T-PP$_r$ in the pure-diffusion regime. However, as was expected, the PPLI accuracy worsens in the presence of a grid-inclined velocity field, very similarly to MPLI/LMKC.

Figures 13 displays $E_2(H)$; it confirms that when Pe $= 10^2$, PLI gains over MPLI/PPLI only for $H = 10$, but it is more accurate over the long interval $H <\approx 80$ when Pe $= 10^3$. In turn, the PPLI asymptotically approaches PP and converges with the third-order rate when Pe $= 10^2$, but it decays slower together with MPLI when Pe $= 10^3$. The PP systematically gains over the LI schemes, especially when Pe increases, and converges smoothly. The T-PP$_r$ and T-PP behave very similarly, they are the most accurate on the finer grids, here when $H \geq 20$ with Pe $= 10^2$, because their closure relation is free of the advection projection; however, their reconstruction is not smooth when Pe $= 10^3$. The employed LI and MR Dirichlet schemes are all parametrized, and their results are set by Pe, c_e, Λ and H. The T-PP$_r$ does not maintain the parametrization; the T-PP is parametrized when it employs only square subsets in Eq. (17); otherwise, T-PP loses the parametrization property when it (optionally) uses the rectangular matrix in single cut link nodes following the algorithm from **example 4** in Subsection B of the Appendix.

Figure 14 shows similar results with the Neumann schemes; here we additionally consider the degraded T-I-DFLI$_r$, where we omit the parabolic term in Eq. (12b) but retain the reconstruction process. Figure 14 (left diagram) shows that the T-I-DFLI$_r$ is the least accurate at Pe $= 10^2$, and its E_2 exceeds FLI$_n$ by about two orders of magnitude in pure diffusion according to Table V. When Pe $= 10^3$, all schemes become affected by the loss of symmetry, and this effect becomes most noticeable with the diffusive-flux parabolic schemes, DFLI$_n$ and T-DFLI$_r$ [T-DFLI produces similar results], whereas the degraded

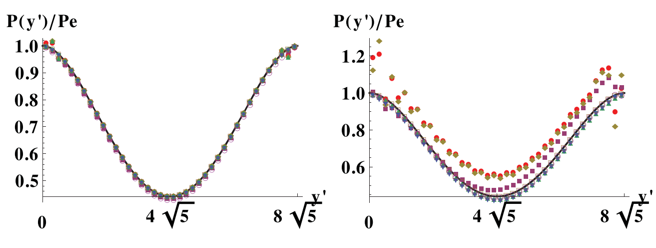

FIG. 12. Quartic-polynomial rotated Dirichlet solution when $H = 20$. Left: Pe $= 10^2$. Right: Pe $= 10^3$. Exact (solid line) and numerical (symbols) solutions with the Dirichlet schemes MPLI/LMKC●, PLI■, PPLI◆, PP ▲, T-I-PP$_r$▼ [first-order Eq. (12a)], T-PP$_r$○, T-PP$^{(eff)}$□ is exact Data: $P|_{y'=0,h} =$ Pe, $\{\Lambda^{(ex)}, c_e{}^{(ex)}\}$, $\mathcal{U} = 1$, $\theta = \arctan[\frac{1}{2}]$, $(x_0, y_0) = 0$, $h = H\cos[\theta]$; E_2 is gathered in Table IV.

TABLE IV. Quartic-polynomial rotated Dirichlet numerical solution when $H = 20$ using $\{\Lambda^{(ex)}, c_e{}^{(ex)}\}$ (i) in pure diffusion [top line: E_2 is Pe-independent] and (ii) in ADE [$\mathrm{Pe} = 10^2$ and $\mathrm{Pe} = 10^3$ from Fig. 12]: E_2 is fixed by the grid Péclet number except T-I-PP$_r$ [the first-order degradation of Eq. (12a)], T-PP$_r$ and T-PP.

Pe	MPLI	PLI	PPLI	PP	T-I-PP$_r$	T-PP$_r$	T-PP	T-PP$^{(eff)}$
∀ Pe	10^{-2}	1.1×10^{-2}	7×10^{-4}	5.2×10^{-3}	3×10^{-2}	9.5×10^{-4}	10^{-3}	5×10^{-15}
10^2	8.8×10^{-3}	1.1×10^{-2}	1×10^{-2}	5.5×10^{-3}	1.6×10^{-2}	9.8×10^{-4}	1.2×10^{-3}	6.9×10^{-15}
10^3	1.7×10^{-1}	7.5×10^{-2}	1.6×10^{-1}	1.9×10^{-2}	2.9×10^{-2}	1.2×10^{-2}	1.2×10^{-2}	1.2×10^{-13}

TABLE V. Quartic-polynomial rotated Neumann numerical solution when $H = 20$ using $\{\Lambda^{(ex)}, c_e{}^{(ex)}\}$ (i) in pure diffusion [top line: E_2 is Pe-independent] and (ii) in ADE from Fig. 14: E_2 is fixed by the grid Péclet number except T-I-DFLI$_r$ [the first-order degradation of Eq. (12b)] T-DFLI$_r$ and T-DFLI.

E_2 using Eq. (28)							
Pe	FLI$_n$	FMR$_n$	DFLI$_n$	T-I-DFLI$_r$	T-DFLI$_r$	T-DFLI	T-DFLI$^{(eff)}$
∀ Pe	5.6×10^{-3}	1.6×10^{-2}	7.2×10^{-2}	0.39	2.1×10^{-2}	2.1×10^{-2}	0
10^2	7.7×10^{-3}	3×10^{-2}	7.5×10^{-2}	2.46×10^{-1}	1.8×10^{-2}	1.6×10^{-2}	2.8×10^{-15}
10^3	3.5×10^{-2}	2.6×10^{-1}	1.2	4.13×10^{-1}	1.2	3.5×10^{-1}	3.2×10^{-13}
$\lvert M_0\rvert/\mathscr{U}$ in Eq. (28)							
Pe	FLI$_n$	FMR$_n$	DFLI$_n$	T-I-DFLI$_r$	T-DFLI$_r$	T-DFLI	T-DFLI$^{(eff)}$
∀ Pe	1.8×10^{-3}	4.7×10^{-3}	2.2×10^{-2}	−0.12	6.6×10^{-3}	6.8×10^{-3}	8.9×10^{-16}
10^2	1.8×10^{-3}	4.7×10^{-3}	2.3×10^{-2}	-7.04×10^{-2}	4.6×10^{-3}	4.7×10^{-3}	2.8×10^{-15}
10^3	1.3×10^{-3}	$6. \times 10^{-3}$	1.2×10^{-1}	-1.22×10^{-1}	1.2×10^{-1}	5.8×10^{-2}	5.7×10^{-14}

T-I-DFLI$_r$ worsens by a smaller extent because its principal inaccuracy is due to the constant diffusive-flux approximation. Table IX confirms that FLI$_n$ overheads all other schemes, including FMR$_n$, and produces two-order magnitude smaller M_0 than DFLI$_n$ and T-DFLI$_r$ when $\mathrm{Pe} = 10^3$.

Figure 15 addresses the convergence of M_0- and Φ_0- strategies when $\mathrm{Pe} = 10^2$; the basic MR schemes are displayed here together with the N-MR and Taylor schemes T-DFLI and T-DFLI$_r$. The results show that all schemes obey a second-order rate and, except FLI$_n$ and DFLI$_n$/N-DFLI, they almost overlap when $H \geq 20$; FLI$_n$ gains again by a large extent and shows much smaller values of $|M_0|$ and $|\Phi_0|$. In this respect, DFLI$_n$ and N-DFLI remain the least accurate. We note that E_2 is very similar with the two-node FMR/N-FMR and the single-node T-DFLI/T-DFLI$_r$, but the MR schemes show better conservation properties.

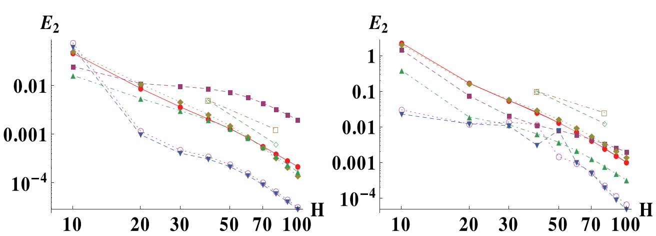

FIG. 13. Quartic-polynomial rotated Dirichlet numerical solution. Left: $\mathrm{Pe} = 10^2$. Right: $\mathrm{Pe} = 10^3$. Dirichlet schemes: MPLI/LMKC●, PLI■, PPLI◆, PP▲, T-PP$_r$▼, T-PP ○, H^{-2}□, H^{-3}◇. Data from Fig. 12.

We employ now $\Lambda^{(eff)}$ from Eq. (55), where the exact solvability condition remains formally valid but the effective profile does not scale with Pe exactly, because of the truncation correction in Eq. (48). Figure 16 compares FLI$_n$ with its five N-MR counterparts from Table III, and with the two Taylor schemes, T-DFLI and T-I-DFLI$_r$. The results are restricted to $\mathrm{Pe} = 10$ because the reconstruction is not always regular at higher Pe. All schemes decay similarly with second-order rate and here only N-FLI$_2$ improves FLI$_n$ in accuracy and convergence due to the smaller amplitude and faster decay of $|\Phi_0(H)|$. Recall, N-FLI$_2$ reconstructs $\mathbf{Y}[5]$ from the two-diagonal and one vertical link [group II(b) in Eq. (19b)]. These results confirm the suitability of the different reconstruction subsets. The Taylor schemes are slightly less accurate than their FLI partners, but they systematically show

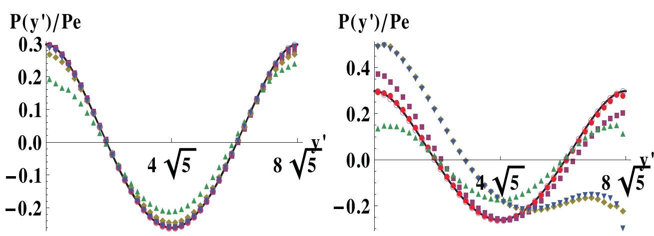

FIG. 14. Quartic-polynomial rotated Neumann solution when $H = 20$. Left: $\mathrm{Pe} = 10^2$. Right: $\mathrm{Pe} = 10^3$. The exact (solid line) and numerical (symbols) solutions with M_0 from Eq. (28) and the flux schemes: FLI$_n$●, FMR$_n$■, DFLI$_n$ ◆, T-I-DFLI$_r$ ▲ [first-order Eq. (12b)], T-DFLI$_r$▼T-DFLI$^{(eff)}$○ is exact. Data: $\Phi_n|_{y'=\{0,h\}} = 0$, $\{\Lambda^{(ex)}, c_e{}^{(ex)}\}$, $\mathscr{U} = 1$, $\theta = \arctan[\frac{1}{2}]$, $(x_0, y_0) = 0$, $h = H\cos[\theta]$. E_2 and M_0 are gathered in Table V.

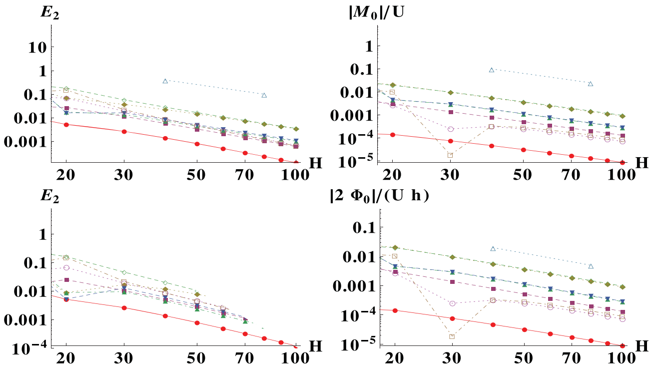

FIG. 15. Quartic-polynomial rotated Neumann solution. Top row: $E_2(H)$ and $|M_0(H)|/\mathscr{U}$. Bottom row: $E_2(H)$ and $|2\Phi_0(H)|/(\mathscr{U}h)$. Flux schemes: FLI$_n$ ●, FMR$_n$■, DFLI$_n$◆, T-DFLI$_r$▲, T-DFLI▼, N-FLI$_r$◯, N-FMR$_r$□, N-DFLI$_r$ ◇, H^{-2}△. Data: Pe $= 10^2$, $\mathscr{U} = 1$, $\{\Lambda^{(ex)}, c_e{}^{(ex)}\}$, $\theta = \arctan[\frac{1}{2}]$, $(x_0, y_0) = 0$, $h = H\cos[\theta]$.

noticeably larger amplitude $|\Phi_0|$. Finally, Fig. 17 shows that the FLI$_n$ produces very similar E_2, $M_0(\mathrm{Pe}, H)$ and $\Phi_0(\mathrm{Pe}, H)$ in all six computations with $\mathrm{Pe} \in \{10, 10^2, 10^3\}$; as usually, $\Phi_0 -$ FLI$_n$ slightly overpasses $M_0 -$ FLI$_n$. The original FLI produces nearly the same results, because the normal source correction becomes almost negligible when c_e is small. This example tells us that, without reconstruction, FLI/FLI$_n$ is not much affected by the truncated non-linear Pe-dependency.

H. Solution independence over an additive constant

When the problem is closed by a constant diffusive flux, solution to Eq. (48a) is defined up to an additive constant, say p_0. Hence, the solution independence over an additive constant should be verified for any diffusive-flux and a theoretically equivalent, advective-diffusive flux scheme. However, this question was not ever raised to the best of our knowledge unless very recently.[40] The Neumann simulations reported above fix $P(x, y)$ to some (arbitrary) value in some (arbitrary) point, typically we prescribe $P|_{x=\frac{1}{2}, y=\frac{1}{2}} = 0$ or $P|_{x=\frac{1}{2}, y=\frac{1}{2}} = 1$. The proposed solvability techniques then add one variable, M_0 or Φ_0, to the global unknown list in Eqs. (29a) and (33), and the global linear system becomes invertible. The error estimate is computed *a posteriori* on the normalized analytical and numerical solutions, e.g., obeying condition $\langle P \rangle = 0$, and hence E_2 is expected to be independent of the fixed value. This property was confirmed[40] with the basic MR schemes

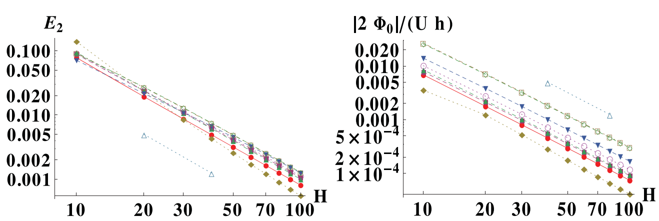

FIG. 16. Quartic rotated Neumann solutions at Pe $= 10$. $E_2^{(eff)}(H)$ (left) and $2\Phi_0(H)/\mathrm{Pe}$ (right) with FLI$_n$●, N-FLI$_1$■, N-FLI$_2$◆, N-FLI$_3$▲, N-FLI$_4$▼, N-FLI$_r$◯, T-DFLI□, T-DFLI$_r$◇, H^{-2}△. Data: $\theta = \arctan[\frac{1}{2}]$, $x_0, y_0 = \{\frac{1}{4}, 0\}$, $c_e = \frac{1}{30}$, $\Lambda^{(eff)}(c_e)$ obeys Eq. (55).

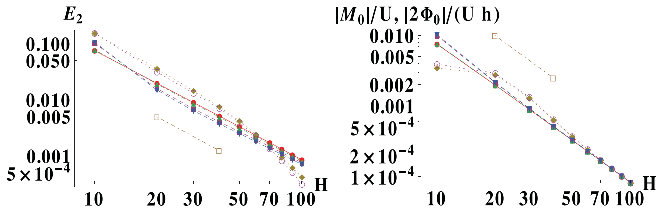

FIG. 17. Quartic rotated Neumann solutions. $E_2(H)$ with the FLI$_n$ using M_0 [Pe $= 10$ ●, Pe $= 10^2$■, Pe $= 10^3$◆] and Φ_0 [Pe $= 10$▲, Pe $= 10^2$▼, Pe $= 10^3$◇]; H^{-2}□. Data: $\theta = \arctan[\frac{1}{2}]$, $\{x_0, y_0\} = \{\frac{1}{4}, 0\}$, $c_e = \frac{1}{30}$, $\Lambda^{(eff)}(c_e)$ obeys Eq. (55).

in the rotated, interface-parallel and interface-perpendicular *constant* velocity field. At the same time, it was observed[39] that $\hat{n}_q^-$, and then the local tangential gradient $c_e\partial_\tau P \approx 2\sum_{q=1}^{Q_m/2} \hat{n}_q^- c_{q\tau}$ becomes non-zero in the translation-invariant direction even with the implicit interface treatment. This effect is attributed to the anti-symmetric truncation correction contained in $\hat{n}_q^-$, which contributes $2\sum_{q=1}^{Q_m/2} t_q^{(a)} \partial_n^2(u_\tau P) c_{qt}^2 c_{qn}^2$ to the local gradient estimate.

We note that the term of $\gamma^{(u)}\hat{n}_q^-$ is different in FLI, FMR and DFLI closure relations, and also, that it depends upon a solution constant in the parabolic velocity profile. Figure 18 demonstrates the difference in the error estimate and M_0 when two arbitrary values are fixed in one point. A very interesting result is that not only FMR, DFLI and T-DFLI, but also all N-MR schemes N-FLI$_r$ − N-FLI$_4$ from Table III produce consistent solutions. In contrast, the FLI and FLI$_n$ produce different normalized solutions with two different values, where the displayed difference in E_2 and M_0 approximately decays in-between second/third rate and third-order rate, respectively. The FLI and FLI$_n$ manifest this artifact not only in the grid-shifted rotated channels, but also in the grid-symmetric ones; the results with Φ_0 follow along this line. Hence, it is suggested that the N-MR removes this free-constant dependency with the help of its tangential corrections of u_τ−terms in Eq. (10).

To sum up, the N-FLI does not improve FLI and FLI$_n$ regularly for accuracy in the parabolic no-slip velocity profiles because of the relatively weak tangential advection effects against the advection truncation and its accommodation. However, it appears that the N-FLI removes the principal advection terms in the non-equilibrium

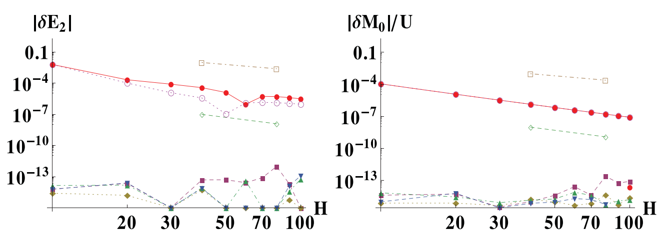

FIG. 18. Dependency upon an additive constant in quartic rotated Neumann profiles: the difference $|\delta E_2|$ and $|\delta M_0|/\mathscr{U}$ when $P(\vec{r}_c) = 10$ and $P(\vec{r}_c) = 20$ are fixed at the same (arbitrary) bulk point $\vec{r}_c(x = \frac{1}{2}, y = \frac{5}{2})$ [$y' = \frac{91\sqrt{5}}{100}$]. FLI$_n$●, FMR$_n$■, DFLI$_n$◆, T-DFLI$_r$▲, N-FLI$_r$▼, FLI◯, H^{-2}□, H^{-3}◇ Data: Pe $= 10^2$, $\mathscr{U} = 1$, $\theta = \arctan[\frac{1}{2}]$, $(x_0, y_0) = \{\frac{1}{4}, 10^{-1}\}$, $\{\Lambda^{(ex)}, c_e{}^{(ex)}\}$.

expansion responsible for the FLI inconsistency. Otherwise, the FLI and FLI_n normalized solution and error-estimate vary together with the solution constant, and therefore, these schemes are to be considered as not reliable, despite their very good conservation properties.

I. Rotated heterogeneous system

We extend now the boundary problem[37] from the grid-aligned implicit-interface TRT-EMM scheme[38,39] to the grid-rotated interface-conjugate treatment. The bulk equation remains the same as described by Eq. (41a), but the stratified system combines now the diffusive porous layer $\phi = \phi_1 \in [0, 1[$ with the open (Poiseuille) profile $\phi_2 = 1$:

$$\begin{aligned} u_\tau(y') &= 0, \quad \boldsymbol{\phi} = \boldsymbol{\phi}_1, \quad y' \in [-h_1, 0], \\ u_\tau(y') &= -\frac{1}{2}\Psi y'(y' - h_2), \quad \boldsymbol{\phi}_2 = 1, \quad y' \in [0, h_2], \\ \mathscr{U} &= \frac{\Psi {h_1}^3}{12(\boldsymbol{\phi}_1 h_1 + \boldsymbol{\phi}_2 h_2)}, \quad \mathrm{Pe} = \frac{\mathscr{U}(h_1 + h_2)}{c_e \Lambda^-}. \end{aligned} \tag{63}$$

The two layers are either periodic [OPL] or impermeable [B − OPL]; the B − OPL reduces to the above considered Poiseuille flow problem when the diffusion-layer vanishes [$h_1 = 0$]. The diffusion coefficients are discontinuous: $\Lambda_1^- = \phi_1 \Lambda^-$ and $\Lambda_2^- = \phi_2 \Lambda^-$; the scalar field $P(y')$ and the diffusive flux $-\mathscr{D}_k \partial_{y'} P(y')$ are set continuous on the interface $y' = 0$. The advective flux reduces to zero together with $u_\tau(y')$ on the interface, and hence, the advective-diffusive flux is also continuous. The effective profile $P^{(eff)}(y')$ combines the parabolic branch (41b) and the effective quartic solution from Eqs. (51) and (56). We apply the interface-conjugate from Eq. (37) with the two-node parabolic PP family for the scalar-field continuity condition and combine it with all developed flux schemes for the flux-continuity condition. The porosity contrast is set equal to 8 for all simulations, for the sake of comparison with our previous results.[38,39]

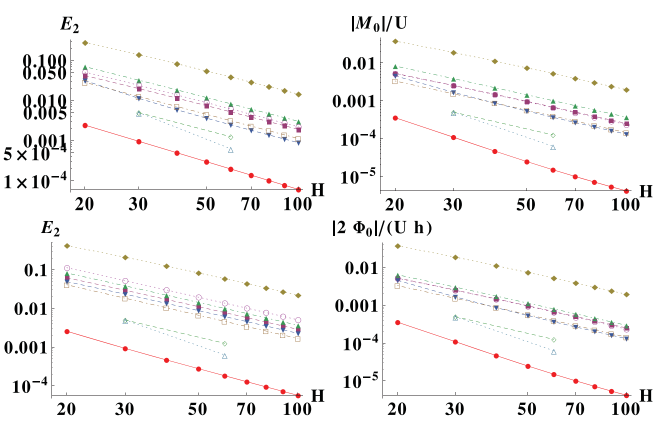

FIG. 19. B − OPL in two equal layers. Top row $E_2^{(eff)}(H)$ (left) and $M_0(H)/\mathscr{U}$ (right). Bottom row: $E_2^{(eff)}(H)$ (left) and $\Phi_0(H)/(\mathscr{U}h)$ with on the boundary-interface: $\mathrm{FLI}_n - \mathrm{FLI}_n$●, $\mathrm{FMR}_n - \mathrm{FMR}_n$■, $\mathrm{DFLI}_n - \mathrm{DFLI}_n$◆, $\mathrm{T\text{-}DFLI}_r - \mathrm{FLI}_n$▲, $\mathrm{N\text{-}FLI}_2 - \mathrm{N\text{-}FLI}_2$▼, $\mathrm{T\text{-}DFLI}_2 - \mathrm{N\text{-}FLI}_2$○, FLI − FLI□, H^{-2}◇ Data: $\mathrm{Pe} = 10$, $\mathscr{U} = 1$, $\phi_1 = \frac{1}{8}$, $\{\Lambda^{(ex)}, c_e^{(ex)}\}$, $\theta = \arctan[\frac{1}{2}]$, $(x_0, y_0) = 0$, $h = H\cos[\theta]$.

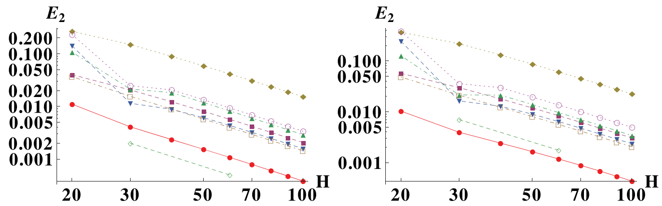

FIG. 20. B-OPL in two equal layers, $E_2^{(eff)}(H)$ with M_0 (left) and Φ_0 (right) using on the boundary-interface: $\mathrm{FLI}_n - \mathrm{FLI}_n$●, $\mathrm{FMR}_n - \mathrm{FMR}_n$■, $\mathrm{DFLI}_n - \mathrm{DFLI}_n$◆, $\mathrm{T\text{-}DFLI}_r - \mathrm{FLI}_n$▲, $\mathrm{N\text{-}FLI}_r - \mathrm{N\text{-}FLI}_r$▼, $\mathrm{T\text{-}DFLI}_r - \mathrm{N\text{-}FLI}_r$○, FLI − FLI□, H^{-2}◇ Data: $\mathrm{Pe} = 10^2$, $\mathscr{U} = 1$, $\{\Lambda^{(ex)}, c_e^{(ex)}\}$, $\theta = \arctan[\frac{1}{2}]$, $(x_0, y_0) = 0$, $h = H\cos[\theta]$.

1. Bounded open-porous layered system, B-OPL

The MR, N-MR and T-DFLI flux schemes are applied on the impermeable solid wall, either using M_0 or Φ_0 for the solvability condition. These two strategies are compared now in the presence of the interface, when the flux-continuity condition is not satisfied exactly. Figures 19 and 20 address the system of two equal symmetric rotated layers when $\mathrm{Pe} = 10$ and $\mathrm{Pe} = 10^2$, respectively. We apply FLI^2 [this abbreviates FLI − FLI applied both on the interface and boundary], and compare it with (i) its MR counterparts involving the normal mass-source correction, as FLI_n^2, FMR_n^2 and DFLI_n^2; (ii) the N-MR partners, as $\mathrm{N\text{-}FLI}_2^2$ or $\mathrm{N\text{-}FLI}_r^2$ from Table III, and (iii), the single-node combinations of the Taylor and N-MR schemes, where $\mathrm{T\text{-}DFLI}_r$ applies for boundary and $\mathrm{N\text{-}FLI}_2$ [or $\mathrm{N\text{-}FLI}_r$] adjusts the interface. Figures 19 and 20 employ the square and rectangular reconstructions, respectively. We recall that all examined schemes are exact for the boundary and interface in two adjacent diffusive layers (STRD restricted to pure-diffusion).

Figure 19 shows that the FLI_n^2 is by far the most accurate and it decays with third-order rate thanks to its best conservation property, while the DFLI_n^2 behaves as the worst, due to its significant deviation from the exact solvability condition manifested again by the large M_0 and Φ_0 magnitudes. All other flux schemes show very similar results of intermediate accuracy: $\mathrm{N\text{-}FLI}_r^2$ behaves slightly better than FLI^2 with M_0, and slightly worse than it with Φ_0, but FLI^2 surpasses FMR_n^2 and the two mixed combinations of the Taylor and MR schemes: $\mathrm{T\text{-}DFLI}_r - \mathrm{FLI}_n$ and $\mathrm{T\text{-}DFLI}_2 - \mathrm{N} - \mathrm{FLI}_2$, which are formally more accurate. The M_0 and Φ_0 techniques also show close results for the E_2 and their respective amplitudes of $M_0/\mathscr{U}$ and $2\Phi_0/(\mathscr{U}h)$.

When $\mathrm{Pe} = 10^2$, the truncation and accommodation grow non-linearly against $\mathrm{Pe} = 10$ in Fig. 19. Figure 20 shows that all schemes then decay with second-order rate; the rectangular reconstruction is not accurate on the coarsest grid, here with a width $h_k = 10\cos[\boldsymbol{\theta}] \approx 8.9$ node per layer. The finer grids show results which are similar with $\mathrm{Pe} = 10$ and confirm the advanced precision of the FLI_n^2 interface/boundary treatment. However, we should emphasize again that the reported values of E_2 depend upon an additive constant in FLI_n^2 and FLI^2.

To sum up, we extended the piece-wise parabolic solutions and confirmed the suitability of the MR and N-MR for the continuous-flux interface-conjugate in the non-uniform velocity profile. The $\mathrm{N\text{-}FLI}^2$

might offer an interesting compromise to FLI^2 and FLI_n^2, because it (i) needs only one interface or boundary point; (ii) shares with FLI_n similar mass-conservation, and (iii) improves FLI^2 and FLI_n^2 for their tangential constraints and a free-constant dependency. However, we find that the important role of the truncation and accommodation at higher Pe, here typically $\mathrm{Pe} \geq 10^3$, corrupts the second-order reconstruction procedure.

2. Periodic open-porous layered system, OPL

We consider now a fully periodic system where the corrective flux from Eq. (32) is extended for interface system and Φ_0 strategy prescribes

$$\begin{gathered} M_0 = 0, \\ || - \mathscr{D}_k \partial_{y'} P||_{y'=0} = ||D_n|| + \Phi_0, \\ || - \mathscr{D}_k \partial_{y'} P||_{y'=h} = ||D_n|| - \Phi_0,\ \Phi_0 = \mathscr{D}\chi. \end{gathered} \tag{64}$$

Like with Eq. (32), Eq. (64) is expected to produce the most accurate results when the two interfaces are placed symmetrically. In the OPL system, the diffusion-flux is continuous, then $||D_n|| = 0$. The OPL is run with M_0 from Eq. (28) and Φ_0 from Eq. (64). Figure 21 addresses the pure diffusive system $e_q^- = 0$ but applies the same mass-source as in Eq. (41a). We confirm that all numerical solutions formally scale with the Pe number and then produce Pe-independent error-estimates. It is interesting to note that $M_0/h = 2\Phi_0/(Uh)$ with all schemes, the straight symmetric Poiseuille flow alike [cf. Eq. (60)]. We observe that $\Phi_0 - \mathrm{FMR}$ and $\Phi_0 - \mathrm{N\text{-}FMR}$ decay with a third-order rate in the absence of the advection terms. Due to the same reason, the N-MR_3 and N-MR_r, exemplified for the square and rectangular reconstruction, show similar results to their counterparts, such as FLI_n and FMR_n. It is curious that, unlike in all previous results, $\Phi_0 - \mathrm{N\text{-}DFLI}_3$ clearly surpasses $\Phi_0 - \mathrm{DFLI}_n$ in pure diffusion. This indicates that although DFLI_n vanishes the uniform-velocity advection terms from its closure relation on the parabolic profiles, its accuracy is impacted by them in the general cases. All M_0-schemes decay with a second-order rate because of the mass-source correction in Eq. (28). On the whole, these results are similar to those in the diagonal flow displayed in Fig. 11 at $\mathrm{Pe} = 10^2$. The last diagram in Fig. 21 confirms that among the Φ_0-schemes, DFLI_n and FMR_n produce, respectively, the largest and smallest deviations from the exact profile.

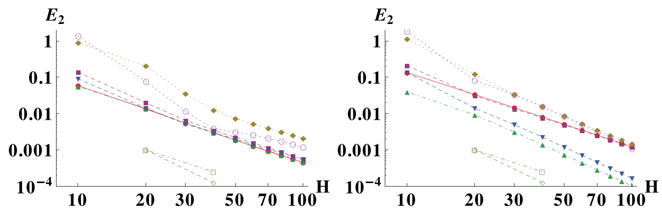

FIG. 22. The same system as in Fig. 21 but in the presence of advection; FLI_n (left) and FMR_n (right). The results are obtained with M_0- strategy: $\mathrm{Pe} = 10$ ●, $\mathrm{Pe} = 10^2$ ■, $\mathrm{Pe} = 10^3$ ◆, and with Φ_0- strategy: $\mathrm{Pe} = 10$ ▲ $\mathrm{Pe} = 10^2$ ▼, $\mathrm{Pe} = 10^3$ ◯, H^{-2} □, H^{-3} △. To compare with FLI_n results in open profile in Fig. 17.

Figure 22 examines the E_2-dependency over Pe with two basic schemes, as FLI_n (left diagram) and FMR_n (right diagram); their results are displayed together using M_0 and Φ_0 when $\mathrm{Pe} = \{10, 10^2, 10^3\}$. When $\mathrm{Pe} \leq 10^2$, $\Phi_0 - \mathrm{FMR}$ monotonously decays with third-order rate, in pure diffusion alike; but $M_0 - \mathrm{FMR}$, and the two FLI schemes, $M_0 - \mathrm{FLI}_n$ and $\Phi_0 - \mathrm{FLI}_n$, decay with second-order rate in agreement with the expectations and previous results. In these simulations, E_2 remains almost Pe-independent, whereas $|M_0|/\mathscr{U}$ and $|2\Phi_0|/(\mathscr{U}h)$ practically coincide between them in all these schemes. However, again, when $\mathrm{Pe} = 10^3$, the M_0 and Φ_0 solutions behave similarly and produce much larger errors on the same grids.

To sum up, these observations confirm that $M_0 - \mathrm{FMR}$ is dominated by the second-order bulk accuracy of the M_0- strategy in the pure diffusion and intermediate Pe range, but both M_0 and Φ_0 solutions are dominated by the Pe-dependent truncation and its interface-accommodation at high Pe. We note that the boundary systems alike, (i) the results of FLI and FLI_n depend upon an additive constant in the fully periodic OPL, and (ii) the N-MR removes this deficiency but becomes irregular when Pe grows.

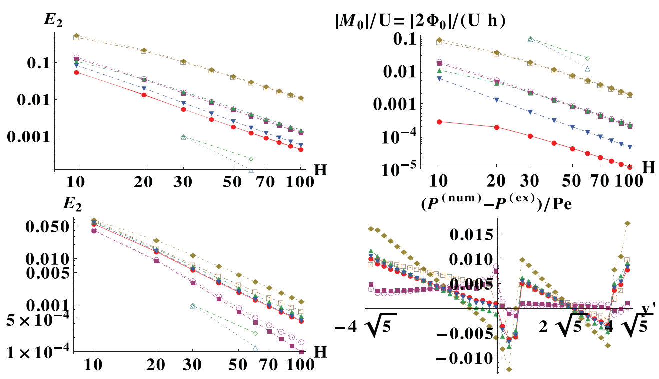

FIG. 21. Pure diffusion in grid-symmetric OPL$-$ system. Top row: $E_2(H)$ with M_0 (left) and $|M_0(H)|/\mathscr{U} = 2|\Phi_0(H)|/(\mathscr{U}h)$ (right). Bottom row: $E_2(H)$ and $(P^{(num)}(y') - P^{(ex)})/\mathrm{Pe}$ using Φ_0 with Eq. (64) when $y' \in [-h/2, h/2]$, $h = H\cos[\theta]$, $H = 20$, interface-flux condition: FLI_n●, FMR_n■, DFLI_n◆, N-FLI_r▲, N-FLI_3▼, N-FMR_3 ◯, N-DFLI_3 □, H^{-2}◇, H^{-3}△. Data: $\mathscr{U} = 1$, $\mathrm{Pe} = 10^3$ [but E_2 is Pe-independent] $\{\Lambda^{(ex)}, c_e{}^{(ex)}\}$, $\theta = \arctan[\frac{1}{2}]$, $(x_0, y_0) = \{\frac{1}{4}, 0\}$, $h = H\cos[\theta]$.

J. Summary

The rotated quartic solution due to the parabolic velocity and mass-source fields extends our previous analysis[34,38,39] on the numerical modeling of the Taylor dispersion problem. We confirm that the pure-diffusion grid-rotated solution can be matched exactly with the help of the fourth-order accurate Neumann and Dirichlet Taylor schemes using $\Lambda_0^{(ex)}(c_e)$ from Eq. (52), $\forall c_e$. When $\Lambda \neq \Lambda_0^{(ex)}$, the effective diffusion solution is isotropic only with the hydrodynamic mass-weight $t_q^{(m)}$, but it retains the symmetry. In contrast, the effective *advection-diffusion* solution is anisotropic and not symmetric with the hydrodynamic weights unless when it is tuned to be exact with the singular choice of the two remaining free parameters, as given by $\{\Lambda^{(ex)}, c_e{}^{(ex)}\}$ from Eq. (53). Using the fourth-order accurate Dirichlet closure, the effective solution is validated exactly with free-tunable values of these two parameters. In the Neumann system, $\Lambda^{(eff)}(c_e)$ from

Eq. (55) becomes mandatory for the exact solvability condition $\langle \mathscr{M}(\mathscr{U}^{(ex)}, y') \rangle = 0$; $\Lambda^{(eff)}(c_e)$ reduces to $\Lambda^{(ex)}$ when $c_e = c_e^{(ex)}$.

The exact bulk-parameter choice is employed to validate all proposed Dirichlet and Neumann schemes. We confirmed their second and, partly, third-order, convergence order in arbitrary-oriented, uniform and heterogeneous channels, and related their accuracy with the mass balance metrics. The interesting result is that the corrective flux Φ_0 is able to adjust the exact straight quartic solution for any flux scheme. Its analytical solution $|\Phi_0(\delta)|$ clearly indicates that the diffusive-flux DFLI family, which is built to be exact on the grid-rotated parabolic profiles in uniform tangential velocity field, deviates most significantly from the exact solvability condition on the quartic solution. This DFLI feature is then observed through all examined solutions, which undoubtedly explains its worst accuracy. In contrast, the FLI and FLI$_n$ behave most accurately despite their lower formal Taylor-accuracy order; this happens because their single-node flux continuation, as $-\Lambda^- \hat{n}_q^- + \delta \hat{n}_q^+$, fits the mid-grid LBM bulk-flux discretization in Eqs. (27). These suggestions are further confirmed through the exact mass-balance analysis in Sec. D.

Unfortunately, due to this semi-implicit discretization, FLI and FLI$_n$ may do not respect the additivity of a free constant in the Neumann or periodic solutions. All other schemes, including N-FLI, are consistent in our simulations. Also, the MR, but also N-MR and A-LSOB with the square-matrix reconstruction are all parametrized by grid Pe number and Λ; the rectangular reconstruction loses this property but it avoids the problem of the subset choice in Eq. (17), and hence it can be regarded as geometry- and problem-independent.

We recognize that the coarse grid solution may become spoiled by the truncation and its accommodation, growing very rapidly with Pe; the rectangular reconstruction becomes then not sufficiently accurate on the coarse grids. In this respect, when the tangential advective boundary flux is very small due to the no-slip velocity or a diffusive interface, the preselected candidates are the two-node FMR$_n$ and the one-node N-FLI, which show similar accuracy at the intermediate Pe range, e.g., Fig. 15. The FMR$_n$ converges faster, with third-order rate in the grid-aligned channels, it is simpler and more robust for the high Pe range. However, N-FMR or N-FLI should replace FMR$_n$ in the case of the (nearly) uniform rotated tangential flow and in the presence of the diffusive-flux jumps, as demonstrated for STRD, and as also expected for problems with the non-zero tangential diffusive boundary/interface flux.

Concerning the single-node A-LSOB flux schemes, the T-DFLI and T-DFLI$_r$ are interesting because they (i) share with FLI$_n$ the same (good) solvability condition in the straight grid-shifted systems, (ii) respect there, together with the unmodified MR, the weight-independence and linear Pe-scale, and (iii) show comparable to two-node FMR$_n$ conservation properties in the inclined channels. On the negative side, they are affected by strong truncation and accommodation errors through the reconstruction procedure at high Pe. The Taylor Dirichlet schemes T-PP and T-PP$_r$ are not impacted by Pe-dependent effects, and they even surpass the parabolic PP MR family (cf. Figs. 12 and 14, Table IV) because their normal Taylor condition is not affected by the advection projections. This is confirmed by the results of the degraded (linear) T-I-PP$_r$ scheme, which behaves much more accurately at high Pe than its linear MR counterparts, MPLI/LMKC, PLI and PPLI. In turn, the novel single-node parabolic PPLI from Table XII is the most accurate in the pure-diffusion and it approaches PP in the intermediate Pe range.

Finally, concerning the EMM − TRT application with the *no-slip velocity field*, we highlight that the parametrized schemes should be preferred to assure the solution control by the Péclet number at fixed Λ, and that the grid shall be refined approximately linearly when Pe grows to get rid of the nonphysical Pe-dependency due to the interface/boundary high-order accommodation. It should be said that the transient ADE solvers meet even stronger limitations for the Taylor moments prediction, because both the translation length and the computational time toward the steady Taylor regime grow with Pe. Moreover, whereas the transient ADE solvers become unstable with Pe, the steady-state EMM − TRT is not affected by the stability issue and the interface-conjugate MR steady-state treatment allows to accelerate the convergence by one or two orders with respect to their implicit tracking in rotated slabs.[40]

VI. ROTATED EXPONENTIAL SOLUTION IN PLUG FLOW

The two stratified heterogeneous layers of width $\{h_1, h_2\}$ are again arbitrary rotated and placed with respect to the grid, but now the constant (Darcy) advection velocity $\vec{u} = u_n \vec{1}_{y'}$ is perpendicular to the interface in "series." The system is periodic along y', it is abbreviated DS, and its modeled equation reads

$$u_n \partial_{y'} P_k(y') - \mathscr{M}_k = \mathscr{D}_k \partial^2_{y'} P_k(y'), \tag{65a}$$

$$\mathscr{M}_k := \mathscr{U}\phi_k - u_n, \langle \mathscr{M} \rangle = 0. \tag{65b}$$

Solvability condition $\langle \mathscr{M} \rangle = 0$ is adjusted with the mean-velocity $\mathscr{U}$. The interface conditions are described by Eq. (36): the scalar field is continuous ($\sigma^{(p)} = 1$, $\eta^{(p)} = 0$) but the normal diffusive-flux is subject to the jump condition: $\sigma^{(u)} = 1$, $\eta^{(m)} = ||\mathscr{D}_k|| \vec{1}_{y'} \cdot \vec{1}_n$. In theory, the advective flux is continuous on the interface and hence it vanishes from the flux closure relation. A continuous periodic solution $P(y')$ is defined up to an additive constant. Solution of Eq. (65) allows to predict the effective diffusivity (at zero velocity, thanks to the interface diffusive-flux jump) and the dispersion coefficient $D_T = \langle \phi \rangle^{-1} \langle u_n P \rangle$ in the plug flow due to the structure heterogeneity, the EMM also extends this procedure to the high-order moments.[37] The symbolic and numerical analysis of the EMM − TRT scheme is developed for the straight[38] (the diffusivity, dispersion, skewness and kurtosis) and the diagonal[39] (the second-order moments) implicit-jump tracking. These results (i) produce exact solutions for the three moments in the pure diffusion with the help of the specific dependency $\Lambda(c_e)$ for kurtosis (given by the third-order polynomial solution $P(y)$) and (ii) show that the implicit-interface ABB− continuity condition produces Pe-growing errors and an anisotropic interface location due to the presence of the advective term of $\beta^{(u)} = -\Lambda^+ \alpha^{(p)}$ in Eq. (5), as $-\Lambda^+ \hat{n}_q^+ \propto -t_q^{(a)} \Lambda^+ \partial_y u_n P(y) c^2_{qy}$ in the perpendicular flow $\vec{u} = u_n \vec{1}_y$. This term is vanished in PLI/PAB with the help of the post-collision correction $\hat{F}_q$ and, together with the next-order term of $\gamma^{(u)}$, in the parabolic MR PP family (see Table XIV). In the diagonal slab, both pure diffusion and plug flow are affected by the implicit interface accommodation.

In the present work, the "internal" $y' = 0$ and "periodic" $y' = h_2$ interfaces are modeled with the interface-conjugate from Eq. (37). When the proposed schemes are not exact on the discrete-exponential profile, we adjust their solvability condition with M_0 from Eq. (28) and the corrective interface jump $\pm\Phi_0$ from Eq. (64).

Our analysis undertakes a symbolic procedure in the straight geometry, and the numerical computations in the diagonal and rotated slabs.

A. Effective symbolic solutions

We construct and examine the effective solutions of the MR and A-LSOB interface-conjugate, and their combinations, in the straight interface-perpendicular plug flow. We also build the effective Taylor equivalents of the MR schemes and develop their inverse mapping, from the parabolic Taylor closure to its local MR equivalent.

1. Symbolic procedure

Our symbolic analysis follows[38] and develops with d2q5, because the steady-state profile $P(y)$ is weight-independent in the straight geometry; the extension for d2q9 solution and the diagonal orientation may follow.[39] We apply M_0 strategy, then Eq. (28) determines d2q5 solution for $\hat{n}_q^+(y_n)$:

$$\hat{n}_q^+(y_n) = t_q(\mathscr{M}_k(y_n) + M_0)c_{qy}^2, \tag{66a}$$

$$\text{then } \Delta_y \hat{n}_q^+ = 0,\ \Delta_y^2 \hat{n}_q^+ = 0,\ \forall\, y. \tag{66b}$$

Conversely, plugging Eq. (66) into Eqs. (15a)–(15c), $\hat{n}_q^{\pm}$ reads with $\mathrm{Pe}_k = \frac{u_n}{\mathscr{D}_k}$:

$$\hat{n}_q^+(y_n) = t_q c_e \Lambda_k^- \left[\mathrm{Pe}_k \Delta_y P c_{qy}^2 - \Delta_y^2 P c_{qy}^2\right](y_n), \tag{67a}$$

$$\hat{n}_q^-(y_n) = t_q c_e \left[\Delta_y P c_{qy} - \frac{1}{4}\mathrm{Pe}_k \Delta_y^2 P c_{qy}^3\right](y_n). \tag{67b}$$

Equation (28) equates the sums of Eqs. (67a) and (66a), and provides the central-difference form of the modeled equation:

$$u_n \Delta_y P - (\mathscr{M}_k + M_0) = \mathscr{D}_k \Delta_y^2 P,\ \mathscr{D}_k = c_e \Lambda_k^-. \tag{68}$$

Clearly, when $M_0 \neq 0$, the solution gradient gets modified as

$$P_k = a_k + b_k y + c_k r_k^{\,y}, \quad b_k = \frac{\mathscr{M}_k + M_0}{u_n}, \text{ with} \quad r_k = \frac{1 + \mathrm{Pe}_k/2}{1 - \mathrm{Pe}_k/2}. \tag{69}$$

The two-layered solution is determined up to an additive constant a_1 [or a_2]. The three coefficients from the set $\{a_1, a_2, c_1, c_2\}$ and M_0 are determined giving the two couples of the interface-conjugate conditions (37), e.g., with PP – FLI, PLI – FLI, and other MR combinations. The MR$_n$ and N-MR reduce to MR because the tangential advective-diffusive flux is zero in d2q5. Their interface-closure relations are all expressed exactly through Eqs. (66a) and (67b) plugging their Eq. (69). In turn, the A-LSOB Taylor schemes (12) become expressed through the four couples of the grid unknowns $\{\Delta_y P, \Delta_y^2 P\}|_{\vec{r}_i}^{(k)}$; T-PP is then substituted into the interface scalar equation (36a); T-DFLI (diffusive flux) or T-FLI (advective-diffusive flux) are substituted into the interface-flux equation (36b). Equation (67) closes the A-LSOB system by equating the RHS of Eq. (67) to its solution expressed on the profile (69) for vertical links in the interface grid nodes $\vec{r}_i$; this procedure mimics the reconstruction of $\{\Delta_y P, \Delta_y^2 P\}|_{\vec{r}_i}^{(k)}$ with the $\mathbf{B}[2\times 2]$ matrix in Eq. (17). We also combine the MR and A-LSOB interface-conjugate relations, as T-PP-FLI or PP – T-DFLI. Our symbolic procedure does not involve the truncation approximation from Eq. (16). The constructed solution then presents the effective numerical solution of a given scheme.

2. Solvability conditions

Assume that the "internal" $y' = 0$ and "periodic" $y' = h_2$ interfaces are shifted from their mid-grid position at the distance $\delta^{(i)}$ and $\delta^{(p)}$, respectively, giving $h_1 = H_1 + \delta^{(i)} - \delta^{(p)}$, $h_2 = H_2 + \delta^{(p)} - \delta^{(i)}$, but keeping the total length $h = h_1 + h_2 = H_1 + H_2 = H$. The following results are obtained on the symbolic solutions and confirmed numerically:

- Both FLI and FMR satisfy the exact solvability condition $\langle \mathscr{M}(\mathscr{U}^{(ex)})\rangle = 0$ with $M_0 = 0$:

$$M_0 = 0,\ \forall\, \{\delta^{(i)}, \delta^{(p)}\} \text{ if only } \mathscr{U} = \mathscr{U}^{(ex)} = \frac{u_n h}{\phi_1 h_1 + \phi_2 h_2}. \tag{70}$$

  This property is independent of the continuity scheme applied for a scalar-field in the interface-conjugate.
- Otherwise, when for example $\mathscr{U}$ is prescribed in Eq. (65b) via summation, FLI and FMR adjust M_0 according to the derivation in Subsection D 1 of the Appendix, as

$$M_0 = -\frac{(\mathscr{M}_1 - \mathscr{M}_2)(\delta^{(i)} - \delta^{(p)})}{H}, \text{ if } \mathscr{U} = \mathscr{U}^{(sum)} = \frac{u_n H}{\phi_1 H_1 + \phi_2 H_2}, \text{ then } M_0 = 0 \text{ if only } \delta^{(i)} = \delta^{(p)}. \tag{71}$$

  The case $\delta^{(i)} = \delta^{(p)}$ corresponds to the uniform vertical shift of the whole slab from its mid-grid position.
- Inversely, if one adjusts $c_e\Lambda^-$ and prescribes the same values $\mathscr{U}^{(ex)} = \mathscr{U}^{(sum)}$ at the fixed grid Péclet number $\mathrm{Pe}' = \frac{\mathscr{U}}{c_e\Lambda^-}$, then $\mathscr{M}_k(y') + M_0$, and hence $\hat{n}_q^+(y)$ in Eq. (66a), get identical solutions:

$$\mathscr{M}_k(y') + M_0 = \mathscr{U}^{(ex)}\phi_k - u_n(\mathscr{U}^{(ex)}). \tag{72}$$

  The proof is based on Eq. (71). However, $P(y')$ is distinguished in these two configurations, because $u_n(\mathscr{U}^{(ex)}) \neq u_n(\mathscr{U}^{(sum)})$.
- Unlike the FLI/FMR, the DFLI and T-DFLI produce $M_0 \neq 0$ either with $\mathscr{U}^{(ex)}$ or $\mathscr{U}^{(sum)}$ for any interface position, including its mid-way $[\delta^{(i)} = \delta^{(p)} = 0]$ or the uniformly-shifted $[\delta^{(i)} = \delta^{(p)}]$ placements. The DFLI solution of M_0 with $\mathscr{U}^{(sum)}$ is expressed in Eq. (D7). The symbolic solutions confirm it and show that, in contrast to Eq. (71), M_0 depends on the scalar-field continuity scheme $M_q^{(p)}$ applied in Eq. (37a), both with the DFLI and the Taylor scheme T-DFLI. That means that these two parabolic schemes do not satisfy the exact solvability condition in a series of straight blocks in the presence of the interface-normal velocity. Moreover, it is shown in Subsection D 2 of the Appendix that the vertical DFLI closure relation in Eq. (8) is equivalent with the back-sided non-equilibrium extrapolation of the diffusive-flux component $-\Lambda^-\hat{n}_q^-$, as

$$\mathrm{DFLI}: D_y(\vec{r} + \delta\vec{c}_q) = -\Lambda^-\hat{n}_q^-(\vec{r}) - \delta c_{qy}\Lambda^-(\hat{n}_q^-(\vec{r}) - \hat{n}_q^-(\vec{r} - \vec{c}_q)). \tag{73}$$

In contrast, T-DFLI in Eq. (12b) presents the locally expressed normal Taylor extrapolation of the diffusive flux.

- All these results are also valid in parallel Darcy flow $\vec{u} = u_\tau \vec{1}_{x'}$ [STRD]. However, since the STRD solution $P(y)$ to Eq. (41a)] is determined by $\mathscr{M}_k(\mathscr{U}) + M_0$, it is the same when $\mathscr{U}^{(ex)} = \mathscr{U}^{(sum)}$ but $u_\tau(\mathscr{U})$ and $c_e\Lambda^-$ differ. In these cases, the T-DFLI and DFLI are also exact, because Eqs. (12b) and (73) are exact when the diffusive flux is linear in space.

To sum up, when the mass-source is piece-wise constant, the DFLI "straight" closure relation is equivalent with the back-sided normal extrapolation of $-\Lambda^-\hat{n}_q^-$, whereas FLI and FMR operate its continuation locally via $\delta\hat{n}_q^+$, the BB alike, and they are then able to satisfy the exact solvability condition $\langle \mathscr{M}(\mathscr{U}^{(ex)})\rangle = 0$ with plug flow in series; this conservation property is unavailable with the DFLI and T-DFLI, even on the uniformly shifted interface $\delta^{(p)} = \delta^{(i)}$.

3. The exact Taylor MR form

We build now the Taylor equivalents of the MR schemes in the plug flow. This analysis is based on the exact central-difference solution in Eq. (67); the effective MR closure is then not identical with its second-order approximation in Eq. (5). This analysis allows us to compare the Taylor and MR closure relations in terms of the exact central-difference gradients $\Delta_y P$ and $\Delta_y^2 P$ according to Eq. (67). The key point is that the neighbor components $P(\vec{r}_b - \vec{c}_q)$ and $\hat{n}_q^-(\vec{r}_b - \vec{c}_q)$ in two-node MR schemes are expressed from Eqs. (26a) and (26b) through $P(\vec{r}_b)$ and $\hat{n}_q^\pm(\vec{r}_b)$, where we take into account that $\hat{n}_q^+$ is the same inside one layer thanks to Eq. (66). The MR Taylor form then reads as

$$T_n(\vec{r}_b) = t_1 M_0 + t_2 P + u_n c_{qy}(t_3 P + t_4 \Delta_y P c_{qy} + t_5 \Delta_y^2 P c_{qy}^2) + t_6 \Delta_y P c_{qy} + t_7 \Delta_y^2 P c_{qy}^2|_{\vec{r}_b}. \tag{74}$$

TABLE VI. The coefficients of the effective interface Taylor closure in Eq. (74) along the vertical cut link are derived from Eq. (34) [it is subdivided by $\alpha^{(p)} c_e t_q$ and reads with $\Lambda^- = \{\Lambda_k^-\}$]. Equation (74) with the MR and normal Taylor Dirichlet schemes in the straight geometry. The MR coefficients of Eq. (34) are subdivided by $\alpha^{(p)} c_e t_q$.

Taylor form of the Dirichlet MR				
	MR			normal Taylor
t_i	MPLI	PLI	PP/KMR1	T-PP
t_1	$(I_{int}-1)\dfrac{\Lambda}{\Lambda^-}$	0	0	0
t_2	1	1	1	0
t_3	0	0	0	1
t_4	$-\dfrac{(1+(I_{int}-1)c_e)\Lambda}{c_e\Lambda^-}$	0	0	0
t_5	$-\dfrac{\delta}{4c_e\Lambda^-}$	$-\dfrac{\delta}{4c_e\Lambda^-}$	$-\dfrac{\delta(1+\delta)}{4c_e\Lambda^-}$	0
t_6	$\dfrac{1}{2}$	δ	δ	δ
t_7	$(1+(I_{int}-1)c_e)\Lambda$	0	$\dfrac{\delta^2}{2}$	$\dfrac{\delta^2}{2}$

TABLE VII. Equation (74) with the MR and normal Taylor flux schemes in the straight geometry. The coefficients of Eq. (34) are subdivided by $t_q\alpha^{(u)}$ in FLI/FMR and $t_q^{(m)}\beta'$ in DFLI.

t_i	FLI/FMR	T-FLI	DFLI	T-DFLI
t_1	0	0	0	0
t_2	0	0	0	0
t_3	1	1	0	0
t_4	δ	δ	0	0
t_5	$\dfrac{1}{4}$	$\dfrac{1}{2}\delta^2$	$\dfrac{1}{4}(1+2\delta)$	0
t_6	$-c_e\Lambda^-$	$-c_e\Lambda^-$	$-c_e\Lambda^-$	$-c_e\Lambda^-$
t_7	$-c_e\Lambda^-\delta$	$-c_e\Lambda^-\delta$	$-c_e\Lambda^-\delta$	$-c_e\Lambda^-\delta$

Tables VI and VII give, respectively, the coefficients for the Dirichlet and Neumann, MR and A-LSOB basic schemes. They remain valid for the pure diffusion and in straight parallel flow giving $u_n = 0$ in Eq. (74). We first note that according to these two tables, all MR schemes are incorrect for the term of $t_5 u_n \Delta_y^2 P$. In detail, the effective diffusive-flux interface condition reads as

$$\text{T-DFLI}: \ ||-\Lambda_k^- c_e c_{qy}(\Delta_y P_k + \delta\Delta_y^2 P_k c_{qy})|| = ||\mathscr{D}_k||, \tag{75a}$$

$$\text{DFLI}: \ ||-\Lambda_k^- c_e c_{qy}(\Delta_y P_k + \delta\Delta_y^2 P_k c_{qy})|| = ||\mathscr{D}_k|| - \frac{u_n}{4}||(1+2\delta)\Delta_y^2 P_k)||. \tag{75b}$$

Thus, DFLI modifies the prescribed jump condition with respect to T-DFLI in the normal flow, to be contrasted with the second-order approximation in Eq. (5), which vanishes all velocity terms in DFLI closure thanks to its coefficients, $\alpha^{(u)} = \beta^{(u)} = \gamma^{(u)} = 0$. In turn, the PP/KMR1 − FLI/FMR interface-conjugate reads with

$$\text{PP/KMR1}: ||P + \delta\Delta_y P c_{qy} + \frac{\delta^2}{2}\Delta_y^2 P c_{qy}^2|| = \left|\left|\frac{\delta(1+\delta)\mathrm{Pe}_k}{4}\Delta_y^2 P\right|\right|. \tag{76a}$$

$$\text{FLI/FMR}: \ ||u_n c_{qy}\left(P + \delta\Delta_y P c_{qy} + \frac{1}{4}\Delta_y^2 P c_{qy}^2\right) - c_e\Lambda_k^- c_{qy}(\Delta_y P + \delta\Delta_y^2 P c_{qy})|| = ||\mathscr{D}_k||. \tag{76b}$$

These results show first that the parabolic schemes PP and KMR1 are equivalent on the straight interface, and they both modify the Taylor continuity relation in the *interface-normal flow* $\mathrm{Pe}_k \neq 0$; again, this is despite that the PP closure in Eq. (5) is predicted to be velocity-independent. Second, FLI and FMR produce identical closure relations and hence, the same solutions in the basic straight configurations, although their form in Eq. (5) is distinct for the coefficient of $\gamma^{(u)}$. Namely, their common deficient advection term $\frac{1}{4}\Delta_y^2 P c_{qy}^2$ in Eq. (76b) is $\delta-$independent and hence, it is the same as with the BB or implicit-interface tracking. Hence, Eq. (76b) comes down to T-DFLI from Eq. (75a) only provided that the scalar interface-continuity condition in Eq. (37a) is modeled with the incorrect, *modified* Taylor scheme, replacing $\frac{1}{2}$ by $\frac{1}{4}$ in the parabolic term:

$$\text{M-T-PP}: \left|\left|\left(P + \delta\Delta_y P c_{qy} + \frac{1}{4}\Delta_y^2 P c_{qy}^2\right)\right|\right| = 0. \tag{77}$$

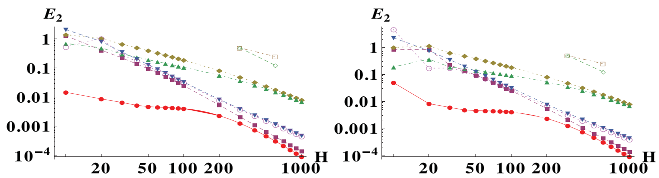

FIG. 23. The Darcy in series system [DS] in two equal straight blocks when the "internal" and "periodic" interfaces are shifted at $\delta^{(i)}$ and $\delta^{(p)}$, respectively, from the mid-grid position. PP − FLI/FMR ● and T-PP − FLI/FMR■ with $M_0 = \Phi_0 = 0$, then M_0 − PP-DFLI ▲, Φ_0 − PP − DFLI ◆ and M_0 − T-PP − T-DFLI ▼, Φ_0 −T-PP − T-DFLI ◯. Left: $\delta^{(i)} = \delta^{(p)} = \frac{1}{4}$, E_2- rate $r = \{2.37, 2.23, 1.56, 1.47, 1.77, 1.77\}$. Right: $\delta^{(i)} = -\delta^{(p)} = -\frac{1}{4}$, E_2- rate $r = \{2.37, 2.23, 1.55, 1.45, 1.75, 1.74\}$. Data: $\mathrm{Pe} = 10^2$, $r_\phi = 8$.

To sum up, the second-order "correct" Taylor interface-conjugate T-PP − T-DFLI produces $M_0 \neq 0$ according to above analysis, and hence it does not support the exact solvability condition, whereas the "incorrect" interface-conjugate M-T-PP − T-DFLI respects $\langle \mathscr{M}(\mathscr{U}^{(ex)})\rangle = 0$ thanks to its equivalence with M-T-PP −FLI/FMR. This example clearly shows that the best mass-balance and the best Taylor accuracy are not equivalent for LBM flux schemes.

4. The M_0 and Φ_0 in plug flow

Let us exemplify the symbolic solutions for several basic interface combinations, like PP − FLI, PP − DFLI and T-PP − T-DFLI, where we now compare the two strategies, M_0 from Eq. (28) and the corrective interface-jump Φ_0 from Eq. (64). Figure 23 displays E_2 when the interface is shifted uniformly (left diagram) and when the "internal" and "periodic" interfaces move one to another; on the whole, we observe that these two "opposite" configurations produce very similar results. In accord with the above analysis, PP-FLI and PP-FMR produce identical and the most accurate results; they solve the system with $M_0 = 0$ and $\Phi_0 = 0$. Otherwise, with both DFLI and T-DFLI, the effective solution $|M_0|$ and $|\Phi_0|$ depends on the scalar-continuity scheme. It is confirmed that M_0 − PP − DFLI is the least accurate, and it is surpassed by the Φ_0 − PP − DFLI over a long interval $H \leq\approx 3 \times 10^2$; the two techniques then decay together on the finer grids. In turn, T-PP − T-DFLI behaves similar to PP − DFLI on the coarsest grids, where it is not accurate; however, T-PP − T-DFLI converges faster and decays almost in parallel with PP − FLI/FMR, both with M_0 and Φ_0. The "mixed" single-node pair T-PP-FLI is also interesting: it behaves as the T-PP − T-DFLI on the coarse grid, but then very rapidly (with a rate about 2.4) joins PP-FLI. These observations confirm that the mass conservation, or the exact solvability, predetermines the *asymptotic accuracy*, whereas the joined combination of the two interface conditions determines it on the realistic grids.

B. Inverse mapping in the straight system

A very interesting property of the examined above effective closure relations and their solutions is that they are $\Lambda-$ independent. This property is not automatic, for example E_2 linearly grows with Λ using the implicit ABB − BB interface-tracking,[38,40] where ABB differently shifts the midway interface position on two interface sides to $\frac{1}{2} \mp \Lambda_k^-(1 - c_e)\mathrm{Pe}_k$. The PAB scheme [which is $\mathrm{PLI}(\delta = \frac{1}{2})$] radically improves for this property with the leading-order post-collision advection correction, and makes the solution $\Lambda-$ independent; the parabolic PP and T-PP schemes examined above share the same property in the straight series. However, we have seen that the MR and Taylor schemes are not equivalent there. The idea of the "inverse mapping" is to construct the I-MR equivalents of the Taylor schemes. The I-MR is searched in its steady-state one-node form in Eq. (34):

$$M_q(\vec{r}_b) = (m_1 e_q^+ + m_2 e_q^- + m_3 \hat{n}_q^+ + m_4 \hat{n}_q^-)|_{\vec{r}_b}. \tag{78}$$

Equations (66a) and (67b) are substituted into Eq. (78) for $\hat{n}_q^\pm$; $M_q(\vec{r}_b)$ then becomes expressed through the local variables $\{M_0, P, \Delta_y P, \Delta_y^2 P\}|_{\vec{r}_b}$. The four coefficients m_i are then adjusted to one of the three Taylor schemes (12); the obtained coefficients are gathered in Table VIII for their three (inverse) equivalents: I-PP, I-FLI and I-DFLI. Usually, the MR coefficients only depend upon the directional distance δ to the interface/boundary. However, the I-MR coefficients also depend on (a) the sign of (cut) link c_{qy}, and (b), grid Péclet number Pe_k. Hence, the inverse mapping automatically detects the anisotropy and Péclet–dependency of the effective closure. We have verified that the I-MR numerical solution coincides with the symbolic solution of its Taylor counterpart. Hence, the single-node I-MR reproduces the A-LSOB in straight series without any reconstruction. At zero Pe, the local I-MR reduces to Table IX and it applies exactly on the vertical cut link for piece-wise parabolic straight profile [STRD problem above].

To sum up, the I-MR delivers the methodological example on how one should combine equilibrium and non-equilibrium components in single interface-neighbor nodes to make the interface-

TABLE VIII. The coefficients $m_1 - m_4$ of the "inverse" single-node I-MR in Eq. (78), equivalent with the Taylor schemes from Eq. (12) in straight plug flow in series. The table reads with $X = 2c_{qy} + \mathrm{Pe}_k$, $Y = -4 + \mathrm{Pe}_k^2$, $Z = -2 + \delta^2\mathrm{Pe}_k^2$, $\mathrm{Pe}_k = \frac{U_0}{\mathscr{D}_k}$, $\delta = \delta_k$ in phase k and c_{qy} corresponds to interface cut link $\vec{c}_q$. The I-PP applies flag $l_{int} = 1$ in interface-conjugate in Eq. (37a).

I-MR = A-LSOB	m_1	m_3	m_2	m_4
I-PP = T-PP	1	$\frac{\delta(2(1+\delta)\mathrm{Pe}_k + c_{qy}(4\delta + \mathrm{Pe}_k^2))}{\Lambda_k^- XY}$	0	$\frac{-2\delta(2 + c_{qy}\mathrm{Pe}_k)(2c_{qy} + \delta\mathrm{Pe}_k)}{XY}$
I-FLI = T-FLI	0	$\frac{c_{qy}((-1+2\delta^2)\mathrm{Pe}_k + c_{qy}\delta Y)}{Y}$	1	$\frac{-2c_{qy}\Lambda_k^-(2 + c_{qy}\mathrm{Pe}_k)Z}{XY}$
I-DFLI = T-DFLI	0	$\frac{-2(1+2\delta\mathrm{Pe}_k) + c_{qy}(8\delta + \mathrm{Pe}_k^2)}{XY}$	0	$\frac{4c_{qy}\Lambda_k^-(2 + c_{qy}\mathrm{Pe}_k)(1 + c_{qy}\delta\mathrm{Pe}_k)}{XY}$

TABLE IX. The results of Table VIII when $\mathrm{Pe}_k \to 0$. These local I-MR d2q5 schemes are exact on the straight parabolic profile according to Eq. (43).

I-MR = Taylor	m_1	m_2	m_3	m_4
I-PP = T-PP	1	0	$-\frac{\delta^2}{2\Lambda_k^-}$	δ
I-FLI = T-FLI	0	1	δ	$-\Lambda_k^-$
I-DFLI = T-DFLI	0	0	δ	$-\Lambda_k^-$

conjugate in Eq. (36) equivalent with the Taylor interface closure from Eq. (12) on the straight interface in series. This approach may find its utility for construction of the MR schemes.

Remark. In principle, giving $m_1 - m_4$ in Eq. (78), one can try to invert the system (35) and to find the corresponding coefficients $\{\hat{\alpha}, \beta, \hat{\beta}, \gamma, \hat{\gamma}, \hat{K}^{\pm}\}$ in the standard (transient) MR, Eq. (A1). When $\mathrm{Pe}_k \neq 0$, the obtained coefficients depend upon c_{qy}. For example, the I-PP and I-FLI can be, respectively, reproduced by the ABB and BB supplemented with two local specific post-collision corrections $\hat{K}^{\pm}$.

C. Diagonal interface

The symbolic and numerical results[39] show that the d2q5 tackles the implicit diagonal mid-way interface without accommodation layers and retains the second-order convergence in series of two heterogeneous blocks. In contrast, the full weight-stencil d2q9 model suffers from the equilibrium discrete-exponential A-layer accommodation; its amplitude depends on the weight distribution, Λ, Pe and porosity contrast. The error estimates[39] address the two solution functionals, like the effective diffusivity and the Taylor dispersion coefficient D_T; the A-layer slows their error convergence to the first order (see Fig. 10 in Ref. 39) We extend this analysis to the grid-shifted interface-conjugate treatment and employ the standard error-estimate metric.

Our steady-state simulations are performed in a single column delimited by the diagonal periodic interface. The PP is prescribed for the scalar-continuity in Eq. (37a); in flux schemes, $\mathrm{MR} = \mathrm{MR}_n$ because the mass-source is piece-wise constant. In theory, there are no tangential effects because the 1d advection-diffusion process develops along the interface-normal direction; however, the numerical solution may produce spurious accommodation terms. We then examine not only the d2q5 and d2q9, FLI and FMR for flux-jump in Eq. (37b), but also their d2q9 N-MR counterparts from Table III. We find that the reconstructions based on the two coordinate and one diagonal tangential link $q = 3$, like N-FLI$_1$ or its "RM" counterpart with $\mathbf{B}[6 \times 5]$ in Eq. (17), produce a zero value for $\partial_\tau P$, $\partial^2_{\tau n} P$ and $\partial^2_{\tau\tau} P$ in Eq. (11), and hence, they do not modify MR in Eq. (10). In contrast, N-FLI$_2$ and N-FMR$_r$ involve the interface-perpendicular diagonal link and formally produce non-zero projection $\partial^2_{\tau\tau} P \neq 0$ in Eq. (10) due to the full-stencil accommodation. Figure 24 then addresses d2q9 (with the hydrodynamic weights) and d2q5 in the presence of the grid-shifted diagonal interface, using the FLI$-$ based (left diagram) and FMR$-$ based (right diagram) flux conditions. It is observed that d2q5 $-$ FLI and d2q5 $-$ FMR overlap, the straight d2q5/d2q9 system alike. Moreover, d2q5 retains the exact mass-conservation and it solves the global system with $M_0 = \Phi_0 = 0$; the d2q5 then remains the most accurate and it converges the fastest, with rate $r \approx 1.7$. Among the d2q9 schemes, N-FLI$_2$ reaches the best accuracy and convergence

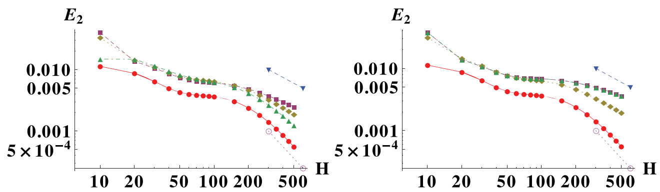

FIG. 24. The DS in the diagonal grid-shifted series of two porous blocks applying the PP for scalar-field continuity in Eq. (37a) and Φ_0 from Eq. (64) for solvability. Left: d2q9 with FLI■, N-FLI$_r$◆, N-FLI$_2$▲; $r = \{7.66 \times 10^{-1}, 1.04, 1.41\}$. Right: d2q9 with FMR■, N-FMR$_r$◆, N-FMR$_2$ ▲; $r = \{5.7 \times 10^{-1}, 1., 5.71 \times 10^{-1}\}$. Left & Right: d2q5 $-$ FLI = d2q5 $-$ FMR ●, $r = 1.71$, H^{-1} ▼, H^{-2}○ Data: $\theta = \frac{\pi}{4}$, $(x_0, y_0) = (\frac{1}{4}, \frac{1}{8})$, $\mathrm{Pe} = 10^2$, $r_\phi = \frac{1}{8}$, $\Lambda = \frac{1}{4}$, $c_e = \frac{1}{3} \times 10^{-1}$, d2q9$(t_c^{(.)} = \frac{1}{3}, t_d^{(.)} = \frac{1}{12})$.

with $r \approx 1.4$, followed by the linearly decaying N-FMR$_r$, whereas FLI and FMR without corrections decay slower. These results allow to suggest that the N-MR is able to diminish the interface-accommodation through its tangential projection, and then to improve the whole solution, asymptotically at least.

D. Rotated series of porous blocks

The rotated system of two heterogeneous blocks in series has been examined[40] with the MR interface-conjugate schemes (see there Fig. 14). When $\mathrm{Pe} = 10$, the FLI and FMR, combined with PP in Eq. (37a), converge with rate $r \approx 1.8$, and they clearly overpass their combinations with the linear scalar-continuity schemes, like PLI and MPLI, which demonstrate the expected linear decay. These computations are run with $M_0 \neq 0$ in Eq. (28). It has been observed that the advection accommodation effect rapidly amplifies between $\mathrm{Pe} = 10$ and $\mathrm{Pe} = 10^2$: the solution dependency over the equilibrium weights then becomes highly irregular, and the convergence rate becomes halved, both for E_2 and M_0. Moreover, d2q5 loses its advanced accuracy, which is observed in the grid-aligned and, for small Pe range, rotated systems. At the same time, the BB flux condition, combined either with the implicit interface scalar-continuity condition (ABB), linear or parabolic Dirichlet schemes, retains its first-order convergence when $\mathrm{Pe} = 10^2$, and then ABB-BB even slightly supersedes the formally most accurate PP-FMR interface-conjugate on the finest grids $H \geq 3 \times 10^3$. In agreement with our conclusions above with respect to FLI/FMR straight system, this advanced BB performance might be related to its mass-conservation $[M_0 = 0]$ because the solvability condition[40] is prescribed via summation, as $\langle \mathcal{M}(\mathcal{U}^{(sum)}) \rangle = 0$.

We apply here the exact condition $\langle \mathcal{M}(\mathcal{U}^{(ex)}) \rangle = 0$, which is equivalent to the summation in constant velocity field when the discrete phase distribution respects the porosity ratio r_ϕ exactly. Figure 25 presents in the left diagram the error decay in the same geometry considered previously, but using the two solvability strategies, M_0 and Φ_0.

The corrective interface flux-jump Φ_0 shows slightly better accuracy in all simulations, and slightly better convergence rate (DFLI excepted); $\Phi_0 - \mathrm{PP} - \mathrm{FLI}$ is again the most accurate. The PP $-$ DFLI remains one-order magnitude less accurate than its FLI and FMR counterparts, but it converges slightly faster. The two linear schemes $M_0 - \mathrm{PLI} - \mathrm{FLI}$ and $\Phi_0 - \mathrm{PLI} - \mathrm{FLI}$ halve the PP convergence rate.

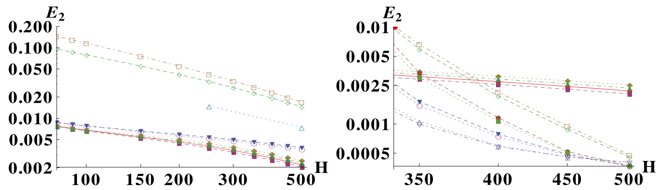

FIG. 25. The DS in the inclined series of two porous blocks. Left: PP− contnuity scheme is combined with M_0- FLI●, Φ_0- FLI■, M_0- FMR ◆, Φ_0- FMR ▲: $r=10^{-1}\times\{8.7,8.9,8.1,8.3\}$, followed by PLI− conitinuity combined with, M_0- FLI ▼ and Φ_0- FLI ◯, $r=\{0.49,0.5\}$; and then by (the least accurate) M_0- PP − DFLI □ and Φ_0- PP − DFLI ◇: $r=\{1.3,1.2\}$. Right: The PP is combined with M_0- FLI●, Φ_0- FLI■, M_0- FMR◆, Φ_0- FMR▲ ("lines") and their four counterparts N-FLI$_r$, N-FLI$_3$, N-FMR$_r$, N-FMR$_3$ ("curved", from the "bottom"), their results are plotted together with M_0 and Φ_0. Data: $\theta=\arctan[\frac{1}{2}]$, $(x_0,y_0)=(\frac{1}{4},0)$, Pe $=10^2$, $r_\phi=\frac{1}{8}$, $\Lambda=\frac{1}{4}$, $c_e=\frac{1}{3}\times 10^{-1}$, d2q9 ($t_c^{(\cdot)}=\frac{1}{3}$, $t_d^{(\cdot)}=\frac{1}{12}$).

Figure 25 (right diagram) then compares PP-FLI and PP-FMR with their N-MR partners on the finest grids. In fact, we observed that N-MR is rather irregular on the coarser grids, most likely because of the strong interface-accommodation advection effect. We optionally apply (i) the reduced rectangular reconstruction N-FLI$_r$/N-FMR$_r$ with $\mathbf{B}[6\times 5]$ in Eq. (20), giving four coordinate values $\hat{n}^{\pm}_{1,2}$ and two diagonal values $\hat{n}^{\pm}_3$ in the RHS of Eq. (10), and (ii), the corresponding square reconstruction N-FLI$_3$ and N-FMR$_3$ with Eq. (17), reducing $\hat{n}^{\pm}_3$ to $\hat{n}^{+}_3$. The N-MR is also performed with M_0 and Φ_0; we observe that, as usual, $E_2(M_0)$ is slightly higher than $E_2(\Phi_0)$. Asymptotically, the four N-MR schemes diminish the error-estimate of their FLI/FMR counterparts and all converge toward the same solution.

To sum up, these preliminary results indicate that the current N-MR procedure is able to reduce a strong purely-accommodation solution component in the interface-perpendicular diagonal and rotated plug flow, but only on the very fine grids.

VII. CONCLUDING REMARKS

We proposed two new boundary approaches, suitable for both transient and steady-state linear ADE−LBM: A-LSOB and N-MR, and validated them with the stationary S-TRT formulation in arbitrary-oriented channel slabs. The A-LSOB is a single-node approach: in a transient standard algorithm, the incoming populations are built with the third-order accurate Chapman-Enskog expansion, where all first- and second-order derivatives are expressed from the post-collision non-equilibrium alone, and they are constrained to the wall-normal parabolic-accurate Taylor approximation of the Dirichlet or Neumann boundary condition. The nodal reconstruction requires the d2q9 stencil to restore all five 2D derivatives without resort to any surface information; this step can be accomplished either with a square- or rectangular-matrix formulation; the latter makes the A-LSOB algorithmically simpler, lattice- and problem-independent, but it does not retain the S-TRT parametrization by Péclet number and Λ in the general cases. Another subtle point is that the S-TRT operates with the symmetric and anti-symmetric non-equilibrium components, rather than with the populations, and any one of them suffices to be prescribed for a wall-cut link; we proposed a heuristic algorithm to build the well-defined local and global linear systems.

The (normal) N-MR follows another path to prescribe the parabolic-accurate Neumann condition. The N-MR restores locally, but precisely, the actual directional projection of the tangential advective-diffusive flux, built-in into a given MR flux closure relation, and simply deducts it from the incoming-population solution. Also, the in-node correction of the normal mass-source variation improved accuracy of the MR$_n$ and N-MR flux schemes for all reported results. In this work, the A-LSOB and N-MR shared the same reconstruction procedure, delivering the same results in the Cartesian and flat-surface aligned coordinates. The N-MR extension to 2d/3d curved boundaries and corner geometries with a non-zero boundary flux value is thought to be more efficient in the fixed coordinate system, because the normal direction is distinct for different cut-links. This next step might adapt the recent LSOB formulation[87] for the curved cross-section duct Stokes flow.

In the presence of a grid-rotated high Pe velocity field, the single-node parabolic Dirichlet A-LSOB T-PP shows better accuracy level than the two-node parabolic MR PP; in turn, a linear normal Taylor condition behaved more accurately than its single-node MR counterparts MPLI/PLI/PPLI. This Dirichlet A-LSOB enhancement is because the MR directional closure relations are affected by the advection projections, e.g., at the first order with MPLI/PPLI, the second order with PLI and the third-order with PP; however, the A-LSOB reconstruction process is not smooth at high Pe. The MR, N-MR and A-LSOB expand straightforwardly for the Robin condition by combining their Dirichlet and normal Neumann counterparts. The A-LSOB is expected to extend easier its parabolic accuracy to the full-matrix and anisotropic collisions, but, like the MR, the N-MR operates directly on any-shape interface-conjugate and it applies very similarly in transient and steady-state algorithms. The two methods follow the so-called Lnode approach[87] whereas the ideas of the "Lwall" approaches[21,23,104,105] might become beneficial for (i) their reduction to the coordinate stencils, thanks to additional surface information, and (ii) their interface extensions, by re-formulating A-LSOB and N-MR in terms of the surface derivatives. Finally, the reconstruction procedure was elaborated for the linear ADE; we assume that the transient non-linear problems might adapt the linearization of the Chapman-Enskog solution around the previous step.

We have shown that the BB, its linear [FLI] and parabolic [FMR] advective-diffusive MR flux counterparts should be corrected in the steady-state problems in the presence of the grid-rotated tangential constant velocity field. The previous research delivered similar conclusions in the wall-parallel transient advection[26] and for the non-zero tangential diffusive boundary flux;[17,42,62–64] indeed, the accommodation mechanism is equivalent for tangential, constant-velocity and linear diffusive, fluxes.[33,36,39] The N-MR and Neumann A-LSOB are constructed to resolve these two problems together, for any velocity field; their formulation is equivalent for advective and diffusive flux components, and their concept was validated through the exactness of their piece-wise parabolic, bounded, periodic, continuous and discontinuous, profiles in the grid-inclined uniform velocity field, extending this solution class for the single-node Dirichlet and Neumann A-LSOB schemes, and the single-node N-FLI scheme. We note that the N-FLI improves the FLI scheme[62] for any weight-stencil without need for resorting to the heuristic Dirichlet and off-grid interpolations. Conversely, we have demonstrated that the linearly accurate Dirichlet LI families, and the intentionally degraded A-LSOB Dirichlet and

Neumann schemes, fail to reproduce interface and boundary behavior correctly in the benchmark configurations tested herein.

All parabolic-accurate schemes behaved well on the quartic profiles in the diffusion-dominant refimes and intermediate Pe-range, suggesting them to be suitable for heat and mass transfer applications in composite materials. In particular, the most simple single-node Dirichlet PPLI shows the best diffusion accuracy; its Dirichlet velocity counterpart IPLI is expected to share these properties in the pipe fluid flow modeling; their further validation is required because of the restricted heuristic stability range. Some reservations should be made for the advection-dominant regime. In practice, both the Cartesian-decomposition method[62] and N-MR considerably complicate the simple directional MR concept; it is legitimate to understand when they are necessary for the realistic solute transport. We have shown that the tangential grid-inclined *no-slip velocity field* induces relatively small boundary and open-porous diffusive-interface errors, as compared to the truncation and its accommodation effects caused by the inexactness of the boundary rules. The latter was demonstrated on the quartic-polynomial rotated solution, where the second-order boundary schemes excite the anisotropic advection truncation, which non-linearly grows with Péclet number, violates the linear Pe-scale of the modeled equation and makes the error-estimates Pe-dependent. A similar deficiency is provoked by the accommodation layers in the grid-inclined interface-perpendicular plug flow, rendering the N-MR solutions irregular in the high Péclet regime. Given that the diffusive-flux effects must become negligible when the advection is strong, we suggest to give the preference to the unmodified MR schemes, and in particular, the two-node FMR/FMR$_n$, for the interface-continuous Neumann problems in the high Pe problems. The N-MR or A-LSOB may substitute it there for the discontinuous solutions with the diffusive-flux jumps.

We also examined all flux schemes with respect to the exact, "body-fitted", mass-conservation solvability condition $\langle \mathscr{M} \rangle = 0$ using either the (i) artificial uniform mass-source M_0, suitable in any geometry or (ii) corrective surface-flux $\pm\Phi_0$, applicable on two parallel surfaces; these unknown variables are automatically obtained on the global S-TRT solution. Their respective amplitudes $|M_0|$ and $|\Phi_0|$ served us as mass-balance metrics. Although the two techniques decay closely with second-order rate, the corrective flux is more accurate, especially with MR, because it does not modify the bulk equation. As one illustrative example, the corrective flux is able to adjust the grid-shifted symmetric straight quartic solution for all examined flux schemes, including the BB. We hope that these findings will inspire novel approaches for the mass-balance of the body-fitted regular-grid boundary schemes.

Along these lines, our results undoubtedly show that the inherent mass-balance dominates the formal accuracy with the Neumann LBM. In particular, the FLI/FLI$_n$ exhibits the smallest mass leakage and, together with the FMR/FMR$_n$, assures the exact mass-balance for any straight interface position in the plug flow. This happens because FLI describes the total local mass-flux as $-\Lambda^- n_q$, and its continuation toward the delimiting surface as $\delta \hat{n}_q^+$, which comes down to the regular bulk-flux discretization for $\delta = \frac{1}{2}$. However, due to this semi-implicit discretization, FLI/FLI$_n$ does not guarantee to respect a free additive constant in the Neumann solutions, in the presence of the parabolic tangential velocity field at least. This truncation feature is in-line with the deficient local-gradient estimate dependency upon an additive constant,.[39] On the positive side, all other examined flux schemes, as the FMR, DFLI, N-MR and Taylor scheme T-DFLI, are consistent with respect to additive constant independence in our examples. The FMR, N-MR and T-DFLI report a comparable mass-balance in the grid-inclined situations, but the example of the parabolic diffusive-flux MR scheme DFLI shows that its intrinsic back-sided extrapolation of $-\Lambda^- n_q$ along the characteristic is extremely non-conserving, except the linear diffusive-flux case where it is exact. These observations might become fruitful for many non-equilibrium interpolation approaches.

Concerning the presented analytical work, we (i) derived the solvability conditions on the equilibrium weights or free TRT parameter Λ, when the quartic polynomial may satisfy the discrete system in the presence of the grid-rotated parabolic advection profile, (ii) constructed the associated effective solution with the hydrodynamic weights, (iii) delineated the particular dependency $\Lambda(c_e)$ where the effective solution becomes exact and hence, isotropic and linearly scaling with Pe, and (iv) built the corrective boundary flux which adjusts the global mass conservation for all examined flux schemes. We also constructed the effective symbolic solutions in the interface-perpendicular straight plug flow and applied them to compare exactly all schemes for their mass balance; the FLI and FMR are found to be conservative on the grid-shifted straight interface. Finally, we built the single-node MR counterparts of the Taylor schemes and demonstrated that, unlike in the current MR approach, their coefficients should become anisotropic and account for the cut link direction with respect to the surface-perpendicular plug velocity field. We believe that our methodology will be helpful to advance the LBM analysis and to delineate the most optimal closure schemes.

In conclusion, the Neumann boundary and interface-flux conditions should combine the compactness, accurate mass-balance, physical parametrization, correct Pe-scale and free-constant independence with the release of the tangential constraints and efficient reduction of the accommodation layers. We have shown that the proposed approaches progress along all these directions, and we expect that they will bring some new ideas for two-phase and fluid-solid, stress and slip Lattice Boltzmann models.

APPENDIX A: THE LI AND MR MULTI-REFLECTION SCHEMES

We consider the MR in two-node directional form:

$$\begin{aligned} f_{-q}(\vec{r}_{\rm b}, t+1) &= {\rm MR}_q(\vec{r}_{\rm b}, t) + w_q(\vec{r}_q, \tilde{t}),\ \vec{r}_q = \vec{r}_{\rm b} + \vec{c}_q \notin V_p, \\ {\rm MR}_q &= \hat{\alpha}\hat{f}_q(\vec{r}_{\rm b}, t) + \beta f_q(\vec{r}_{\rm b}, t+1) + \hat{\beta}\hat{f}_{-q}(\vec{r}_{\rm b}, t) \\ &\quad + \gamma f_q(\vec{r}_{\rm b} - \vec{c}_q, t+1) + \hat{\gamma}\hat{f}_{-q}(\vec{r}_{\rm b} - \vec{c}_q, t) \\ &\quad + \hat{F}_q(\vec{r}_{\rm b}, t),\ \hat{F}_q = \hat{K}^+ \hat{n}_q^+ + \hat{K}^- \hat{n}_q^-. \end{aligned} \tag{A1}$$

Equation (A1) gives solution for unknown population $f_{-q}(\vec{r}_{\rm b}, t+1)$ in boundary node $\vec{r}_{\rm b}$ in terms of (i) three post-collision populations: $\hat{f}_q(\vec{r}_{\rm b}, t), \hat{f}_{-q}(\vec{r}_{\rm b}, t), \hat{f}_{-q}(\vec{r}_{\rm b} - \vec{c}_q, t)$; (ii) two after-streaming populations: $f_q(\vec{r}_{\rm b}, t+1) = \hat{f}_q(\vec{r}_{\rm b} - \vec{c}_q, t)$ and $f_q(\vec{r}_{\rm b} - \vec{c}_q, t+1) = \hat{f}_q(\vec{r}_{\rm b} - 2\vec{c}_q, t)$; (iii) local post-collision correction $\hat{F}_q(\vec{r}_{\rm b}, t)$ and (iv), the prescribed boundary term $w_q(\vec{r}_q, \tilde{t})$. Alternatively, one may adopt the time-explicit algorithm by replacing $\beta f_q(\vec{r}_{\rm b}, t+1)$ and $\gamma f_q(\vec{r}_{\rm b}, t+1)$ by their previous time step solution: $\beta f_q(\vec{r}_{\rm b}, t)$ and

TABLE X. The three-population families MPLI($\alpha^{(p)}$) and PLI($\alpha^{(p)}$) with free coefficient $\alpha^{(p)}$ and $\gamma = \hat{\gamma} = 0$; w_q obeys Eq. (A4); the two schemes differ for $\hat{K}^+$; β or $\hat{K}^+$ can be set equal to zero with the specific $\alpha^{(p)}$. Heuristic stability: $\{\hat{\alpha}, \beta, \hat{\beta}\} \in [-1, 1]$ when $\alpha^{(p)} \in [-\frac{4}{3}, 0[, \forall\delta$. The coefficients of the three Dirichlet families[62] are matched with $\alpha^{(p)} = \{-\frac{1}{\delta}, -2\frac{3-2\delta}{1+2\delta}, -\frac{4}{1+2\delta}\}$; these two first schemes are not parametrized; the LMKC refers to their third scheme which belongs to MPLI with $\hat{K}^+ = 0$ and $\hat{\alpha} = -1$. The (anti-bounce-back) ABB (and implicit interface) correspond to MPLI with $\delta = \frac{1}{2}$ and $\hat{F}_q = 0$; PAB $=$ PLI($\delta = \frac{1}{2}$) is the pressure scheme[30] (see also Table XI in Ref. 40).

The Dirichlet linear one-node families

	$\alpha^{(p)}$	$\hat{\alpha}$	β	$\hat{\beta}$	$\hat{F}_q = \hat{K}^+\hat{n}_q^+,\ \hat{K}^+:$
MPLI	$\forall\alpha^{(p)}$	$1 + \alpha^{(p)}\left(\frac{1}{2} + \delta\right)$	$-(1 + \alpha^{(p)}\delta)$	$1 + \frac{\alpha^{(p)}}{2}$	$-2 - \alpha^{(p)}\left(\frac{1}{2} + \delta\right)$
PLI	$\forall\alpha^{(p)}$	$1 + \alpha^{(p)}\left(\frac{1}{2} + \delta\right)$	$-(1 + \alpha^{(p)}\delta)$	$1 + \frac{\alpha^{(p)}}{2}$	$-2- \alpha^{(p)}\left(\frac{1}{2} + \delta - \Lambda^+\right)$

$\gamma f_q(\vec{r}_b, t)$. This strategy was adapted to reduce the staggered invariants and in the specific corner geometry,[22,30] but it also utilized as a regular linear treatment, e.g., Refs. 73, 88, and 106. In such case, Eq. (A1) reads

$$\begin{aligned} f_{-q}(\vec{r}_b, t+1) &= \mathrm{MR}_q(\vec{r}_b, t) + w_q(\vec{r}_q, \tilde{t}), \\ \mathrm{MR}_q &= \hat{\alpha}\hat{f}_q(\vec{r}_b, t) + \beta f_q(\vec{r}_b, t) + \hat{\beta}\hat{f}_{-q}(\vec{r}_b, t) \\ &\quad + \gamma f_q(\vec{r}_b - \vec{c}_q, t) + \hat{\gamma}\hat{f}_{-q}(\vec{r}_b - \vec{c}_q, t) + \hat{F}_q(\vec{r}_b, t). \end{aligned} \tag{A2}$$

The LI schemes are considered as the single-node three-population MR sub-class:

$$\mathrm{LI} = \mathrm{MR} \text{ with } \gamma = \hat{\gamma} = 0. \tag{A3}$$

TABLE XI. The two-node Dirichlet KMR1 scheme and SMR($\alpha^{(p)}$) family; w_q obeys Eq. (A4); Heuristic stability: KMR1: $\{\hat{\alpha} - \hat{\gamma}\} \in [-1, 1]$, $\hat{K}^+ \in [-1, 1]$ when $\Lambda^+ \in]0, \frac{1}{4}]$, $\forall\delta$; SMR: $\{\hat{\alpha} - \hat{\gamma}, \hat{K}^+\} \in [-1, 1]$ when $\alpha^{(p)} \in [-1, -\frac{1}{2}]$, $\forall\Lambda^\pm$ and $\forall\ \delta$. The SMR may vanish $\hat{K}^+$ with the specific $\alpha^{(p)}$. We employ SMR with an arbitrary coefficient $\alpha^{(p)}$ in the present steady-state computations and refer to it as PP, because all PP members produce the equivalent steady-state solutions.

The Dirichlet parabolic two-node schemes

	KMR1	SMR $\in$ PP family
$\hat{\alpha}$	-1	$\frac{1}{2}(2 + \alpha^{(p)}(1+\delta)^2)$
β	$\frac{-1 + 2\delta(1+\delta)}{(1+\delta)^2}$	$\frac{1}{4}(-4 - \alpha^{(p)}\delta(4 + 3\delta + 2\Lambda^+))$
$\hat{\beta}$	β	$\frac{1}{4}(4 + \alpha^{(p)}(2 - \delta^2 + 2\delta\Lambda^+))$
γ	$-\frac{\delta^2}{(1+\delta)^2}$	$\frac{1}{4}\alpha^{(p)}\delta(\delta + 2\Lambda^+)$
$\hat{\gamma}$	γ	$\frac{1}{4}\alpha^{(p)}\delta(\delta + 2\Lambda^+)$
$\hat{F}_q = \hat{K}^+\hat{n}_q^+$, $\hat{K}^+$	$\alpha^{(p)}\Lambda^+$	$-\frac{1}{2}(4 + \alpha^{(p)}(1+\delta)(1 + \delta - 2\Lambda^+))$
$\alpha^{(p)}$	$-\frac{4}{(1+\delta)^2}$	$\forall\,\alpha^{(p)}$

We provide the coefficients for several linear and parabolic Dirichlet families, advective-diffusive flux schemes and diffusive-flux family. An MR family with infinite number of members is controlled by the free-tunable coefficient as, typically, the scale factor of the underlying closure relation, $\alpha^{(p)}$ in Dirichlet families. The coefficients of (i) the exact steady-state MR form in Eq. (34) and (ii) the corresponding second-order closure approximate in Eq. (5), are tabulated for all schemes. The mixed (Robin) schemes can be built as the linear combinations of the Dirichlet and diffusive-flux MR following.[40] All provided MR schemes support the bulk parametrization of the ADE solutions by the grid Péclet number and free collision product Λ using TRT. When the MR coefficients depend upon Λ^+, they should be computed with the free-tunable collision rate of the symmetric modes in $\mathrm{TRT}^{(+)} \cup \mathrm{MRT}^{(-)}$ collision operators,[32,40,101] which are sufficient for isotropic and anisotropic diagonal tensors. Accordingly, $\Lambda = \Lambda^+\Lambda^-$ is defined in TRT or $\mathrm{TRT}^{(+)} \cup \mathrm{MRT}^{(-)}$ isotropic collisions, where Λ^- corresponds to the common rate of the discrete-velocity eigenvectors. In the

TABLE XII. The ADE Dirichlet scheme PPLI is exact on the parabolic, pure-diffusion and grid-aligned flow, profiles in an inclined channel; PPLI shares MPLI/PLI coefficients from Table X, Eq. (14a), $\Lambda^- = c_e^{-1}\mathscr{D}_0$. The fluid velocity Dirichlet scheme IPLI is exact in the inclined Poiseuille flow; IPLI is specified with the Stokes equilibrium $e_q^-(\vec{j})$, $\vec{j} = \sum_{q=1}^{Q-1} f_q\vec{c}_q + \frac{1}{2}\vec{F}$, $\Lambda^+ = 3\nu$. Heuristic stability: $\{\hat{\alpha}, \beta, \hat{\beta}\} \in [-1, 1]$ when $\Lambda \in [0, \frac{\delta^2}{2}]$, and then only when $\Lambda \to 0$, $\forall\ \delta$.

The Dirichlet parabolic single-node ADE and flow schemes

	PPLI	IPLI
$\hat{\alpha}$	$1 + \alpha^{(p)}\left(\frac{1}{2} + \delta\right)$	$-1 + \alpha^{(u)}\left(\frac{1}{2} + \delta\right)$
β	$-(1 + \alpha^{(p)}\delta)$	$1 - \alpha^{(u)}\delta$
$\hat{\beta}$	$1 + \frac{\alpha^{(p)}}{2}$	$1 - \frac{\alpha^{(u)}}{2}$
γ, $\hat{\gamma}$, $\hat{F}_q$	0	0
$\alpha^{(p)}$, $\alpha^{(u)}$	$\frac{-4\Lambda^-}{\delta^2 + \Lambda^-(1+2\delta) - 2\Lambda}$	$\frac{4\Lambda^+}{\delta^2 + \Lambda^+(1+2\delta) - 2\Lambda}$
w_q	$-\alpha^{(p)}t_q^{(m)}c_e(P + \Lambda^+\mathscr{M})\vert_{\vec{r}_q}$	$-\alpha^{(u)}t_q^{\star}(\vec{j} + \Lambda^-\vec{F})\cdot\vec{c}_q\vert_{\vec{r}_q}$

TABLE XIII. Equations (34) and (35) are specified for Dirichlet schemes from Tables X–XII.

Exact steady-state form in Eqs. (34) and (35)	MPLI	PLI	PPLI	KMR1	PP
$m_1/\alpha^{(p)}$	1	1	1	$1-\frac{1}{2}\delta^2$	$1-\frac{1}{2}\delta^2$
$m_3\times\Lambda^-/\alpha^{(p)}$	$-\Lambda$	0	$-\frac{\delta^2}{2}$	$\frac{1}{2}\delta^2\Lambda$	$\frac{1}{2}\delta(3+\delta)\Lambda$
$m_5/\alpha^{(p)}$	0	0	0	$\frac{1}{2}\delta^2$	$\frac{1}{2}\delta^2$
$m_7\times\Lambda^-/\alpha^{(p)}$	0	0	0	$-\frac{1}{2}\delta^2\Lambda$	$-\frac{1}{2}\delta(1+\delta)\Lambda$
$m_2\times\Lambda^-/\alpha^{(p)}$	0	0	0	0	$-\delta\Lambda$
$m_4/\alpha^{(p)}$	δ	δ	δ	$\delta+\frac{3}{4}\delta^2$	$\frac{1}{4}\delta(4+3\delta+4\Lambda)$
$m_6\times\Lambda^-/\alpha^{(p)}$	0	0	0	$\delta\Lambda$	
$m_8/\alpha^{(p)}$	0	0	0	$-\frac{1}{4}\delta^2$	$-\frac{1}{4}\delta(\delta+4\Lambda)$

TABLE XIV. The coefficients of the approximate closure relation in Eq. (5) with the Dirichlet schemes from Table XIII. The ABB and implicit interface correspond to MPLI with $\delta=\frac{1}{2}$; PAB = PLI($\delta=\frac{1}{2}$) is the pressure scheme.[30]

Directional closure relation in Eq. (5)					
Eq. (5)	MPLI	PLI	PPLI	KMR1	PP
$\alpha^{(p)}/\alpha^{(p)}$	1	1	1	1	1
$\beta^{(p)}/\alpha^{(p)}$	δ	δ	δ	δ	δ
$\gamma^{(p)}/\alpha^{(p)}$	Λ	0	$\frac{1}{2}\delta^2$	$\frac{1}{2}\delta^2$	$\frac{1}{2}\delta^2$
$\alpha^{(u)}/\alpha^{(p)}$	0	0	0	0	0
$\beta^{(u)}/\alpha^{(p)}$	$-\Lambda^+$	0	$-\frac{\delta^2}{2\Lambda^-}$	0	0
$\gamma^{(u)}/\alpha^{(p)}$	$-\delta\Lambda^+$	$-\delta\Lambda^+$	$-\delta\Lambda^+$	$-\delta\Lambda^+$	0

TABLE XV. The single-node FLI and two-nodes FMR advective-diffusive flux families; w_q obeys Eq. (22a). FLI : $\{\hat{\alpha},\beta,\hat{\beta}\}\in[-1,1]$; FMR : $\{\hat{\alpha},\beta,\hat{\beta},\gamma,\hat{\gamma}\}\in[-1,1]$ when $\Lambda\in]0,\frac{3}{4}]$, $\forall\delta$.

The advective-diffusive flux schemes	FLI	FMR
$\hat{\alpha}$	1	$\frac{\alpha^{(u)}}{4}((1+\delta)^2-2\Lambda)$
β	$\frac{1-2\delta}{1+2\delta}$	$\alpha^{(u)}(\frac{1}{4}-\frac{1}{2}\delta(1+\delta)+\Lambda)$
$\hat{\beta}$	$-\beta$	$-\beta$
γ	0	$\alpha^{(u)}((1+\delta)^2-2\Lambda)$

TABLE XV. (*Continued.*)

The advective-diffusive flux schemes	FLI	FMR
$\hat{\gamma}$	0	$-\gamma$
$\hat{F}_q$	0	0
$\alpha^{(u)}$	$\frac{4}{1+2\delta}$	$\frac{4}{(1+\delta)^2-2\Lambda}$

TABLE XVI. The diffusive-flux DFLI family prescribes $w_q(\vec{r}_q)$ with Eq. (22b); the DFLI reduces to back-sided $\hat{n}_q^-$– extrapolation in 1D, Eq. (73). The SFLI has several heuristic sub-domains $\{\hat{\alpha},\beta,\hat{\beta},\gamma,\hat{\gamma}\}\in[-1,1]$, they include: $(\Lambda>3\Lambda^-)$ $\&\&\beta'\in]0,\frac{2}{\delta\Lambda^-+\Lambda}]$; the SFLI is able to adjust $\hat{K}^+$ to $[-1,1]$. The AFLI is more restrictive. We apply SFLI and refer to it as DFLI because steady-state solution are the same with any DFLI member.

Two diffusive-flux DFLI families, $\forall\,\beta'$	SFLI(β'), $\forall\,\beta'$	AFLI(β'), $\forall\,\beta'$
$\hat{\alpha}$	$1-\beta'(1+\delta)\Lambda^-$	$-(1+\beta'\Lambda)$
β	$-1+\frac{\beta'}{2}((2+3\delta)\Lambda^-+\Lambda))$	$1+\frac{\beta'}{2}(\delta\Lambda^-+3\Lambda)$
$\hat{\beta}$	$1+\frac{\beta'}{2}(\delta\Lambda^--\Lambda)$	$1+\frac{\beta'}{2}(\delta\Lambda^--\Lambda)$
γ	$-\frac{\beta'}{2}(\delta\Lambda^-+\Lambda)$	$-\frac{\beta'}{2}(\delta\Lambda^-+\Lambda)$
$\hat{\gamma}$	$-\frac{\beta'}{2}(\delta\Lambda^--\Lambda)$	$-\frac{\beta'}{2}(\delta\Lambda^--\Lambda)$
$\hat{F}_q$	$\hat{K}^+\hat{n}_q^+$, $\hat{K}^+=-\hat{K}^-\vert_{\mathrm{AFLI}}$	$\hat{K}^-\hat{n}_q^-$, $\hat{K}^-=2-\beta'((1+\delta)\Lambda^--\Lambda)$

TABLE XVII. Equations (34) and (35) in FLI and FMR advective-diffusive schemes from Table XV [$\alpha^{(u)}$ is given there], and diffusive-flux family DFLI from Table XVI [β' is free-tunable].

The exact steady-state form in Eqs.(34)-(35)	FLI	FMR		DFLI, $\forall\,\beta'$
$m_1/(\Lambda^-\alpha^{(u)})$	0	0	$m_1/(\Lambda^-\beta')$	δ
$m_3/\alpha^{(u)}$	δ	$\delta+\frac{3\delta^2}{4}-\frac{3}{2}\Lambda$	m_3/β'	$-\frac{1}{2}(3+2\delta)\Lambda$
$m_5/(\Lambda^-\alpha^{(u)})$	0	0	$m_5/(\Lambda^-\beta')$	$-\delta$
$m_7/\alpha^{(u)}$	0	$-\frac{\delta^2}{4}+\frac{1}{2}\Lambda$	m_7/β'	$\frac{1}{2}(1+2\delta)\Lambda$
$m_2/\alpha^{(u)}$	1	$1-\frac{1}{2}\delta^2+\Lambda$	m_2/β'	Λ
$m_4/(\Lambda^-\alpha^{(u)})$	-1	$-\left(1-\frac{1}{2}\delta^2+\Lambda\right)$	$m_4/(\Lambda^-\beta')$	$-\frac{1}{2}(2+3\delta+2\Lambda)$

TABLE XVII. (*Continued.*)

The exact steady-state form in Eqs.(34)-(35)				
	FLI	FMR		DFLI, $\forall\beta'$
$m_6/\alpha^{(u)}$	0	$\frac{1}{2}\delta^2-\Lambda$	m_6/β'	$-\Lambda$
$m_8/(\Lambda^-\alpha^{(u)})$	0	$\Lambda-\frac{1}{2}\delta^2$	$m_8/(\Lambda^-\beta')$	$\frac{1}{2}(\delta+2\Lambda)$

TABLE XVIII. The approximate closure relation (5) with {FLI,FMR} and DFLI from Tables XV–XVII, respectively [$\alpha^{(u)}$ is given in Table XV, β' is free-tunable].

Directional closure relation in Eq. (5)			
Eq. (5)	FLI	FMR	DFLI(β'), $\forall\beta'$
$\alpha^{(u)}/\alpha^{(u)}$	1	1	$\alpha^{(u)}=0$
$\beta^{(u)}/\alpha^{(u)}$	δ	δ	$\beta^{(u)}=0$
$\gamma^{(u)}/\alpha^{(u)}$	Λ	$\frac{1}{2}\delta^2$	$\gamma^{(u)}=0$
$\alpha^{(p)}/\alpha^{(u)}$	0	0	$\alpha^{(p)}=0$
$\beta^{(p)}/\alpha^{(u)}$	$-\Lambda^-$	$-\Lambda^-$	$\beta^{(p)}=-\beta'\Lambda^-$
$\gamma^{(p)}/\alpha^{(u)}$	$-\Lambda^-\delta$	$-\Lambda^-\delta$	$\gamma^{(p)}=-\beta'\Lambda^-\delta$

presence of mass-source $\mathscr{M}(\vec{r})$, the Dirichlet schemes prescribe the directional boundary value $w_q(\vec{r}_q,\tilde{t})$ through e_q^+ from Eq. (14a):

$$w_q(\vec{r}_q,\tilde{t})=-\alpha^{(p)}c_e t_q(P+(1-I_b)\Lambda^+\mathscr{M})(\vec{r}_q,\tilde{t}). \tag{A4}$$

We prescribe regularly $I_b=0$ in Eq. (A4) to vanish the mass-source from the Dirichlet LI and MR closure in Eq. (5); in contrast, the ABB and LI rules[62,96] commonly apply $I_b=1$, and the mass-source term then couples with the parabolic error. We refer to work[40] for more details and extension for MRT collisions.

APPENDIX B: RECONSTRUCTION STEP

Example 1: The matrix $\mathbf{B}$ in Eq. (17) can be expressed in the Cartesian system and Eq. (17) is then solved with respect to $\mathbf{Y}_0[5]=\{\partial_x P,\partial_y P,\partial^2_{xx}P,\partial^2_{yy}P,\partial^2_{xy}P\}$. The vector $\mathbf{Y}[5]=\{\partial_\tau P,\partial_n P,\partial^2_{\tau\tau}P,\partial^2_{nn}P,\partial^2_{\tau n}P\}$ from Eq. (11) obtains the same solution as when Eq. (17) is solved in the $(\vec{1}_\tau,\vec{1}_n)$ system using the coordinate transform:

$$\begin{aligned}\partial_\tau P&=\cos[\theta]\partial_x P+\sin[\theta]\partial_y P,\\ \partial_n P&=\cos[\theta]\partial_y P-\sin[\theta]\partial_x P,\\ \partial^2_{\tau\tau}P&=\cos^2[\theta]\partial^2_{xx}P+\sin[2\theta]\partial^2_{xy}P+\sin^2[\theta]\partial^2_{yy}P,\\ \partial^2_{nn}P&=\cos^2[\theta]\partial^2_{yy}P-\sin[2\theta]\partial^2_{xy}P+\sin^2[\theta]\partial^2_{xx}P,\\ \partial^2_{\tau n}P&=\cos[2\theta]\partial^2_{xy}P+\frac{1}{2}\sin[2\theta](\partial^2_{yy}P-\partial^2_{xx}P).\end{aligned} \tag{B1}$$

Example 2: We exemplify Eq. (19) with a constant velocity and mass source. If one replaces the fifth component $\hat{n}_q^+$ in Eq. (19) by $\hat{n}_q^-$, $|\det[\mathbf{B}]|$ reads in Eq. (17):

$$\mathrm{III}:\hat{\mathbf{n}}[5]=\{\hat{n}_1^+,\hat{n}_1^-,\hat{n}_2^+,\hat{n}_2^-\}\cup\hat{n}_q^-,\ q=3(a)\ \text{or}\ q=4(b):$$
$$|\det[\mathbf{B}]|=2t_d^{(a)}c_e\Lambda^+|(\vec{u}\cdot\vec{c}_q)\Pi_{j=1}^{j=2}(t_c^{(m)2}c_e^2\Lambda^--t_c^{(a)2}\Lambda^+(\vec{u}\cdot\vec{c}_j)^2)|. \tag{B2a}$$

$$\mathrm{IV}:\hat{\mathbf{n}}[5]=\{\hat{n}_3^+,\hat{n}_3^-,\hat{n}_4^+,\hat{n}_4^-\}\cup\hat{n}_q^-,\ q=1(a)\ \text{or}\ q=2(b):$$
$$|\det[\mathbf{B}]|=8t_c^{(a)}c_e\Lambda^+|(\vec{u}\cdot\vec{c}_q)\Pi_{j=3}^{j=4}(t_d^{(m)2}c_e^2\Lambda^--t_d^{(a)2}\Lambda^+(\vec{u}\cdot\vec{c}_j)^2)|. \tag{B2b}$$

Hence, unlike in Eq. (19), $|\det[\mathbf{B}]|$ vanishes when $\vec{u}$ and $\vec{c}_q$ are orthogonal.

Example 3: We exemplify Eq. (17) with the velocity field from Eq. (45). For the sake of simplicity, we consider the straight system $\vec{u}=u_\tau(y)\vec{1}_x$ and the weights $t_q^{(m)}=t_q^{(a)}=t_q=\{t_c,t_d\}$; since $u_\tau(y)$ and $\mathscr{M}(y)$ are parabolic, Eq. (16) is expressed by Eq. (57). The weight t_q is factorized and the reduced matrix $\tilde{\mathbf{B}}[6\times5]$ and RHS $\tilde{\mathbf{R}}[6]$ in Eq. (17) read with $\xi=2\Lambda^+\partial_n u_\tau$:

$$\tilde{\mathbf{B}}=\begin{pmatrix}u_\tau & u_\tau & -c_e\Lambda^- & -2c_e\Lambda^- & -c_e\Lambda^-\\ u_\tau & -u_\tau & -c_e\Lambda^- & 2c_e\Lambda^- & -c_e\Lambda^-\\ c_e-\xi & c_e-\xi & -\Lambda^+u_\tau & -2\Lambda^+u_\tau & -\Lambda^+u_\tau\\ -c_e-\xi & c_e+\xi & \Lambda^+u_\tau & -2\Lambda^+u_\tau & \Lambda^+u_\tau\\ u_\tau & 0 & -c_e\Lambda^- & 0 & 0\\ 0 & 0 & 0 & 0 & -c_e\Lambda^-\end{pmatrix} \tag{B3}$$

and

$$\tilde{\mathbf{R}}[6]=t_q^{-1}\hat{\mathbf{n}}-t_q^{-1}\hat{\mathbf{n}}|_{\mathbf{Y}=0},$$
$$t_q^{-1}\hat{\mathbf{n}}=\left\{\frac{\hat{n}_3^+}{t_d},\frac{\hat{n}_4^+}{t_d},\frac{\hat{n}_3^-}{t_d},\frac{\hat{n}_4^-}{t_d},\frac{\hat{n}_1^+}{t_c},\frac{\hat{n}_2^+}{t_c}\right\}^T, \tag{B4a}$$

$$\begin{aligned}t_q^{-1}\hat{\mathbf{n}}|_{\mathbf{Y}=0}=&\{-c_e\Lambda\partial_n^2\mathscr{M}+\partial_n u_\tau P,-c_e\Lambda\partial_n^2\mathscr{M}-\partial_n u_\tau P,\\ &c_e\Lambda^+\partial_n\mathscr{M}-\Lambda^+P\partial_n^2u_\tau,c_e\Lambda^+\partial_n\mathscr{M}+\Lambda^+P\partial_n^2u_\tau,0,\\ &-c_e\Lambda\partial_n^2\mathscr{M}\}^T.\end{aligned} \tag{B4b}$$

When $u_\tau(y)$ and $\mathscr{M}(y)$ are constant, Eq. (B4b) vanishes. Equations (B3) and (B4) correspond to an ensemble of six components $\hat{n}_q^\pm$ in Eq. (19b). The two square $[5\times5]$ sub-systems $\mathbf{BY}[5]=\mathbf{R}$ in Eq. (17), referred to as N-MR$_1$ and N-MR$_2$ in Table III, only differ for the two last lines, corresponding to $\hat{n}_1^+$ $(q=1)$ or $\hat{n}_2^+$ $(q=2)$, respectively, in Eqs. (B3) and (B4); the two sub-systems operate Eq. (17) with $|\det[\mathbf{B}]|=t_c t_d^4|\det[\tilde{\mathbf{B}}]|$:

$$|\det[\tilde{\mathbf{B}}]|=8c_e\Lambda^-|(c_e^4\Lambda^{-2}+\Lambda^{+2}u_\tau^4-2c_e^2\Lambda(2\Lambda(\partial_n^2u_\tau)^2+u_\tau^2))|. \tag{B5}$$

Example 4: *The A-LSOB algorithm* The steady-state A-LSOB formulation is resumed in Sec. III E. The Taylor schemes given in Eq. (12) prescribe one closure equation for the wall-normal direction traced from the boundary node $\vec{r}_b$. Additionally, the N_b-1 "expansions" are prescribed with Eq. (40) for the given N_b cut links $q\in Q_b$, where $\hat{n}_q^{\pm(2)}$ obeys Eq. (16) and the five derivatives $\mathbf{Y}[5]$ are expressed linearly with Eq. (17). Let us exemplify (i) the "expansion" subset Q_e in Eq. (40) and (ii), the "reconstruction" subset Q_r in Eq. (17) assuming that $N_b\le4$. Optionally, we set $Q_e\in Q_b$

and, when possible, prescribe $Q_e \cap Q_r = \varnothing$. Prior, we preselect the type of $\hat{n}_{rec}$, e.g., $\hat{n}_{rec} = \{\hat{n}_q^+\}$ or $\hat{n}_{rec} = \{\hat{n}_q^-\}$, then Q_r is described with Eq. (19) or Eq. (B2), respectively. We prescribe Eq. (40) for the two components $\hat{n}_q^{\pm(2)}$ with the first link in Q_e when $N_b - 1 \geq 2$, and then either $\hat{n}_q^{+(2)}$ [if $\hat{n}_{rec} = \{\hat{n}_q^+\}$] or $\hat{n}_q^{-(2)}$ [if $\hat{n}_{rec} = \{\hat{n}_q^-\}$] for the second link in Q_e when $N_b - 1 = 3$. This last rule also applies if $N_b - 1 = 1$ and Q_e prescribes only one equation. We operate with $\{q_1, q_2, q_3, q_4\}$ for the links $\pm\vec{c}_q = \{(1,0),(0,1),(1,1),(-1,1)\}$, and we preselect the reconstruction default type r − default. The Q_e and $Q_r(\vec{r}_b)$ are optionally set as

1. If $N_b = 1$ then r − default applies, $Q_e = \varnothing$ because $N_b - 1 = 0$, done = 1.
2. If $Q_b = \{q_1, q_2\}$, and $|(c_{q_2} \cdot \vec{1}_n)| > |(c_{q_1} \cdot \vec{1}_n)|$, then $Q_e = \{q_2\}$ and $Q_r = \{q_3, q_4, q_1\}$, else $Q_e = \{q_1\}$ and $Q_r = \{q_3, q_4, q_2\}$; done = 1.
3. If $Q_b = \{q_1, q_3, q_4\}$, then $Q_e = \{q_1\}$ and $Q_r = \{q_3, q_4, q_2\}$, i.e., IIb in Eq. (19b) if $\hat{n}_{rec} = \{\hat{n}_q^+\}$ or IVb in Eq. (B2b) if $\hat{n}_{rec} = \{\hat{n}_q^-\}$; done = 1.
4. If $Q_b = \{q_2, q_3, q_4\}$, then $Q_e = \{q_2\}$ and $Q_r = \{q_3, q_4, q_1\}$, i.e., IIa in Eq. (19b) if $\hat{n}_{rec} = \{\hat{n}_q^+\}$ or IVa in Eq. (B2b) if $\hat{n}_{rec} = \{\hat{n}_q^-\}$; done = 1.
5. If done = 0, $q_4 \in Q_b$ and $|(c_{q_4} \cdot \vec{1}_n)| > |(c_{q_3} \cdot \vec{1}_n)|$, then
   (a) If $N_b = 2$ or $N_b = 3$, then $Q_e = q_4$ for n_q^+, $Q_r = \{q_1, q_2, q_3\}$, i.e., Ia in Eq. (19b) if $\hat{n}_{rec} = \{\hat{n}_q^+\}$ or IIIa in Eq. (B2b) if $\hat{n}_{rec} = \{\hat{n}_q^-\}$; done = 1.
   (b) If $N_b = 4$, then $Q_e = \{q_4, q_3\}$, $Q_r = \{q_1, q_2, q_3\}$; done = 1.
6. If done = 0, $q_3 \in Q_b$ and $|(c_{q_3} \cdot \vec{1}_n)| > |(c_{q_4} \cdot \vec{1}_n)|$, then the Step 5 exchanges q_3 and q_4.

In our examples, r-default is rectangular with Eq. (20); T-PP and T-DFLI apply the square reconstruction except when $N_b = 1$ (step 1); T-PP$_r$ and T-DFLI$_r$ apply Eq. (20) in all nodes but Q_e is set according to the above algorithm. Let us exemplify the straight horizontal wall: $N_b = 3$, $Q_b = \{q_2, q_3, q_4\}$, then $Q_e = \{q_2\}$ and $Q_r = \{q_3, q_4, q_1\}$ according to Step 3. Equation (40) prescribes two "expansions" $\hat{n}_{q_2}^{\pm(2)}$, and reconstruction is performed using subset IIa in Eq. (19b) when $\hat{n}_{rec} = \{\hat{n}_q^+\}$, or subset IVa in Eq. (B2b) when $\hat{n}_{rec} = \{\hat{n}_q^-\}$.

APPENDIX C: EXACT STRAIGHT QUARTIC SOLUTIONS DUE TO CORRECTIVE FLUX

We prescribe $\Lambda_0^{(ex)} = \frac{1}{6(1-c_e)}$ from Eq. (52) and consider the exact quartic solution from Eqs. (48a) and (46) with an impermeable horizontal boundary. **Example 1a** derives Eq. (61a) where FLI matches this solution exactly with the help of the corrective flux $\Phi_0 = \mathscr{D}\chi$ from Eq. (32); BB [FLI with $\delta = \frac{1}{2}$] reduces this solution to Eq. (60b). **Examples 2 and 3** demonstrate that FLI$_n$ [which is FLI with the normal mass-source correction from Eq. (24b)] and the Taylor scheme T-DFLI$_1$ are exact with the same solution $|\Phi_0|$ reproduced in Eq. (62). **Example4** generalizes these solutions for the MR flux schemes, like FLI, FMR or T-DFLI. In these derivations, $\vec{1}_{y'} = \vec{1}_y$, the boundary nodes are $y_b = \delta_B$ (bottom) and $y_b = h - \delta_T$ (top), and the prescribed corrective flux reads with $\mathscr{D} = c_e\Lambda^-$, as

$$-\mathscr{D}\partial_{y'}P|_{y'=0} = \mathscr{D}\chi(\delta_T),\ -\mathscr{D}\partial_{y'}P|_{y'=h} = -\mathscr{D}\chi(\delta_B). \tag{C1}$$

Equation (C1) reduces to Eq. (32) when $\delta_T = \delta_B = \delta$. Solution $P(y)$ is the same with d2q5 and d2q9 in the straight system; d2q5 satisfies Eq. (28) with

$$\hat{n}_q^+(y) = t_q\mathscr{M}(y)c_{qy}^2 = -t_q\mathscr{D}\partial_y^2 P(y),\ \text{and} \tag{C2a}$$

$$\partial_y^{(n)}\mathscr{M}(y) = -\mathscr{D}\partial_y^{(n+2)}P(y),\ n = 0,1,2. \tag{C2b}$$

In this section, $\partial_y^{(n)}P(y)$ denotes the exact derivatives on the quartic solution from Eq. (46). Equation (15c) gives, by replacing the central-difference Δ_y with its exact Taylor expression and using Eq. (C2b):

$$\begin{aligned}
\Lambda^-\hat{n}_q^-(y) &= t_q\left[c_e\Lambda^-\Delta_y(P + \Lambda^+\mathscr{M}) - \left(\Lambda - \frac{1}{4}\right)\Delta_y\mathscr{M}\right]\\
&= t_q\left[c_e\Lambda^- c_{qy}\left(\partial_y P + \partial_y^3 P\left(\frac{1}{6} - c_e\Lambda + \left(\Lambda - \frac{1}{4}\right)\right)\right)\right],\\
&\text{then, giving}\ \Lambda = \Lambda_0^{(ex)},\\
&-\Lambda^-\hat{n}_q^- = -t_q\mathscr{D}c_{qy}(\partial_y P(y) + \delta T(y)),\\
&\delta T(y) = \frac{1}{12}c_{qy}\partial_y^3 P(y).
\end{aligned} \tag{C3}$$

Example 1a: We apply FLI with the corrective flux from Eq. (C1). The exact closure from Eq. (34) reads with $e_q^- = 0$ on the vertical cut link $c_{qy} = 1$ [$y_b = h - \delta_T$] and $c_{qy} = -1$ [$y_b = \delta_B$]. We substitute there $m_3/\alpha^{(u)} = \delta$ and $m_4/\alpha^{(u)} = -\Lambda^-$ from Table XVII, and the closure condition becomes

$$-\Lambda^-\hat{n}_q^- + \delta\hat{n}_q^+|_{y_b} = -t_q\mathscr{D}\chi(\delta)|_{y_b}c_{qy}^2. \tag{C4}$$

Equation (C4) reads plugging there Eqs. (C2a) and (C3),

$$-\mathscr{D}(\partial_y P c_{qy} + \delta\partial_y^2 P c_{qy}^2 + \delta T)|_{y_b} = -\mathscr{D}\chi|_{y_b}c_{qy}^2. \tag{C5}$$

Equation (C5) presents the fourth-order accurate Taylor closure relation provided that

$$\chi(\delta)c_{qy}^2 = -\left(\frac{1}{2}\delta^2 c_{qy}\partial_y^3 P + \frac{1}{6}\delta^3 c_{qy}^2\partial_y^4 P - \delta T\right)\Big|_{y=y_b}. \tag{C6}$$

Plugging the exact derivatives from Eq. (46) and Eq. (C3) for δT, Eq. (C6) gives when $\delta = \frac{1}{2}$,

$$\begin{aligned}
\text{BB}: \chi\left(\delta = \frac{1}{2}\right)c_{qy}^2 &= \frac{\psi' c_{qy}^2}{16}(h-1) + \frac{\psi' c_{qy}^2}{48} - \frac{\psi' c_{qy}^2}{24}(h-1),\\
\text{then}\ \chi\left(\delta = \frac{1}{2}\right) &= \frac{\psi' h}{48} = \frac{\text{Pe}}{4h^2},\ \text{with}\\
\text{Pe} &= \frac{\mathscr{U}h}{\mathscr{D}} = \frac{\psi' h^3}{12},\ \mathscr{U} = \frac{\Psi h^2}{12}.
\end{aligned} \tag{C7}$$

When $\delta_T = \delta_B = \delta$ and $y_b = \{\delta, h - \delta\}$, Eq. (C6) gives

$$\text{FLI}: \chi(\delta) = \frac{\text{Pe}}{h^2}\left(3\delta^2 - \frac{1}{2} + \frac{\delta(1 - 4\delta^2)}{h}\right). \tag{C8}$$

Equation (C8) reduces to Eq. (C7) when $\delta = \frac{1}{2}$. It is confirmed that the numerical solution with Eq. (32) reproduces the symmetric solution from Eq. (C8) exactly. When $\delta_B \neq \delta_T$, this solution is not symmetric and it cannot be exactly reproduced with Eq. (32); it is then validated by prescribing Eq. (C1) for the boundary flux and reproducing the exact quartic profile.

Example 1b: Curiously, BB is able to reproduce the exact quartic solution for *any symmetric walls* thanks to Φ_0. The derivation follows the same lines, replacing δT from Eq. (C3) by $\delta T + (\frac{1}{2} - \delta)\partial_y^2 P c_{qy}^2$. Equation (C8) then becomes

$$\chi(\delta) = -\frac{\text{Pe}}{2h^2}\left(1 + \frac{(1-2\delta)}{h}\right)(2(\delta-1)\delta + (1-2\delta)h). \quad \text{(C9)}$$

Example 2: When the MR is complemented with the normal mass-source correction [$I_n^{(\mathscr{M})} = 1$ in Eq. (21)], the LHS of the closure relation in Eq. (C4) gets an additional term $\mathscr{E}_{q_b}^{(-)} = \text{CL}_{qn}(\Lambda^+\mathscr{M}, 0)/\alpha^{(u)}$ from Eq. (24b). It reads with $\beta^{(p)}/\alpha^{(u)} = -\Lambda^-$, $\gamma^{(p)}/\alpha^{(u)} = -\Lambda^-\delta$ from Table XVIII:

$$\begin{aligned}\mathscr{E}_{q_b}^{(-)} &= t_q\Lambda^+ c_e(-\Lambda^-\partial_n\mathscr{M}c_{qn} - \Lambda^-\delta\partial_{nn}^2\mathscr{M}c_{qn}^2)|_{y_b}\\ &= t_q\mathscr{D}c_e\Lambda(\partial_y^3 P c_{qy} + \delta\partial_y^4 P c_{qy}^2)|_{y_b} = -\frac{6t_q\mathscr{D}c_e\Lambda\text{Pe}}{h^2}c_{qy}^2. \end{aligned}\quad \text{(C10)}$$

Equation (C10) is expressed with $\Lambda_0^{(ex)}$ in Eq. (62), Eq. (C11) then becomes

$$\chi(\delta) = \frac{\text{Pe}}{h^2}\left(3\delta^2 - \frac{1+c_e}{2(1-c_e)} + \frac{\delta(1-4\delta^2)}{h}\right), \forall\delta. \quad \text{(C11)}$$

Example 3: We show that Eq. (C11) also satisfies the Taylor scheme T-DFLI provided that Eq. (57) applies on the vertical cut link, as for example with T-DFLI$_1$ or T-DFLI$_r$, using the notations from Table III and **example 4** from Sec. B. We then equate Eq. (57) to $\hat{n}_2^{-ex}$ and $\hat{n}_2^{+ex}$ from Eqs. (C3) and (C2a), respectively, this gives

$$\partial_y P^{(num)} = \partial_y P + \left(\Lambda_0^{(ex)} - \frac{1}{12}\right)\partial_y^3 P, \quad \text{(C12a)}$$

$$\partial_{yy}^2 P^{(num)} = \partial_{yy}^2 P + c_e\Lambda_0^{(ex)}\partial_y^4 P. \quad \text{(C12b)}$$

Equation (12b) becomes modified by the corrective flux from Eq. (C1) and it reads

$$-\mathscr{D}(\partial_y P^{(num)} + \delta c_{qy}\partial_{yy}^2 P^{(num)})|_{y=y_b} = -\mathscr{D}\chi c_{qy}. \quad \text{(C13)}$$

Plugging Eq. (C12) into Eq. (C13), it reproduces Eq. (C11). Therefore, the T-DFLI$_1$ is equivalent to FLI$_n$ on these solutions. In contrast, T-DFLI$_2$ produces the same solution for $\partial_{yy}^2 P^{(num)}$, but differs for $\partial_y P^{(num)}$ and then $\chi(y_b)$.

Example 4: We extend now Eqs. (C8) and (C11) to other MR flux schemes, as FMR and DFLI, prescribing Eq. (34) on the vertical cut link. The corrective flux presents the difference between the MR closure relation and the fourth-order accurate Neumann condition, as

$$\begin{aligned}&W_q^{(u)-1}\left[M_{q_b}\cdot X_{q_b} - \mathscr{E}_{q_b}^{(-)}\right] - T^{(4)}|_{y_b} = -\mathscr{D}\chi(\delta)c_{q_b y}^2,\\ &\text{with } T^{(4)} = -\mathscr{D}\sum_{m=1}^{4}\frac{\delta^{(m-1)}}{(m-1)!}\partial_y^m P^{(ex)}.\end{aligned}\quad \text{(C14)}$$

The term $M_{q_b}\cdot X_{q_b}$ is expressed with $M_{q_b}[8] = \{m_i\}$; $W_q^{(u)} = \alpha^{(u)}$ in FLI/FMR and $W_q^{(u)} = \beta'$ in T-DFLI [cf. Eq. (39)]; these coefficients are pre-computed in Table XVII. The components $X_{q_b}[8]$ are expressed exactly: (i) e_q^+ with Eq. (46); (ii) $e_q^- = 0$; (iii) $\hat{n}_q^+(y)$ with Eq. (C2a) and (iv), $\hat{n}_q^-(y)$ with Eq. (C3). It is confirmed that FLI reduces Eq. (C14) to Eq. (C8); additionally, FMR and DFLI substitute the exact solution components in the neighbor node $\vec{r}_b - q_b$. Equation (61) resumes their solutions with respect to FLI. Next, FLI$_n$, FMR$_n$ and DFLI$_n$ apply the normal mass-source correction $\mathscr{E}_q^{(-)} = \text{CL}_{qn}(\Lambda^+\mathscr{M}, 0)$ from Eq. (24b) which reads with the same coefficients in three schemes: $\beta^{(p)}/W_q^{(u)} = -\Lambda^-$ and $\gamma^{(p)}/W_q^{(u)} = -\Lambda^-\delta$ (see Table XVIII). Equation (C10) gives then the same (negative value) correction $\mathscr{E}_{q_b}^{(-)}$, expressed with $\Lambda_0^{(ex)}$ in Eq. (62), and then χ in Eq. (C11).

APPENDIX D: MASS-BALANCE OVER A GRID-SHIFTED STRAIGHT INTERFACE

We construct FLI/FMR and DFLI solutions for M_0 from Eq. (28) in the straight grid-shifted layers subject to piece-wise constant mass-source and either interface-parallel or perpendicular velocity field. These results are resumed in Sec. VI A 2.

1. The advective-diffusive flux FLI/FMR

The macroscopic solution in the straight geometry is weight-independent, and it can be examined with the d2q5 exact recurrence solution from Eqs. (66) and (67). It can be then demonstrated that FLI and FMR have the same interface closure given in Eq. (76b). We examine their mass-balance with FLI, without construction of its symbolic solution; recall, FLI reduces to BB (implicit interface, or do nothing algorithm) on the mid-grid interface. Assume that the "internal" and "periodic" interface nodes are $\{y_i, y_i+1\}$ and $\{y_p, y_1 = y_p + 1\}$, respectively. The two flux continuity equations (37b) [without correction $\mathscr{E}_{q_i}^{(-)}$] read then with $c_{qy} = 1$ by inserting FLI coefficients from Table XVII:

$$\begin{cases}\Phi_q^{(i)} = 0, \text{ with}\\ \Phi_q^{(i)} = \left[e_q^- + \left(\frac{1}{2} + \delta^{(i)}\right)\hat{n}_q^+ - \Lambda^{-(1)}\hat{n}_q^-\right]_{y_i}^{(1)}\\ -\left[e_q^- - \left(\frac{1}{2} - \delta^{(i)}\right)\hat{n}_q^+ - \Lambda^{-(2)}\hat{n}_q^-\right]_{y_i+1}^{(2)},\end{cases} \quad \text{(D1a)}$$

$$\begin{cases}\Phi_q^{(p)} = 0, \text{ with}\\ \Phi_q^{(p)} = \left[e_q^- + \left(\frac{1}{2} + \delta^{(p)}\right)\hat{n}_q^+ - \Lambda^{-(2)}\hat{n}_q^-\right]_{y_p}^{(2)}\\ -\left[e_q^- - \left(\frac{1}{2} - \delta^{(p)}\right)\hat{n}_q^+ - \Lambda^{-(1)}\hat{n}_q^-\right]_{y_p+1}^{(1)}.\end{cases} \quad \text{(D1b)}$$

The BB reads with $\delta^{(i)} = \delta^{(p)} = 0$ in Eq. (D1). We consider the total flux $\delta\Phi_{\text{FLI}}$ across the domain given by the sum of Eqs. (D1a) and (D1b), $\Phi_{\text{FLI}} = \Phi_q^{(i)} + \Phi_q^{(p)}$, and subtract from it the implicit-interface (BB) flux $\Phi_{\text{BB}} = \Phi_q^{(i)}(\delta^{(i)} = 0) + \Phi_q^{(p)}(\delta^{(p)} = 0) = 0$, which is zero due to the bulk flux discretization in Eq. (26b), provided that $\mathscr{M}(\mathscr{U}^{(sum)})$ is prescribed. This gives:

$$\begin{aligned}\delta\Phi_{\mathrm{FLI}} :&= \Phi_{\mathrm{FLI}} - \Phi_{\mathrm{BB}}\\ &= (\Phi_q^{(i)}(\delta^{(i)}) - \Phi_q^{(i)}(\delta^{(i)} = 0))\\ &\quad + (\Phi_q^{(p)}(\delta^{(p)}) - \Phi_q^{(p)}(\delta^{(p)} = 0)).\end{aligned} \tag{D2}$$

Then,

$$\begin{aligned}\delta\Phi_{\mathrm{FLI}} &= (\hat{n}_q^{+(1)} - \hat{n}_q^{+(2)})(\delta^{(i)} - \delta^{(p)})\\ &= t_q^{(m)}(\mathscr{M}_1 - \mathscr{M}_2)(\delta^{(i)} - \delta^{(p)}),\\ &\text{if } \hat{n}_q^{+} = t_q^{(m)}\mathscr{M}_k c_{qy}^2.\end{aligned} \tag{D3}$$

We equate Eq. (D3) to $-t_q^{(m)}M_0H$ and get M_0 from Eq. (71), which provides the solvability condition. This tells us that FLI/FMR conserves the population mass $[M_0 = 0]$ with $\mathscr{M}(\mathscr{U}^{(sum)})$ only when the two-layers are uniformly shifted from the midway interface position $[\delta^{(i)} = \delta^{(p)}]$. Otherwise, when using the exact definition $M_0(\mathscr{U}^{(ex)})$ in Eq. (68), $M_0 = 0$ with any interface position. These two findings are in agreement with the symbolic and numerical solutions, and they are resumed by Eqs. (70) and (71). These solutions are valid in the heterogeneous series subject to the plug flow $\vec{u} = u_n\vec{1}_n$, but also in the stratified parabolic solutions with $\vec{u} = u_\tau\vec{1}_\tau$, because $\mathscr{M}(y)$ is piece-wise constant and Eq. (66) is valid in these two systems. We note that the total flux $\Phi_q^{(i)} + \Phi_q^{(p)}$ remains the same in the presence of the "physical" interface jump in series, giving $\sigma^{(u)} = 1$, $\eta^{(m)} = ||\mathscr{D}_k||\vec{1}_{y'} \cdot \vec{1}_n$ in Eq. (36) (see next section).

2. The diffusive-flux DFLI MR

We build the grid-shifted straight interface-flux mass-balance in Eq. (37b) [without correction $\mathscr{E}_{q_i}^{(-)}$] with the diffusive-flux parabolic family DFLI from Tables XVI and XVII. We follow Eq. (D1), where we also include the flux jump $\pm J_q$ on the two interfaces, with $J_q = t_q^{(m)}\mathscr{D}_0(\boldsymbol{\phi}_1 - \boldsymbol{\phi}_2)c_{qy}$ in series. We decompose $\Phi_q^{(i)}$ in Eq. (D1) on the local and neighbor components Φ_q^{loc} and Φ_q^{nb}, respectively, and it reads giving $c_{qy} = 1$:

$$\begin{aligned}\Phi_q^{(i)} &= 0,\ \Phi_q^{(i)} = \Phi_q^{loc} + \Phi_q^{nb} - J_q,\\ \Phi_q^{loc} &= \frac{1}{8}(a_1x_1 + a_2x_2),\\ \Phi_q^{nb} &= \frac{1}{8}(A_1X_1 + A_2X_2 + A_3\hat{n}_1^{+} + A_4\hat{n}_2^{+}),\\ x_1 &= e_q^{-} - \Lambda^{-(1)}\hat{n}_q^{-}|_{y_i}^{(1)},\ x_2 = e_q^{-} - \Lambda^{-(2)}\hat{n}_q^{-}|_{y_i+1}^{(2)},\\ X_1 &= e_q^{-} - \Lambda^{-(1)}\hat{n}_q^{-}|_{y_i-1}^{(1)},\ X_2 = e_q^{-} - \Lambda^{-(2)}\hat{n}_q^{-}|_{y_i+2}^{(2)},\end{aligned} \tag{D4}$$

where $\{a_i, A_i\}$ are set by the MR coefficients from Table XVII. The idea is to express the neighbor solution $e_q^{+}|_{y_i-1}^{(1)}$ and $e_q^{+}|_{y_i+2}^{(2)}$ from the in-phase bulk relation in Eq. (27), as

$$\begin{aligned}e_q^{+} + \frac{1}{2}\hat{n}_q^{-} - \Lambda^{+}\hat{n}_q^{+}|_{y_i-1}^{(1)} &= e_q^{+} - \frac{1}{2}\hat{n}_q^{-} - \Lambda^{+}\hat{n}_q^{+}|_{y_i}^{(1)},\\ e_q^{+} + \frac{1}{2}\hat{n}_q^{-} - \Lambda^{+}\hat{n}_q^{+}|_{y_i+1}^{(2)} &= e_q^{+} - \frac{1}{2}\hat{n}_q^{-} - \Lambda^{+}\hat{n}_q^{+}|_{y_i+2}^{(2)}.\end{aligned} \tag{D5}$$

Then, we first substitute the FMR coefficients and confirm that $\Phi_q^{(i)}$ reduces to its FLI solution, given that $\hat{n}_q^{+(k)}$ is layer-wise constant according to Eq. (D3). In turn, DFLI holds

$$\begin{aligned}\tilde{\Phi}_q^{(i)} &= 0,\ \tilde{\Phi}_q^{(i)} = \Phi_q^{(1)} - \Phi_q^{(2)} - J_q,\ \text{with}\\ \Phi_q^{(1)} &= -\Lambda^{-}(\hat{n}_q^{-} + \delta_i\partial_q\hat{n}_q^{-})|_{y_i}^{(1)},\ \delta_i = \frac{1}{2} + \delta^{(i)},\\ \partial_q\hat{n}_q^{-}|_{y_i}^{(1)} &= \hat{n}_q^{-(1)}|_{y_i} - \hat{n}_q^{-(1)}|_{y_i-1},\\ \Phi_q^{(2)} &= -\Lambda^{-}\hat{n}_q^{-} - (1 - \delta_i)\partial_q\hat{n}_q^{-}|_{y_i+1}^{(2)},\\ \partial_q\hat{n}_q^{-}|_{y_i+1}^{(2)} &= \hat{n}_q^{-(2)}|_{y_i+2} - \hat{n}_q^{-(2)}|_{y_i+1}.\end{aligned} \tag{D6a}$$

Obviously, Eq. (D6) presents the back-sided in-phase extrapolations of the diffusive-flux non-equilibrium component $\Phi_q^{(k)} = -\Lambda_k^{-}\hat{n}_q^{-(k)}$. Straightforwardly, the DFLI flux condition shares the same property on the periodic interface $y_1 = y_p + 1$,

$$\begin{aligned}\tilde{\Phi}_q^{(p)} &= 0,\ \tilde{\Phi}_q^{(p)} = \Phi_q^{(2)} - \Phi_q^{(1)} + J_q,\\ \Phi_q^{(2)} &= -\Lambda^{-}(\hat{n}_q^{-} + \delta_p\partial_q\hat{n}_q^{-})|_{y_p}^{(2)},\ \delta_p = \frac{1}{2} + \delta^{(p)},\\ \partial_q\hat{n}_q^{-}|_{y_p}^{(2)} &= \hat{n}_q^{-(2)}|_{y_p} - \hat{n}_q^{-(2)}|_{y_p-1},\\ \Phi_q^{(1)} &= -\Lambda^{-}(\hat{n}_q^{-} - (1 - \delta_p)\partial_q\hat{n}_q^{-})|_{y_1=y_p+1}^{(1)},\\ \partial_q\hat{n}_q^{-(1)}|_{y_1=y_p+1}^{(1)} &= \hat{n}_q^{-(1)}|_{y_2} - \hat{n}_q^{-(1)}|_{y_1}.\end{aligned} \tag{D7a}$$

Given $\mathscr{M}(\mathscr{U}^{(sum)})$, where the implicit bulk discretization is exact, M_0 can be found similar to in Eqs. (D1) from $\delta\Phi_{\mathrm{DFLI}} = \Phi_{\mathrm{DFLI}} - \Phi_{\mathrm{BB}}$, in exact agreement with the symbolic solution

$$M_0 = -\frac{\delta\Phi_{\mathrm{DFLI}}}{Ht_q^{(m)}},\ \Phi_{\mathrm{DFLI}} = \tilde{\Phi}_q^{(i)} + \tilde{\Phi}_q^{(p)}. \tag{D8}$$

DATA AVAILABILITY

The data that support the findings of this study are available from the corresponding author upon reasonable request.

REFERENCES

[1] R. Aris, "On the dispersion of a solute in a fluid flowing through a tube," Proc. R. Soc. London **235**(1200), 67–77 (1956).
[2] H. Bai, P. Yu, S. H. Winoto, and H. T. Low, "Lattice Boltzmann method for flows in porous and homogenuous fluid domains coupled at the interface by stress jump," Int. J. Numer. Methods Fluids **60**, 691–670 (2009).
[3] G. Batôt, L. Talon, Y. Peysson, M. Fleury, and D. Bauer, "Analytical and numerical investigation of the advective and dispersive transport in Herschel-Bulkley fluids by means of a Lattice-Boltzmann two-relaxation-time scheme," Chem. Eng. Sci. **141**, 271–281 (2016).
[4] H. Brenner, "Dispersion resulting from flow through spatially periodic porous media," Philos. Trans. R. Soc. London, Ser. A **297**(1430), 81–133 (1980).
[5] S. Bogner, R. Ammer, and U. Rüde, "Boundary conditions for free interfaces with the lattice Boltzmann method," J. Comput. Phys. **297**, 1–12 (2015).
[6] M. Bouzidi, M. Firdaouss, and, and, and P. Lallemand, "Momentum transfer of a Boltzmann-lattice fluid with boundaries," Phys. Fluids **13**, 3452–3459 (2001).
[7] Z. Chai, B. Shi, and, and, and Z. Guo, "A multiple-relaxation-time lattice Boltzmann model for general nonlinear anistropic convection-diffusion equations," J. Sci. Comput. **69**, 355–390 (2016).
[8] Z. Chai and B. Shi, "Multiple-relaxation-time lattice Boltzmann method for the Navier-Stokes and nonlinear convection-diffusion equations: Modeling, analysis, and elements," Phys. Rev. E **102**, 023306 (2020).
[9] Q. Chen, X. Zhang, and J. Zhang, "Improved treatments for general boundary conditions in the lattice Boltzmann method for convection-diffusion and heat transfer processes," Phys. Rev. E **88**(3), 033304 (2013).

[10] Y. Chen, G. Jin, P. Zhang, S. A. Galindo-Torres, A. Scheuermann, and, and, and L. Ling, "Intercomparison of boundary schemes in Lattice Boltzmann Method for porous media flow simulation," Int. J. Num. Methods Fluids **92**(2), 2009–2029 (2020).
[11] B. Chopard, J. L. Falcone, and, and, and J. Latt, "The lattice Boltzmann advection-diffusion model revisited," Eur. Phys. J. Spec. Top. **171**, 245–249 (2009).
[12] P. V. Danckwerts, "Continuous flow systems," Chem. Eng. Sci. **2**(1–13), 1 (1953).
[13] C. Demuth, S. Mishra, M. A. Mendes, S. Ray, and D. Trimis, "Application and accuracy issues of TRT lattice Boltzmann method for solving elliptic PDEs commonly encountered in heat transfer and fluid flow problems," Int. J. Therm. Sci. **100**, 185–201 (2016).
[14] G. Drazer and J. Koplik, "Tracer dispersion in two dimensional rough fractures," Phys. Rev. E **63**, 056104 (2001).
[15] F. Dubois, C. An Lin, and M. M. Tekitek, "Anisotropic thermal lattice Boltzmann simulation of 2D natural convection in a square cavity," Comput. Fluids. **124**, 278–287 (2016).
[16] D. Gao, Z. Chen, L. Chen, and, and, and D. Zhang, "A modifed lattice Boltzmann for conjugate heat transfer in porous media," Int. J. Heat Mass Transfer. **105**, 673–683 (2017).
[17] T. Gebäck and A. Heintz, "A lattice Boltzmann method for the advection-diffusion equation with Neumann boundary conditions," Commun. Comput. Phys **15**(2), 487–505 (2014).
[18] T. Gebäck, M. Marucci, C. Boissier, J. Arnehed, and A. Heintz, "Investigation of the effect of the tortuous pore structure on water diffusion through a polymer film using lattice Boltzmann simulations," J. Phys. Chem. B **119**(16), 5220–5227 (2015).
[19] A. Genty and V. Pot, "Numerical calculation of effective diffusion in unsaturated porous media by the TRT lattice Boltzmann method," Transp. Porous Med. **105**, 391–410 (2014).
[20] I. Ginzbourg and P. M. Adler, "Boundary flow condition analysis for the three-dimensional lattice Boltzmann model," J. Phys. II France **4**, 191–214 (1994).
[21] I. Ginzbourg and D. d'Humières, "Local second-order boundary method for lattice Boltzmann models," J. Stat. Phys. **84**, 927–971 (1996).
[22] I. Ginzburg and D. d'Humières, "Multi-reflection boundary conditions for lattice Boltzmann models," Phys. Rev. E. **68**, 066614 (2003).
[23] I. Ginzburg and K. Steiner, "Lattice Boltzmann model for free-surface flow and its application to filling process in casting," J. Comput. Phys. **185**, 61–99 (2003).
[24] I. Ginzburg and K. Steiner, "A free-surface lattice Boltzmann method for modelling the fillling of expanding cavities by Bingham fluids," Phil. Trans. R. Soc. London, A **360**, 453–466 (2002).
[25] I. Ginzburg, "Equilibrium-type and link-type lattice Boltzmann models for generic advection and anisotropic-dispersion equation," Adv. Water Res. **28**, 1171–1195 (2005).
[26] I. Ginzburg, "Generic boundary conditions for lattice Boltzmann models and their application to advection and anisotropic-dispersion equations," Adv. Water Res. **28**, 1196–1216 (2005).
[27] I. Ginzburg, "Variably saturated flow described with the anisotropic Lattice Boltzmann methods," J. Comput. Fluids **35**, 831–848 (2006).
[28] I. Ginzburg and D. d'Humières, "Lattice Boltzmann and analytical modeling of flow processes in anisotropic and heterogeneous stratified aquifers," Adv. Water Res. **30**, 2202–2234 (2007).
[29] I. Ginzburg, "Lattice Boltzmann modeling with discontinuous collision components. Hydrodynamic and advection-diffusion equations," J. Stat. Phys. **126**, 157–203 (2007).
[30] I. Ginzburg, F. Verhaeghe, and D. d'Humières, "Two-relaxation-time lattice Boltzmann scheme: About parametrization, velocity, pressure and mixed boundary conditions," Commun. Comput. Phys. **3**(2), 427–478 (2008), available at https://global-sci.org/intro/article_detail/cicp/7862.html.
[31] I. Ginzburg, D. d'Humières, and A. Kuzmin, "Optimal stability of advection-diffusion Lattice Boltzmann models with two relaxation times for positive/negative equilibrium," J. Stat. Phys **139**(6), 1090–1143 (2010).
[32] I. Ginzburg, "Multiple anisotropic collisions for advection-diffusion lattice Boltzmann schemes," Adv. Water Res. **51**, 381–404 (2013).
[33] I. Ginzburg, L. Roux, and, and, and G. Silva, "Local boundary reflections in lattice Boltzmann schemes: Spurious boundary layers and their impact on the velocity, diffusion and dispersion," C. R. Mec. **343**, 518–532 (2015).
[34] I. Ginzburg and L. Roux, "Truncation effect on Taylor-Aris dispersion in lattice Boltzmann schemes: Accuracy towards stability," J. Comput. Phys. **299**, 974–1003 (2015).
[35] I. Ginzburg, "Prediction of the moments in advection-diffusion lattice-Boltzmann method. Part I: Truncation dispersion, skewness and kurtosis," Phys. Rev. E **95**, 013304 (2017).
[36] I. Ginzburg, "Prediction of the moments in advection-diffusion lattice Boltzman method. II. Attenuation of the boundary layers via double-Λ bounce-back flux scheme," Phys. Rev. E **95**, 013305 (2017).
[37] I. Ginzburg and A. Vikhansky, "Determination of the diffusivity, dispersion, skewness and kurtosis in heterogeneous porous flow. Part I: Analytical solutions with the Extended Method of Moments," Adv. Water Res. **115**, 60–87 (2018).
[38] I. Ginzburg, "Determination of the diffusivity, dispersion, skewness and kurtosis in heterogeneous porous flow. Part II: lattice Boltzmann schemes with implicit interface," Adv. Water Res. **118**, 49–82 (2018).
[39] I. Ginzburg, "Spurious interface and boundary behaviour beyond of physical solution in the Lattice Boltzmann schemes," J. Comput. Phys. **431**, 109986 (2021).
[40] I. Ginzburg, "Steady-state Two-relaxation-time lattice Boltzmann formulation for transport and flow, closed with the compact multi-reflection boundary and interface-conjugate schemes," J. Comput. Sci. **2020**, 101215.
[41] Y. Guan and I. Novosselov, "Two relaxation time lattice Boltzmann method coupled to fast Fourier transform Poisson solver: Application to electroconvective flow," J. Comput. Phys. **397**, 108830 (2019).
[42] K. Guo, L. Li, G. Xiao, N. AuYeung, and R. Mei, "Lattice Boltzmann method for conjugate heat and mass transfer with interfacial jump conditions," Int. J. Heat Mass Transfer **88**, 306–322 (2015).
[43] H. Hammou, I. Ginzburg, and M. Boulerhcha, "Two-relaxation-times lattice Boltzmann schemes for solute transport in unsaturated water flow, with a focus on stability," Adv. Water. Res. **34**, 779–793 (2011).
[44] M. Haussmann, N. Hafen, F. Raichle, R. Trunk, H. Nirschl, and M. J. Krause, "Galilean invariance study on different lattice Boltzmann fluid–solid interface approaches for vortex-induced vibrations," Comput. Math. Appl. **80**(5), 671–691 (2020).
[45] Y. Hu, D. Li, S. Shu, and, and X. Niu, "Lattice Boltzmann flux scheme for the convection–diffusion equation and its applications," Comput. Math. Appl. **72**(1), 48–63 (2016).
[46] Z. Hu, J. Huang, and W.-A. Yong, "Lattice Boltzmann method for convection-diffusion equations with general interfacial conditions," Phys. Rev. E **93**, 043320 (2016).
[47] Z. Hu, J. Huang, W.-W. Xuang, and W.-A. Yong, "Second-order curved interface treatments of the lattice Boltzmann method for convection-diffusion equations with conjugate interfacial conditions," Comput. Fluids **144**, 60–73 (2017).
[48] J. Huang and W.-A. Yong, "Boundary conditions of the lattice Boltzmann method for convection-diffusion equations," J. Comput. Phys. **300**, 70–79 (2015).
[49] J. Huang, Z. Hu, and, and, and W.-A. Yong, "Second-order curved boundary treatments of the lattice Boltzmann method for convection-diffusion equations," J. Comput. Phys. **310**, 26–44 (2016).
[50] R. Huang and H. Wu, "A modified multiple-relaxation-time lattice Boltzmann model for convection-diffusion equation," J. Comput. Phys. **274**, 50–63 (2014).
[51] D. d'Humières and I. Ginzburg, "Viscosity independent numerical errors for Lattice Boltzmann models: From recurrence equations to "magic" collision numbers," Comput. Math. Appl. **58**(5), 823–840 (2009).
[52] L. Jahanshaloo, N. A. C. Sidik, A. Fazeli, and M. Pesaran H. A, "An overview of boundary implementation in lattice Boltzmann method for computational heat and mass transfer," Int. Commun. Heat Mass Transfer **78**, 1–12 (2016).
[53] S. Khirevich, I. Ginzburg, and U. Tallarek, "Coarse- and fine-grid numerical behavior of MRT/TRT Lattice-Boltzmann schemes in regular and random sphere packings," J. Comput. Phys. **281**, 708–742 (2015).

[54]H. Karani and C. Huber, "Lattice Boltzmann formulation for conjugate heat transfer in heterogeneous media," Phys. Rev. E **91**, 023304 (2015).
[55]D. Korba, N. Wang, and L. Li, "Accuracy of interface schemes for conjugate heat and mass transfer in the lattice Boltzmann method," Int. J. Heat Mass Transfer **156**, 119694 (2020).
[56]C. Körner, M. Thies, T. Hoffmann, N. Thürey, and U. Rüde, "Lattice Boltzmann model for free surface flow for modeling foaming," J. Stat. Phys. **121**(1/2), 179–197 (2005).
[57]I. Krastins, A. Kao, K. Pericleous, and T. Reis, "Moment-based boundary conditions for straight on-grid boundaries in three-dimensional lattice Boltzmann simulations," Int. J. Numer. Methods Fluids **92**(12), 1948–1974 (2020).
[58]T. Krüger, H. Kusumaatmaja, A. Kuzmin, O. Shardt, G. Silva, and E. M. Viggen, *The Lattice Boltzmann Method Principles and Practice*, 1st ed. (Springer, 2016).
[59]P. Kvist, T. Gebäck, and A. Rasmuson, "A multi-scale model for diffusion of large molecules in steam-exploded wood," Wood Sci. Technol. **54**, 821 (2020).
[60]A. Kuzmin, I. Ginzburg, and A. A. Mohamad, "A role of the kinetic parameter on the stability of two-relaxation-times advection-diffusion Lattice Boltzmann scheme," Comput. Math. Appl. **61**(12), 3417–3442 (2011).
[61]G. Le, O. Oulaid, and J. Zhang, "Counter-extrapolation method for conjugate interfaces in computational heat and mass transfer," Phys. Rev. E **91**, 033306 (2015).
[62]L. Li, R. Mei, and J. F. Klausner, "Boundary conditions for thermal lattice Boltzmann equation method," J. Comput. Phys. **237**, 366–395 (2013).
[63]L. Li, R. Mei, and J. F. Klausner, "Conjugate heat and mass transfer in the lattice Boltzmann equation method," Phys. Rev. E **89**, 043308 (2014).
[64]L. Li and J. Klausner, "Lattice Boltzmann models for the convection-diffusion equation: D2Q5 vs D2Q9," Int. J. Heat Mass Transfer **108**, 41–62 (2017).
[65]L. Li, "Multiple-time-scaling lattice Boltzmann method for the convectio-diffusion equation," Phys. Rev. E **99**, 063301 (2019).
[66]Y. Li and P. Huang, "A coupled lattice Boltzmann model for advection and anisotropic dispersion problem in shallow water," Adv. Water Res. **31**(12), 1719–1730 (2008).
[67]Y. F. Lim, C. de Loubens, R. J. Love, R. G. Lentle, and P. W. M. Janssen, "Flow and mixing by small intestine villi," Food Function **6**, 1787–1795 (2015).
[68]C.-H. Liu, K.-H. Lin, H.-C. Mai, and C.-A. Lin, "Thermal boundary conditions for thermal lattice Boltzmann simulations," Comput. Math. Appl **59**(7), 2178–2193 (2010).
[69]J. H. Lu, H. Y. Lei, and C. S. Dai, "A simple difference method for Lattice Boltzmann algorithm to simulate conjugate heat transfer," Int. J. Heat Mass Transfer **114**, 268–276 (2017).
[70]J. H. Lu, H. Y. Lei, and, and, and C. S. Dai, "An optimal two-relaxation-time lattice Boltzmann equation for solid-liquid phase change: The elimination of unphysical numerical diffusion," Int. J. Therm. Sci. **135**, 17–29 (2019).
[71]R. Mabrouk, H. Naji, H. Dhahri, S. Hammouda, and, and, and Z. Younsi, "Numerical investigation of porosity effect on a PCM's thermal performance in a porous rectangular channel via thermal lattice Boltzmann method," Int. Commun. Heat Mass Transfer **119**, 104992 (2020).
[72]A. Maslo, J. Panjan, and D. Zagar, "Large-scale oil spill simulation using the lattice Boltzmann method, validation on the Lebanon oil spill case," Mar. Pollut. Bull. **84**, 225–235 (2014).
[73]F. Marson, Y. Thorimbert, B. Chopard, I. Ginzburg, and J. Latt, "Enhanced single-node Lattice Boltzmann boundary condition for fluid flows," Phys. Rev. E (in press 2021).
[74]S. N. Nia, F. Rabiei, M. M. Rashidi, and T. M. Kwang, "Lattice Boltzmann simulation of natural convection heat transfer of a nanofluid in a L-shape enclosure with a baffle," Results Phys. **19**, 103413 (2020).
[75]R. Noël, F. Ge, Y. Zhang, and G. Courbebaisse, "Lattice Boltzmann method for modelling of biological phenomena," in 25th European Signal Processing Conference (EUSIPCO), Kos, Greece, 2017.
[76]J. Perko and R. A. Patel, "Single-relaxation-time lattice Boltzmann scheme for advection-diffusion problems with large diffusion-coefficient heterogeneities and high-advection transport," Phys. Rev. E **89**, 053309 (2014).
[77]T. Reis and P. J. Dellar, "Lattice Boltzmann simulations of pressure-driven flows in microchannels using Navier–Maxwell slip boundary conditions," Phys. Fluids **24**, 112001 (2012).
[78]R. Samanta, H. Chattopadhyay, and C. Guha, "Transport phenomena in a differentially heated lid-driven cavity: A study using multi-relaxation-time thermal lattice Boltzmann modeling," Phys. Fluids **32**(9), 093610 (2020).
[79]S. Mohammed, D. Graham, and T. Reis, "Modelling the effects of slip on dipole-wall collision problems using a lattice Boltzmann equation method," Phys. Fluids **32**, 025104 (2020).
[80]C. Rettinger and U. Rüde, "A comparative study of fluid-particle coupling methods for fully resolved lattice Boltzmann simulations," Comput. Fluids **154**, 74–89 (2017).
[81]Z. Rui, J. Li, J. Ma, H. Cai, B. Nie, and H. Peng, "Comparative study on natural convection melting in square cavity using lattice Boltzmann method," Results Phys. **18**, 103274 (2020).
[82]S. Sakane and T. Takaki, "Phase-field lattice Boltzmann method with two-relaxation-time model for dendrite growth of a binary alloy with melt convection," Comput. Mater. Sci. **186**, 110070 (2021).
[83]B. Servan-Camas and F. T. C. Tsai, "Lattice Boltzmann method for two relaxation times for advection-diffusion equation: Third order analysis and stability analysis," Adw. Wat. Res. **31**, 1113–1126 (2008).
[84]B. Servan-Camas and Frank T.-C. Tsai, "Two-relaxation time lattice Boltzmann method for the anisotropic dispersive Henry problem," Water Resour. Res. **46**, W02515, https://doi.org/10.1029/2009WR007837 (2010).
[85]G. Silva and V. Semiao, "Consistent lattice Boltzmann modeling of low-speed isothermal flows at finite Knudsen numbers in slip-flow regime: I. Application to plane boundaries," Phys. Rev. E **96**, 013311 (2017).
[86]G. Silva, "Consistent lattice Boltzmann modeling of low-speed isothermal flows at finite Knudsen numbers in slip-flow regime: II. Application to curved boundaries," Phys. Rev. E **98**, 023302 (2018).
[87]G. Silva and I. Ginzburg, "Reviving the local second-order boundary approach within the two-relaxation-time lattice Boltzmann modelling," Philos. Trans. R. Soc. A **378**, 20190404 (2020).
[88]S. Tao, Q. He, B. Chen, X. Yang, and S. Huang, "One-point second-order curved boundary condition for lattice Boltzmann simulation of suspended particles," Comput. Math. Appl. **76**, 1593–1607 (2018).
[89]S. Tao, A. Xu, Q. He, B. Chen, and F. G. F. Qin, "A curved lattice Boltzmann boundary scheme for thermal convective flows with Neumann boundary condition," Int. J. Heat Mass Transfer **150**, 119345 (2020).
[90]X. Yin, G. Le, and J. Zhang, "Mass and momentum transfer across solid-fluid boundaries in the lattice-Boltzmann method," Phys. Rev. E **86**, 026701 (2012).
[91]D. Yu, R. Mei, L.-S. Luo, and W. Shyy, "Viscous flow computations with the method of lattice Boltzmann equation," Prog. Aerosp. Sci. **39**, 329–367 (2003).
[92]G. I. Taylor, "Dispersion of soluble matter in solvent flowing slowly through a tube," Proc. R. Soc. London, Ser. A **219**, 186–2003 (1953).
[93]F. J. Valdès-Parada, D. Lasseux, and F. Bellet, "A new formulation of the dispersion in homogeneous porous media," Adv. Water Res. **90**, 70–82 (2016).
[94]A. Vikhansky and I. Ginzburg, "Taylor dispersion in heterogeneous porous media: Extended method of moments, theory, and modelling with two-relaxation-times Lattice Boltzmann scheme," Phys. Fluids **26**, 022104 (2014).
[95]L. Wang, S. Tao, X. Meng, K. Zhang, and, and, and G. Lu, "Discrete effects on boundary conditions of the lattice Boltzmann method for fluid flows with curved no-slip walls," Phys. Rev. E **101**, 063307 (2020).
[96]L. Wang, S. Tao, X. Meng, K. Zhang, and G. Lu, "Discrete effects on boundary conditions of the lattice Boltzmann method for convection-diffusion equations with curved geometries," Int. Commun. Heat Mass Transfer **122**, 105130 (2021).
[97]J. Wang, M. Wang, and Z. Li, "A lattice Boltzmann algorithm for fluid-solid conjugate heat transfer," Int. J. Therm. Sci. **46**, 228–234 (2007).
[98]Y. Wang, Y. Zhang, L. Navarro, and G. Courbebaisse, "Multilevel segmentation of intracranial aneurysms in CT angiography images," Med. Phys. **43**(4), 1777–1786 (2016).
[99]D. Wolf-Gladrow, "Lattice gas cellular automata and lattice Boltzmann models: An introduction," *Lecture Notes in Mathematics* (Springer, 2000), Vol. 1725.

[100]Z. Yan, X. Yang, S. Li, and M. Hilpert, "Two-relaxation-time lattice Boltzmann method and its application to advective-diffusive-reactive transport," Adv. Water Res. **109**, 333–342 (2017).
[101]H. Yoshida and M. Nagaoka, "Multiple-relaxation-time lattice Boltzmann model for the convection and anisotropic diffusion equation," J. Comput. Phys. **229**, 7774–7795 (2010).
[102]C. Zhang, T. Suekane, K. Minokawa, and A. Patmonoaji, "Solute transport in porous media studied by lattice Boltzmann simulations at pore scale and x-ray tomography experiments," Phys. Rev. E **100**(6), 063110 (2019).
[103]L. Zhang, Z. Zeng, H. Xie, X. Tao, Y. Zhang, Y. Lu, A. Yoshikawa, and Y. Kawazoe, "An alternative second order scheme for curved boundary condition in lattice Boltzmann method," Comput. Fluids **114**, 193–202 (2015).
[104]L. Zhang, S. Yang, Z. Zeng, and J. W. Chew, "Consistent second-order boundary implementations for convection-diffusion lattice Boltzmann method," Phys. Rev. E **97**(2), 023302 (2018).
[105]L. Zhang, S. Yang, Z. Zeng, and J. W. Chew, "Consistent boundary conditions of the multiple-relaxation-times lattice Boltzmann method for convection-diffusion equations," Comput. Fluids **170**, 24–40 (2018).
[106]M. Zhang, W. Zhao, and P. Lin, "Lattice-Boltzmann method for general convection-diffusion equations: MRT model and boundary schemes," J. Comput. Phys. **389**, 147–163 (2019).
[107]X. Zhang, A. Bengough, L. K. Deeks, J. W. Crawford, and I. M. Young, "A novel three-dimensional lattice Boltzmann model for solute transport in variably saturated porous media," Water Resour. Res. **38**, 6-1–6-10, https://doi.org/10.1029/2001WR000982 (2002).
[108]X. Zhang, J. W. Crawford, R. J. Flavel, and I. M. Young, "A multi-scale Lattice Boltzmann model for simulating solute transport in 3D x-ray-tomography images of aggregated porous materials," J. Hydrol. **541**, 1020 (2016).
[109]Y. Zhao, L. Wang, Z. Chai, and B. Shi, "Comparative study of natural convection melting inside a cubic cavity using an improved two-relaxation-time lattice Boltzmann model," Int. J. Heat Mass Transfer **143**, 118449 (2019).
[110]Y. Zhao, Y. Wu, Z. Chai, and B. Shi, "A block triple-relaxation-time lattice Boltzmann model for nonlinear anisotropic convection–diffusion equations," Comput. Math. Appl. **79**(9), 2550–2573 (2020).